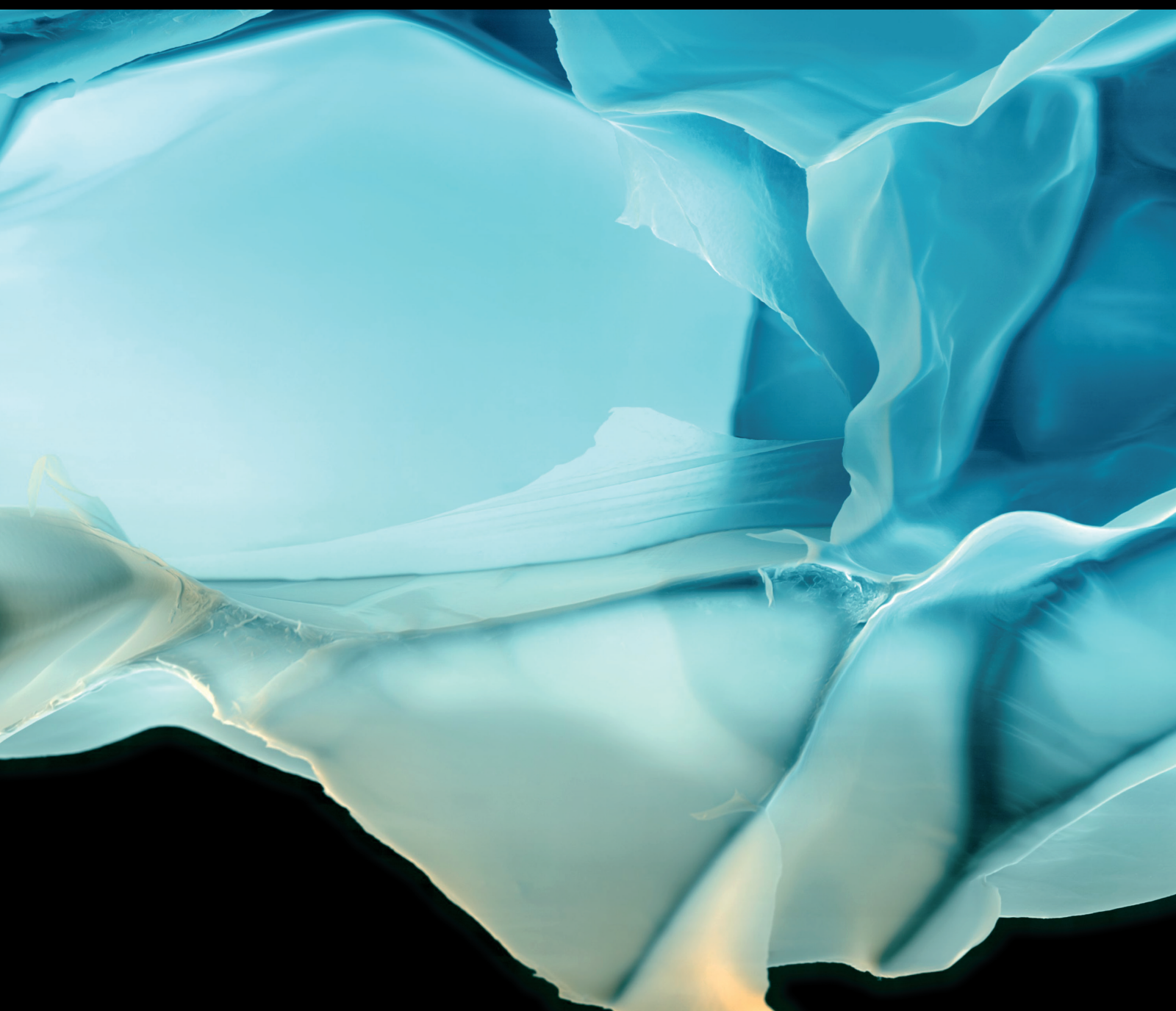


Advances in Polymer Technology

Polymeric Materials for Energy Storage and Conversion

Lead Guest Editor: Professor Yuezhong Meng

Guest Editors: Professor Luyi Sun and Professor Yuning Li





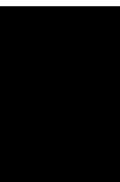
Polymeric Materials for Energy Storage and Conversion

Advances in Polymer Technology

Polymeric Materials for Energy Storage and Conversion

Lead Guest Editor: Professor Yuezhong Meng

Guest Editors: Professor Luyi Sun and Professor
Yuning Li






Copyright © 2020 Hindawi Limited. All rights reserved.

This is a special issue published in "Advances in Polymer Technology." All articles are open access articles distributed under the Creative Commons Attribution License, which permits unrestricted use, distribution, and reproduction in any medium, provided the original work is properly cited.

Chief Editor

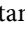






Ning Zhu , China

Associate Editors

Maria L. Focarete , Italy
Leandro Gurgel , Brazil
Lu Shao , China



Academic Editors

Nasir M. Ahmad , Pakistan
Sheraz Ahmad , Pakistan
B Sridhar Babu, India
Xianglan Bai, USA
Lucia Baldino , Italy
Matthias Bartneck , Germany
Anil K. Bhowmick, India
Marcelo Calderón , Spain
Teresa Casimiro , Portugal
Sébastien Déon , France
Alain Durand, France
María Fernández-Ronco, Switzerland
Wenxin Fu , USA
Behnam Ghalei , Japan
Kheng Lim Goh , Singapore
Chiara Gualandi , Italy
Kai Guo , China
Minna Hakkarainen , Sweden
Christian Hopmann, Germany
Xin Hu , China
Puyou Jia , China
Prabakaran K , India
Adam Kiersnowski, Poland
Ick Soo Kim , Japan
Siu N. Leung, Canada
Chenggao Li , China
Wen Li , China
Haiqing Lin, USA
Jun Ling, China
Wei Lu , China
Milan Marić , Canada
Dhanesh G. Mohan , United Kingdom
Rafael Muñoz-Espí , Spain
Kenichi Nagase, Japan
Mohamad A. Nahil , United Kingdom
Ngoc A. Nguyen , USA
Daewon Park, USA
Kinga Pielichowska , Poland

Nabilah Afiqah Mohd Radzuan , Malaysia
Sikander Rafiq , Pakistan
Vijay Raghunathan , Thailand
Filippo Rossi , Italy
Sagar Roy , USA
Júlio Santos, Brazil
Mona Semsarilar, France
Hussein Sharaf, Iraq
Melissa F. Siqueira , Brazil
Tarek Soliman, Egypt
Mark A. Spalding, USA
Gyorgy Szekely , Saudi Arabia
Song Wei Tan, China
Faisal Amri Tanjung , Indonesia
Vijay K. Thakur , USA
Leonard D. Tijing , Australia
Lih-sheng Turng , USA
Kavimani V , India
Micaela Vannini , Italy
Surendar R. Venna , USA
Pierre Verge , Luxembourg
Ren Wei , Germany
Chunfei Wu , United Kingdom
Jindan Wu , China
Zhenhao Xi, China
Bingang Xu , Hong Kong
Yun Yu , Australia
Liqun Zhang , China
Xinyu Zhang , USA

Contents




Semi-interpenetrating Network Membrane from Polyethyleneimine-Epoxy Resin and Polybenzimidazole for HT-PEM Fuel Cells

Chao Meng, Sheng Huang, Dongmei Han, Shan Ren, Shuanjin Wang , and Min Xiao 
Research Article (8 pages), Article ID 3845982, Volume 2020 (2020)



Nonisothermal Kinetic Analysis and AC Conductivity for Polyvinyl Chloride (PVC)/Zinc Oxide (ZnO) Nanocomposite

Huda AlFannakh 
Research Article (18 pages), Article ID 1254301, Volume 2020 (2020)



3D Network Structural Poly (Aryl Ether Ketone)-Polybenzimidazole Polymer for High-Temperature Proton Exchange Membrane Fuel Cells

Junqiao Jiang, Erli Qu, Min Xiao , Dongmei Han, Shuanjin Wang , and Yuezhong Meng 
Research Article (13 pages), Article ID 4563860, Volume 2020 (2020)

A Novel Gel Polymer Electrolyte by Thiol-Ene Click Reaction Derived from CO₂-Based Polycarbonate for Lithium-Ion Batteries

Wenhan Luo, Kuirong Deng, Shuanjin Wang, Shan Ren, Dongmei Han, Yufei Wang, Min Xiao , and Yuezhong Meng 
Research Article (12 pages), Article ID 5047487, Volume 2020 (2020)

A Nitrogen-Rich Covalent Triazine Framework as a Photocatalyst for Hydrogen Production

Ruizhi Gong, Liuliu Yang, Shuo Qiu, Wan-Ting Chen, Qing Wang, Jiazhao Xie, Geoffrey I. N. Waterhouse , and Jing Xu 
Research Article (12 pages), Article ID 7819049, Volume 2020 (2020)

Research Article

Semi-interpenetrating Network Membrane from Polyethyleneimine-Epoxy Resin and Polybenzimidazole for HT-PEM Fuel Cells

Chao Meng,¹ Sheng Huang,¹ Dongmei Han,² Shan Ren,¹ Shuanjin Wang¹ ,¹ and Min Xiao¹ 

¹The Key Laboratory of Low-Carbon Chemistry & Energy Conservation of Guangdong Province/State Key Laboratory of Optoelectronic Materials and Technologies, School of Materials Science and Engineering, Sun Yat-sen University, Guangzhou 510275, China

²School of Chemical Engineering and Technology, Sun Yat-sen University, Zhuhai 519082, China

Correspondence should be addressed to Shuanjin Wang; wangshj@mail.sysu.edu.cn and Min Xiao; stsxm@mail.sysu.edu.cn

Received 29 July 2020; Revised 25 November 2020; Accepted 15 December 2020; Published 30 December 2020

Academic Editor: Federico Carosio

Copyright © 2020 Chao Meng et al. This is an open access article distributed under the Creative Commons Attribution License, which permits unrestricted use, distribution, and reproduction in any medium, provided the original work is properly cited.

In the present work, a semi-interpenetrating network (semi-IPN) high-temperature proton exchange membrane based on polyethyleneimine (PEI), epoxy resin (ER), and polybenzimidazole (PBI) was prepared and characterized, aiming at their future application in fuel cell devices. The physical properties of the semi-IPN membrane are characterized by thermogravimetric analysis (TGA) and tensile strength test. The results indicate that the as-prepared PEI-ER/PBI semi-IPN membranes possess excellent thermal stability and mechanical strength. After phosphoric acid (PA) doping treatment, the semi-IPN membranes show high proton conductivities. PA doping level and volume swelling ratio as well as proton conductivities of the semi-IPN membranes are found to be positively related to the PEI content. High proton conductivities of $3.9 \sim 7.8 \times 10^{-2} \text{ S cm}^{-1}$ are achieved at 160°C for these PA-doped PEI-ER/PBI series membranes. H_2/O_2 fuel cell assembled with PA-doped PEI-ER(1:2)/PBI membrane delivered a peak power density of 170 mW cm^{-2} at 160°C under anhydrous conditions.

1. Introduction

High-temperature (100–200°C) proton exchange membrane fuel cells (HT-PEMFCs) have been receiving increasing attention on account of their advantages over those operated at lower temperatures, including high tolerance to fuel impurities (e.g., CO and H_2S), enhanced activity of the electrocatalysts on both anode and cathode, simplified water, and heat management [1, 2].

After nearly 20 years of development, a series of important advances have been made in the research of high-temperature proton exchange membranes. The research system has developed from the early doping modification of commercial perfluorosulfonic acid-type proton exchange membranes [3–5] to the present inorganic high-temperature proton exchange membrane [6–9], phosphoric acid-doped high-temperature proton exchange membrane

[1, 10–13], phosphonic polymer membrane [14], and other diverse membrane materials coexist. Phosphoric acid-doped high-temperature proton exchange membranes, such as phosphoric acid-doped polybenzimidazole (PBI), exhibit advantages such as high proton conductivity ($4 \times 10^{-2} \sim 8 \times 10^{-2} \text{ S/cm}^{-1}$ @ 150°C) and good chemical stability under high temperature, low humidity, or no water conditions, which has become a research hotspot of high-temperature proton exchange membrane materials [15, 16], and are considered as one of the most promising high-temperature proton exchange membrane materials.

In addition to polybenzimidazole (PBI), there are other polymers that can be doped with phosphoric acid. As early as 1992, phospho-doped polyoxyethylene (PEO), polyacrylamide (PAAM), polyvinylpyrrolidone (PVP), polyethyleneimine (PEI), and other phospho-doped polymer membranes

were prepared by Lassegues [17], but the proton conductivity of these membranes was generally not high (lower than 10^{-3} S·cm⁻¹ at room temperature). One of the most important reasons is that the amount of phosphoric acid in the membrane is too low and cannot be effectively increased, because when the phosphoric acid is too high, these polymers are all paste due to the plasticization of phosphoric acid and cannot form a film at all.

Preparation of semi-interpenetrating polymer network (semi-IPN) is a facile approach to fabricate novel PEMs with specific and various morphology, enhanced mechanical performance, and reduced membrane swelling [18–20]. Tanaka et al. [21] prepared PEI-*x* H₃PO₄ semi-IPN material by treating linear polyethylenimine (PEI) with H₃PO₄ of different metering ratios. Their proton conductivity at a certain temperature is related to *x*. When the range of *x* is extended to 2.5–3.0, the proton conductivity reaches about 10^{-4} S·cm⁻¹ at 50°C. However, after such amount of phosphate is absorbed, the semi-IPN material will become a paste. To solve this problem, the crosslinked PEI (c-PEI) was synthesized by using ethylene glycol diglycidyl ether as the crosslinking agent and then compounded with H₃PO₄. No matter the matrix is PEI or c-PEI, the relationship between proton conductivity and *x* is very similar, but in the crosslinked system, the proton conductivity is smaller.

Loureiro et al. [22] synthesized a semi-interpenetrating polymer network (semi-IPN) through the reaction of epoxy resin with 4,4-diamino-diphenylsulfone and polyethylenimine (PEI). The membrane was acidified by two methods: (i) absorption of H₃PO₄ from aqueous solution and (ii) sulfonation to form covalently bonded -SO₃H. The conductivity value of the film doped with H₃PO₄ at 20% concentration (about 0.08 S·cm⁻¹, 80°C) was higher than that of the sulfonated samples.

The mechanical properties of the materials above, however, do not satisfy the requirement of PEM fuel cells. In recent years, various modification methods have been explored to balance the proton conductivity and mechanical properties of high-temperature proton exchange membranes. For instance, chemical crosslinking modification is an effective method to improve the chemical stability, mechanical properties, and long-term durability of proton exchange membranes [12, 23–28]. In addition, blending is a commonly used and effective method to improve the physical and chemical properties of polymer materials. The new materials obtained by blending not only have the properties of the raw materials themselves but also can overcome the defects of the original materials and produce excellent properties that cannot be matched by a single material.

In this study, we selected PEI, epoxy resin (ER), and PBI as constituent components for the new high-temperature PEM for fuel cells. Branched PEI is a weakly alkaline water-soluble polymer composed of several N-containing functional groups of primary, secondary, and tertiary amines, which can provide multiple active sites for crosslinking reactions and sites for the absorption of phosphoric acid [29, 30]. When PEI-ER and PBI are blended, an in situ crosslinking between ER and PEI in the presence of PBI can form a semi-interpenetrating network structure, which is expected

to improve the mechanical properties and heat resistance of the membrane. Moreover, the semi-IPN membrane should exhibit excellent proton conductivity at high temperature under anhydrous conditions, meeting the need of the application of HT-PEMFCs.

2. Experimental

2.1. Materials and Reagents. Polyethylenimine (PEI) ($M_w = 25\,000$, branched) was purchased from Sigma-Aldrich. Epoxy resin (ER) compound (E-51) was purchased from Macklin. Poly (4,4'-(diphenyl ether)-5,5'-bibenzimidazole) (OPBI) with a viscosity of 6000 Pa·S (tested as 10 wt% solution in N,N'-dimethyl acetamide) was purchased from Shanghai Shengjun Polymer Technologies Co. Ltd. Phosphoric acid (85 wt%) and N-methyl-2-pyrrolidone (NMP) were purchased from Aladdin.

2.2. Membrane Preparation. 80 wt% PEI, 80 wt% ER, and 5 wt% PBI solutions were prepared by dissolving PEI, ER, and PBI in pyrrolidone (NMP), respectively. The PEI, ER, and PBI solution with different volume ratios was mixed and stirred for 12 h at room temperature to obtain a transparent and homogeneous casting solution. Then, the PEI-ER-PBI blend solution was cast onto a glass plate and heated at 60°C for 12 h on a hot plate followed by drying at 140°C for 30 min to allow solidification and remove the solvent. PEI-ER/PBI semi-IPN membranes with PBI amount of 20 wt% and mass ratio of PEI to ER of 1:2, 2:3, 1:1, 3:2, and 2:1 were prepared, which are denoted as PEI-ER(1:2)/PBI, PEI-ER(2:3)/PBI, PEI-ER(1:1)/PBI, PEI-ER(3:2)/PBI, and PEI-ER(2:1)/PBI, in turn. The thickness of the PEI-ER/PBI semi-IPN membranes was controlled to be ~80 μm.

2.3. Characterization

2.3.1. Thermal Analysis. Thermogravimetric curves were recorded from room temperature up to 800°C at a heating rate of 10°C/min in nitrogen atmosphere with a flow rate of 100 mL/min by a Pyris1 TGA (Perkin Elmer). The samples were pretreated by heating to 100°C at a rate of 10°C/minute and kept for 30 minutes before cooling to room temperature.

2.3.2. Mechanical Properties. The mechanical properties of membranes were measured with a universal testing machine (New SANS, Shenzhen, China). The membranes were cut into long rectangular-shaped samples whose initial dimensions were 40 mm in length and 5 mm in width. Measurements were carried out at room temperature (RT) with a constant separating speed of 5 mm min⁻¹.

2.3.3. PA Doping Treatment. For phosphoric acid (PA) doping, dried membranes were cut into 4 × 4 cm² size specimen and the weights of individual specimens were separately noted. The specimens were immersed into 85 wt% PA at 80°C for 2 h. The membranes were taken out from the PA, and excess PA was removed from the membrane surface by carefully wiping the specimens with dust-free paper. After drying at 100°C for 12 h, PA uptake and the size of each sample were measured immediately.

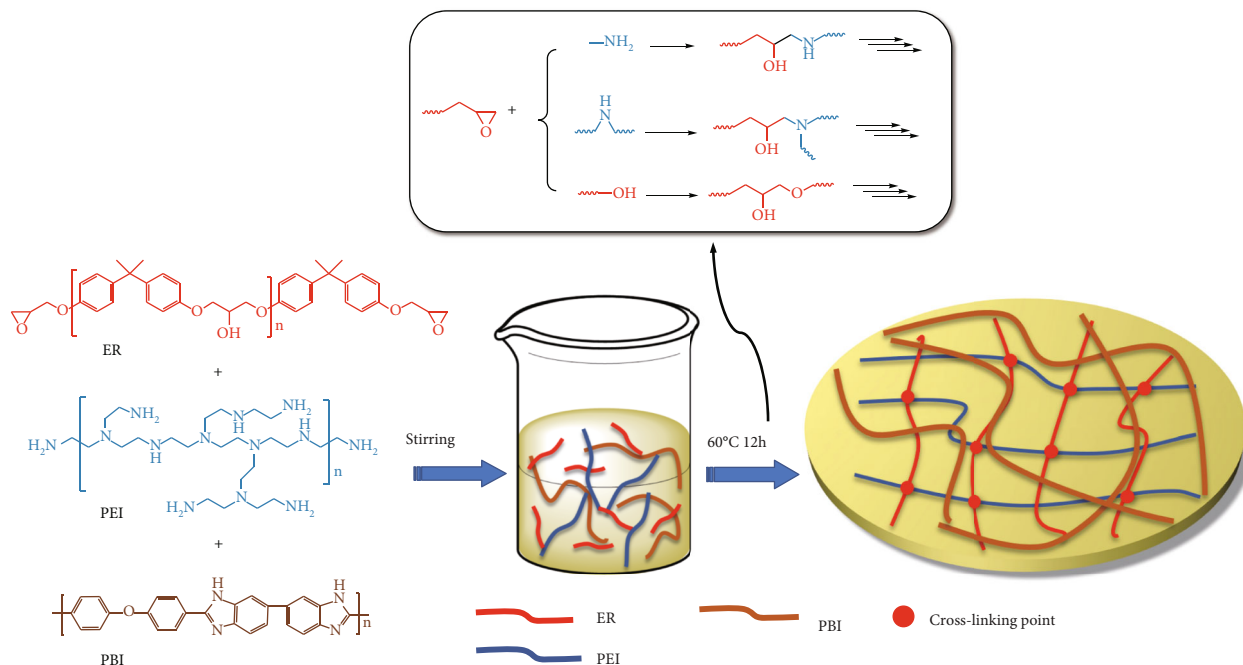


FIGURE 1: In situ step-growth polymerization of polyethyleneimine (PEI) and epoxy resin (ER) in the presence of polybenzimidazole (PBI) to form a PEI-ER/PBI semi-IPN membrane, where PBI and PEI-ER crosslinked networks form a semi-interpenetrating network structure.

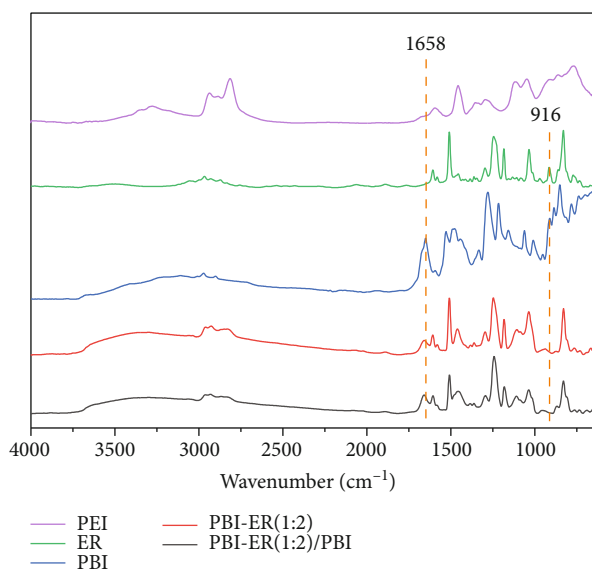


FIGURE 2: FT-IR spectra of PEI, ER, and PBI membranes, PEI-ER(1 : 2) membrane, and PEI-ER(1 : 2)/PBI semi-IPN membrane.

The PA uptake ratio of the membrane (acid doping content (ADC)) was calculated by the following equation:

$$\text{Acid doping content (ADC)(\%)} = \frac{W_2 - W_1}{W_1} \times 100, \quad (1)$$

where W_1 is the initial weight of dried membrane and W_2 is the weight of PA-doped membrane.

The volume swelling ratio and area swelling ratio are defined as the percentage of the membrane volume augment and membrane area augment, respectively, after PA doping treatment and are calculated by the following equation:

$$\begin{aligned} \text{Volume Swelling (\%)} &= \frac{V_2 - V_1}{V_1} \times 100, \\ \text{Area Swelling (\%)} &= \frac{S_2 - S_1}{S_1} \times 100, \end{aligned} \quad (2)$$

where V_2 and S_2 are the volume and area of the PA-doped membrane, respectively. V_1 and S_1 are the volume and area of the undoped dry membrane.

2.3.4. *Structural Characterization.* IR spectra of PEI, ER, and film samples were recorded on a NICOLET 6700 Fourier-Transform Infrared Spectrometer (FT-IR).

2.3.5. *Gel Fraction Test.* The effect of crosslinking was determined by gel fraction test. The membrane samples were immersed in NMP at 80°C for 12 h and then removed from the solvent and dried. The gel fraction was calculated by comparing the weight of the dried sample before and after solvent extraction.

2.3.6. *Proton Conductivity Measurements.* Proton conductivity was measured via a standard four-probe AC impedance method using a PGSTAT204 N electrochemical workstation (AUT86925, AUTOLAB). All samples were cut into 1 cm × 4 cm size, and the average thickness of the samples was obtained by a thickness tester. The PA-doped membranes were stuck in a four-probe clamp and placed in a temperature-controlled chamber. The impedance

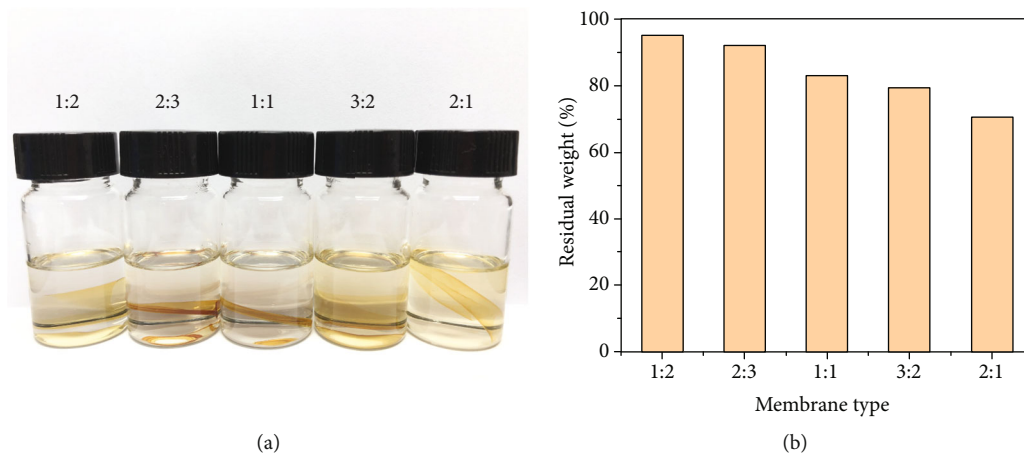


FIGURE 3: Gel fraction test of PEI-ER/PBI membranes performed in NMP at 80°C for 12 h. (a) The membrane samples in NMP at 80°C after 12 h and (b) the residual weight of the membranes after solvent treatment.

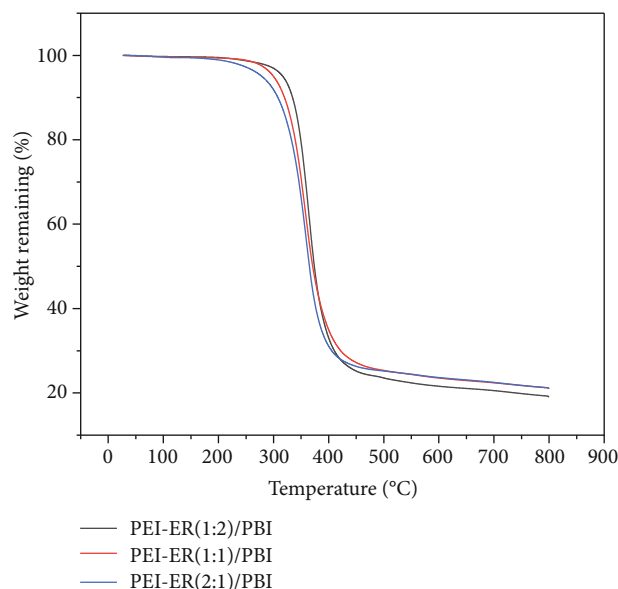


FIGURE 4: TGA curves of different PEI-ER/PBI semi-IPN membranes.

TABLE 1: Acid doping content (ADC) and swelling rate of different semi-IPN membranes.

Membrane	ADC %	Swelling in area %	Swelling in volume %
PEI-ER(1:2)/PBI	101.9	27.0	48.2
PEI-ER(2:3)/PBI	134.7	62.1	68.6
PEI-ER(1:1)/PBI	169.6	77.8	74.7
PEI-ER(3:2)/PBI	272.1	88.7	116
PEI-ER(2:1)/PBI	302.4	107	121

measurement was performed from 80 to 160°C, under anhydrous conditions, in the frequency range of 100 mHz to 100 kHz. The conductivity was calculated by the following formula:

$$\text{Proton conductivity } \sigma = \frac{L}{R \times W \times T}, \quad (3)$$

where L is the distance between reference electrodes, R is the membrane resistance, and W and T are the width and thickness of the samples, respectively.

2.3.7. Fuel Cell Tests. The fuel cell property was assessed using single-cell stacks. Hydrogen and oxygen without prehumidification were applied to the fuel cell at flow rates of 80 mL min⁻¹ and 160 mL min⁻¹, respectively. The area of each of the membrane electrode assemblies (MEAs) was 2.3 × 2.3 cm². The electrodes, 1.0 mg cm⁻² Pt/C for the anode and the cathode, were purchased from Hensen Company. The membranes and electrodes were bonded together by PA without hot pressing, and the active area of the membrane electrode assembly (MEA) was 5 cm². Polarization curves were obtained using current-step potentiometry.

3. Results and Discussion

3.1. Fourier-Transform Infrared (FT-IR) Spectroscopy. The step-growth polymerization of ER and PEI to form a cross-linked network (PEI-ER) (Figure 1) involves the reactions of epoxide (or glycidyl) groups of ER with the primary (–NH₂) and secondary (–NH–) amine groups of PEI and the hydroxyl (–OH) groups of the intermediate products formed through ring opening of the epoxide groups. To gain insight into the reaction between PEI and ER, Fourier-transform infrared (FT-IR) spectroscopy was used to characterize the PEI-ER(1:2) membrane and PEI-ER(1:2)/PBI membrane with curing time of 12 h. As a comparison, the FT-IR spectra of pure PEI, ER, and PBI membrane were also collected.

As shown in Figure 2, C–O stretching of epoxide at 916 cm⁻¹ totally disappeared and a wide O–H stretching peak

TABLE 2: Mechanical properties of different semi-IPN membranes before and after phosphoric acid doping.

Membrane	Tensile strength (MPa)		Elongation at break (%)	
	PA undoped	PA doped	PA undoped	PA doped
PEI-ER(1:2)/PBI	60	4.2	8.6	14
PEI-ER(2:3)/PBI	49	2.2	8.0	4.4
PEI-ER(1:1)/PBI	37	1.4	18	1.4
PEI-ER(3:2)/PBI ^a	22	—	43	—
PEI-ER(2:1)/PBI ^a	13	—	98	—

^aThese membranes swelled significantly in PA solution.

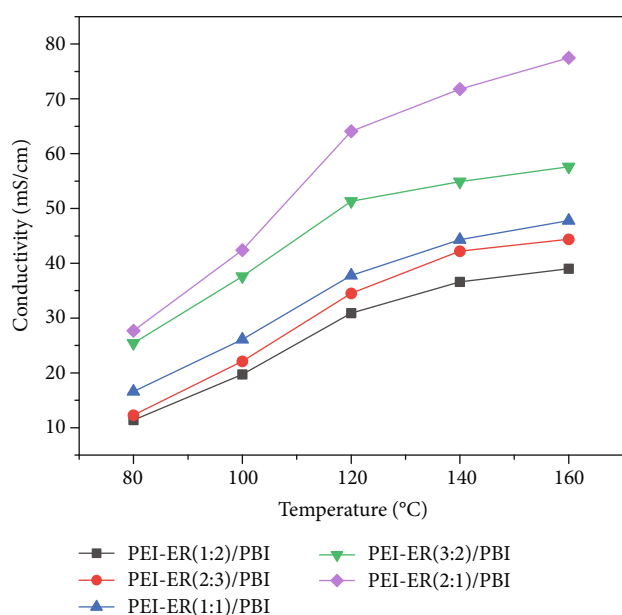


FIGURE 5: Proton conductivities of PA-doped PEI-ER/PBI membranes in anhydrous condition.

appeared at 3200–3700 cm^{-1} in the spectra of PEI-ER(1:2) membrane and PEI-ER(1:2)/PBI membrane, indicating that the epoxy resin was crosslinked successfully with polyethylenimine. The absorption band at 1658 cm^{-1} is attributed to the imidazole ring C=N absorption of PBI.

3.2. Gel Fraction Test. Gel fraction test was carried out to further ascertain that crosslinking was successful. As shown in Figure 3, all the membrane samples maintained the structural integrity after immersing in NMP at 80°C for 12 h. The residual weight of the samples after solvent treatment was over 70% of the original weight. Among them, the gel fraction of PEI-ER(1:2)/PBI, PEI-ER(2:3)/PBI, and PEI-ER(1:1)/PBI membranes was more than 80%, indicating that the semi-interpenetrating network structure may reduce the solubility of PBI in NMP.

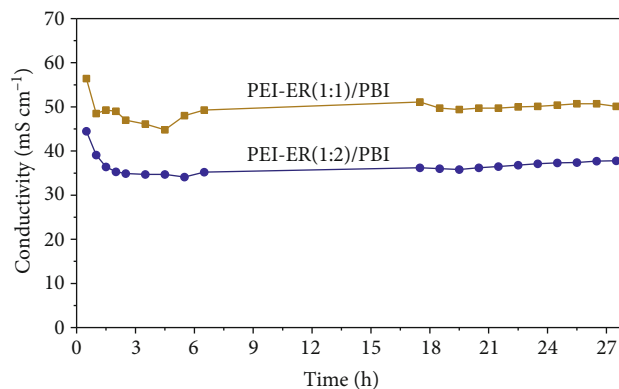


FIGURE 6: Variation of proton conductivity of PA-doped PEI-ER(1:1)/PBI membrane and PA-doped PEI-ER(1:2)/PBI membrane at 140°C in anhydrous condition with time.

3.3. Thermal Properties. Thermal stability of polymer electrolytes is one of the most critical features for long-term durability of fuel cells, especially in high-temperature operation. The thermal stability of PEI-ER/PBI semi-IPN membranes was investigated by TGA under nitrogen atmosphere. The TG curves were recorded after pretreating the samples at 100°C for 30 minutes. Therefore, even though PEI has strong water absorption, the evaporation of water cannot be seen in the spectrum.

As shown in Figure 4, the degradation of PEI-ER/PBI semi-IPN membranes begins at around 300°C, which is much higher than the operation temperature ($\leq 200^\circ\text{C}$) of HT-PEMFCs. Thus, the PEI-ER/PBI semi-IPN membranes have sufficient thermal stability for their application in HT-PEMFCs.

3.4. PA Doping Level. Acid doping treatment was performed by immersing the PEI-ER/PBI semi-IPN membranes in 85 wt% PA solution at 80°C for 2 h. As shown in Table 1, PA uptake increased with the increase of PEI content since the more N-containing functional groups could absorb more phosphoric acid via the acid-base interaction. In addition, the higher the ratio of PEI to ER, the lower the degree of crosslinking and thus the higher phosphoric uptake because the less crosslinked membrane has larger voids for containing the PA. Accordingly, the area and volume swellings of the membranes also increase with the increase of ADC as shown in Table 1, which has been widely reported for PA-doped membranes [31–33].

3.5. Mechanical Properties. An assessment of the mechanical strength of the polymer electrolyte membranes is essential to fabricate membrane electrode assembly. It is well known that high acid doping level usually provides high proton conductivity but results in a large volume swelling ratio and at the expense of mechanical strength. The mechanical properties of PEI-ER/PBI semi-IPN membranes before and after PA doping treatment are summarized in Table 2. The pristine semi-IPN membranes show outstanding mechanical properties and dimensional stability. With the increase of PEI content, the tensile strength decreases from 60 MPa for PEI-

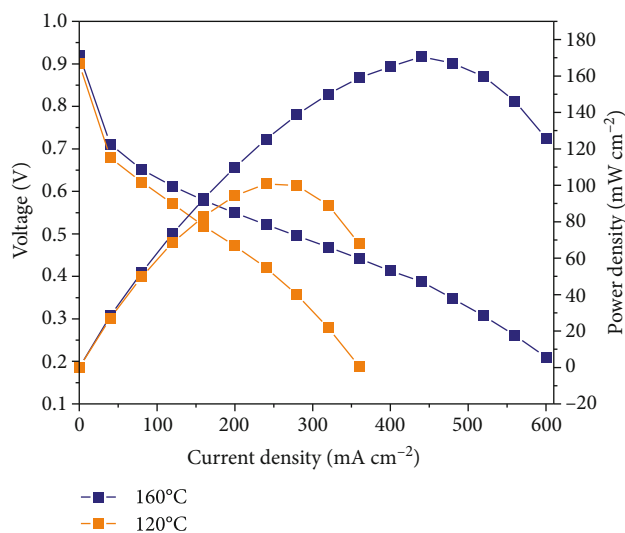


FIGURE 7: Single cell performance of PA-doped PEI-ER(1:2)/PBI at 120°C and 160°C.

ER(1:2)/PBI to 13 MPa for PEI-ER(2:1)/PBI while the elongation at break increases from 8.6% to 98%. It is apparent that more rigid aromatic groups in the backbone and higher crosslinking contribute to higher strength and lower elongation. After PA doping treatment, the mechanical properties of the semi-IPN membranes reduced sharply, especially for PEI-ER(3:2)/PBI and PEI-ER(2:1)/PBI. As He et al. [34] pointed out, high PA doping level will lead to large volume swelling, which will reduce the intermolecular force and thus reduce the mechanical strength of the membrane. However, for the doped membranes with PEI:ER lower than 1:1, the tensile strength is still higher than 1.4 MPa, which is strong enough for membrane electrode assembly.

3.6. Proton Conductivity. The proton conductivities of PA-doped PEI-ER/PBI semi-IPN membranes were measured from 80°C to 160°C without extrahumidification (Figure 5). As expected, the proton conductivities increase with the content of PEI in the membranes increasing because more PA was doped with the increase of the alkaline groups. For the same kind of membrane, the proton conductivity increases sharply with the temperature increases from 80 to 120°C and then level off from 140 to 160°C. The PEI-ER(2:1)/PBI semi-IPN membrane shows the highest proton conductivity of $7.8 \times 10^{-2} \text{ S cm}^{-1}$ at 160°C, and all the membranes exhibit proton conductivity higher than $3.5 \times 10^{-2} \text{ S cm}^{-1}$ at temperatures higher than 140°C, which is sufficient for their application as electrolyte membranes in HT-PEMFCs. A comparison of the proton conductivity of PA-doped PEI-ER/PBI membrane with some of the reported PA-doped PBI membranes is shown in Table S1. The proton conductivity of PEI-ER/PBI series membranes is higher than or comparable to that of PBI and related crosslinked PBI membranes.

Taking both proton conductivity and mechanical strength into consideration, the PA-doped PEI-ER(1:1)/PBI membrane and PEI-ER(1:2)/PBI membrane show good comprehensive performance and were chosen for stability

testing. The variation of proton conductivity with time was tested at 140°C for 27 h. The conductivities were recorded every hour for the first 7 h and the last 10 h with an interval of 10 h in the oven at 140°C overnight. As shown in Figure 6, the proton conductivity first decreased due to the evaporation of adsorbed water and then remained stable. After 27 h, the proton conductivity could still maintain about $4.9 \times 10^{-2} \text{ S cm}^{-1}$ and $3.8 \times 10^{-2} \text{ S cm}^{-1}$, respectively, demonstrating excellent proton conductivity durability in high-temperature and anhydrous environments.

3.7. Fuel Cell Performance. PA-doped PEI-ER(1:2)/PBI membrane was chosen and assembled to perform the fuel cell tests. Figure 7 shows the polarization and power density curves of H_2/O_2 fuel cells obtained at 120°C and 160°C under anhydrous conditions. Open circuit voltages of 0.90 V and 0.92 V were achieved at 120°C and 160°C, respectively, suggesting dense membrane with good gas penetration resistance [35]. Since the reaction kinetics and proton conductivity can be effectively improved by increasing the temperature, as expected, the maximum power density increases with increasing temperature. The highest power density was measured to be 170 mW cm^{-2} at 160°C. The cell performances shown in Figure 7 are very encouraging and demonstrate a promising application of PEI-ER/PBI semi-IPN membrane for HT-PEMFCs.

4. Conclusions

A series of novel PEI-ER/PBI semi-IPN membranes with excellent thermal stability and mechanical strength were prepared by in situ crosslinking of ER and PEI in the presence of PBI. Thanks for the abundant alkaline N-containing functional groups, the PEI-ER/PBI semi-IPN membranes show high PA doping level. Acid doping amount and swelling rate as well as proton conductivities of the PEI-ER/PBI membranes increase with increasing PEI content. The highest proton conductivity of $7.8 \times 10^{-2} \text{ S cm}^{-1}$ at 160°C is achieved for PA-doped PEI-ER(2:1)/PBI membrane, and the PA-doped series membranes with PEI:ER lower than 1:1 show good mechanical strength (1.4~4.2 MPa) and high and stable proton conductivity (higher than $3.5 \times 10^{-2} \text{ S cm}^{-1}$) at temperatures higher than 140°C. The H_2/O_2 fuel cell performance of the PA-doped PEI-ER(1:2)/PBI membrane gave a peak power density of 170 mW cm^{-2} at 160°C under anhydrous conditions, demonstrating promising potential of these PA-doped PEI-ER/PBI membranes as alternative PEMs for HT-PEMFC application.

Data Availability

The authors confirm that the data supporting the findings of this study are available within the article.

Conflicts of Interest

The authors declare that they have no conflicts of interest.

Acknowledgments

This work was supported by the National Key Research and Development Program (2018YFA0702002 and 2019YFA0705701); Link Project of the National Natural Science Foundation of China and Guangdong Province (Grant no. U1601211); the National Key Research and Development Program (Japan-China Joint Research Program) (2017YFE0197900); National Natural Science Foundation of China (51573215, 21506260, 21706294, and 21978332); Guangdong Basic and Applied Basic Research Foundation (Grant nos. 2017B090901003, 2019A1515010803, and 2020A151501445); Guangzhou Scientific and Technological Planning Project (Grant nos. 201804020025, 201707010424, and 201904010271); and the Fundamental Research Funds for the Central Universities (Grant nos. 18lgpy32, 19lgpy07, and 20lgpy11).

Supplementary Materials

Table S1: comparison of the proton conductivity of PA-doped PEI-ER/PBI membrane with some of the reported PA-doped PBI membranes. (*Supplementary Materials*)

References

- [1] S. Bose, T. Kuila, T. X. H. Nguyen, N. H. Kim, K. T. Lau, and J. H. Lee, "Polymer membranes for high temperature proton exchange membrane fuel cell: recent advances and challenges," *Progress in Polymer Science*, vol. 36, no. 6, pp. 813–843, 2011.
- [2] A. Chandan, M. Hattenberger, A. El-Kharouf et al., "High temperature (HT) polymer electrolyte membrane fuel cells (PEMFC) - a review," *Journal of Power Sources*, vol. 231, pp. 264–278, 2013.
- [3] Z. G. Shao, P. Joghee, and I. M. Hsing, "Preparation and characterization of hybrid Nafion-silica membrane doped with phosphotungstic acid for high temperature operation of proton exchange membrane fuel cells," *Journal of Membrane Science*, vol. 229, no. 1-2, pp. 43–51, 2004.
- [4] A. Saccà, A. Carbone, E. Passalacqua et al., "Nafion-TiO₂ hybrid membranes for medium temperature polymer electrolyte fuel cells (PEFCs)," *Journal of Power Sources*, vol. 152, pp. 16–21, 2005.
- [5] A. Saccà, I. Gatto, A. Carbone, R. Pedicini, and E. Passalacqua, "ZrO₂-Nafion composite membranes for polymer electrolyte fuel cells (PEFCs) at intermediate temperature," *Journal of Power Sources*, vol. 163, no. 1, pp. 47–51, 2006.
- [6] S. M. Haile, D. A. Boysen, C. R. I. Chisholm, and R. B. Merle, "Solid acids as fuel cell electrolytes," *Nature*, vol. 410, no. 6831, pp. 910–913, 2001.
- [7] W. Zhou, A. S. Bondarenko, B. A. Boukamp, and H. J. M. Bouwmeester, "Superprotonic conductivity in MH PO₃H M = Li⁺, Na⁺, K⁺, Rb⁺, Cs⁺, NH₄⁺," *Solid State Ionics*, vol. 179, no. 11-12, pp. 380–384, 2008.
- [8] S. Lu, D. Wang, S. P. Jiang, Y. Xiang, J. Lu, and J. Zeng, "HPW/MCM-41 phosphotungstic acid/mesoporous silica composites as novel proton-exchange membranes for elevated-temperature fuel cells," *Advanced Materials*, vol. 22, no. 9, pp. 971–976, 2010.
- [9] J. Zeng and S. P. Jiang, "Characterization of high-temperature proton-exchange membranes based on phosphotungstic acid functionalized mesoporous silica nanocomposites for fuel cells," *Journal of Physical Chemistry C*, vol. 115, no. 23, pp. 11854–11863, 2011.
- [10] Z. Zhou, R. Liu, J. Wang, S. Li, and J. L. Brédas, "Intra- and intermolecular proton transfer in 1H(2H)-1,2,3-triazole based systems," *Journal of Physical Chemistry A*, vol. 110, no. 7, pp. 2322–2324, 2006.
- [11] Y. Chen, M. Thorn, S. Christensen et al., "Enhancement of anhydrous proton transport by supramolecular nanochannels in comb polymers," *Nature Chemistry*, vol. 2, no. 6, pp. 503–508, 2010.
- [12] W. Ma, C. Zhao, J. Yang et al., "Cross-linked aromatic cationic polymer electrolytes with enhanced stability for high temperature fuel cell applications," *Energy & Environmental Science*, vol. 5, no. 6, pp. 7617–7625, 2012.
- [13] Q. Li, R. He, J. O. Jensen, and N. J. Bjerrum, "PBI-based polymer membranes for high temperature fuel cells - preparation, characterization and fuel cell demonstration," *Fuel Cells*, vol. 4, no. 3, pp. 147–159, 2004.
- [14] B. Lin, L. Qiu, J. Lu, and F. Yan, "Cross-linked alkaline ionic liquid-based polymer electrolytes for alkaline fuel cell applications," *Chemistry of Materials*, vol. 22, no. 24, pp. 6718–6725, 2010.
- [15] S. Subianto, "Recent advances in polybenzimidazole/phosphoric acid membranes for high-temperature fuel cells," *Polymer International*, vol. 63, no. 7, pp. 1134–1144, 2014.
- [16] D. J. Jones and R. Jacques, "Recent advances in the functionalisation of polybenzimidazole and polyetherketone for fuel cell applications," *Journal of Membrane Science*, vol. 185, no. 1, pp. 41–58, 2001.
- [17] J. C. Lassegues, *Proton Conductors: Solids, Membranes and Gels-Materials and Devices*, P. Colomban, Ed., Cambridge University Press, 1992.
- [18] C. W. Lin, Y. F. Huang, and A. M. Kannan, "Semi-interpenetrating network based on cross-linked poly(vinyl alcohol) and poly(styrene sulfonic acid-co-maleic anhydride) as proton exchange fuel cell membranes," *Journal of Power Sources*, vol. 164, no. 2, pp. 449–456, 2007.
- [19] C.-H. Lee and Y.-Z. Wang, "Synthesis and characterization of epoxy-based semi-interpenetrating polymer networks sulfonated polyimides proton-exchange membranes for direct methanol fuel cell applications," *Journal of Polymer Science Part A: Polymer Chemistry*, vol. 46, no. 6, pp. 2262–2276, 2008.
- [20] Y. F. Huang, L. C. Chuang, A. M. Kannan, and C. W. Lin, "Proton-conducting membranes with high selectivity from cross-linked poly(vinyl alcohol) and poly(vinyl pyrrolidone) for direct methanol fuel cell applications," *Journal of Power Sources*, vol. 186, no. 1, pp. 22–28, 2009.
- [21] R. Tanaka, H. Yamamoto, A. Shono, K. Kubo, and M. Sakurai, "Proton conducting behavior in non-crosslinked and cross-linked polyethylenimine with excess phosphoric acid," *Electrochimica Acta*, vol. 45, no. 8-9, pp. 1385–1389, 2000.
- [22] F. A. M. Loureiro, R. P. Pereira, and A. M. Rocco, "Polyethyleneimine-based semi-interpenetrating network membranes for fuel cells," *The Electrochemical Society*, vol. 45, no. 23, pp. 11–19, 2013.
- [23] N. N. Krishnan, D. Joseph, N. M. H. Duong et al., "Phosphoric acid doped crosslinked polybenzimidazole (PBI-OO) blend membranes for high temperature polymer electrolyte fuel cells," *Journal of Membrane Science*, vol. 544, pp. 416–424, 2017.

- [24] F. Mack, K. Aniol, C. Ellwein, J. Kerres, and R. Zeis, "Novel phosphoric acid-doped PBI-blends as membranes for high-temperature PEM fuel cells," *Journal of Materials Chemistry A*, vol. 3, no. 20, pp. 10864–10874, 2015.
- [25] D. Joseph, N. N. Krishnan, D. Henkensmeier et al., "Thermal crosslinking of PBI/sulfonated polysulfone based blend membranes," *Journal of Materials Chemistry A*, vol. 5, pp. 409–417, 2016.
- [26] S. K. Kim, K. H. Kim, J. O. Park et al., "Highly durable polymer electrolyte membranes at elevated temperature: cross-linked-copolymer structure consisting of poly(benzoxazine) and poly(benzimidazole)," *Journal of Power Sources*, vol. 226, pp. 346–353, 2013.
- [27] B. Singh, N. M. H. Duong, D. Henkensmeier et al., "Influence of different side-groups and cross-links on phosphoric acid doped radel-based polysulfone membranes for high temperature polymer electrolyte fuel cells," *Electrochimica Acta*, vol. 224, pp. 306–313, 2017.
- [28] J. Jiang, E. Qu, M. Xiao, D. Han, S. Wang, and Y. Meng, "3D network structural poly (aryl ether ketone)-polybenzimidazole polymer for high-temperature proton exchange membrane fuel cells," *Advances in Polymer Technology*, vol. 2020, 13 pages, 2020.
- [29] S. Wang, Z. Li, and C. Lu, "Polyethyleneimine as a novel desorbent for anionic organic dyes on layered double hydroxide surface," *Journal of Colloid & Interface Science*, vol. 458, pp. 315–322, 2015.
- [30] X. S. Song, S. Xing, H. P. Li et al., "An antibody that confers plant disease resistance targets a membrane-bound glyoxal oxidase in *Fusarium*," *New Phytologist*, vol. 210, no. 3, pp. 997–1010, 2016.
- [31] J. Yang, J. Wang, C. Liu et al., "Influences of the structure of imidazolium pendants on the properties of polysulfone-based high temperature proton conducting membranes," *Journal of Membrane Science*, vol. 493, pp. 80–87, 2015.
- [32] Q. Li, R. He, R. W. Berg, H. A. Hjuler, and N. J. Bjerrum, "Water uptake and acid doping of polybenzimidazoles as electrolyte membranes for fuel cells," *Solid State Ionics Diffusion & Reactions*, vol. 168, no. 1-2, pp. 177–185, 2004.
- [33] J. Yang, D. Aili, Q. Li et al., "Benzimidazole grafted polybenzimidazoles for proton exchange membrane fuel cells," *Polymer Chemistry*, vol. 4, no. 17, p. 4768, 2013.
- [34] R. H. He, Q. F. Li, A. Bach, J. O. Jensen, and N. J. Bjerrum, "Physicochemical properties of phosphoric acid doped polybenzimidazole membranes for fuel cells," *Journal of Membrane Science*, vol. 277, no. 1-2, pp. 38–45, 2006.
- [35] J. Yang, Q. Li, L. N. Cleemann et al., "Crosslinked hexafluoropropylidene polybenzimidazole membranes with chloromethyl polysulfone for fuel cell applications," *Advanced Energy Materials*, vol. 3, no. 5, pp. 622–630, 2013.

Research Article

Nonisothermal Kinetic Analysis and AC Conductivity for Polyvinyl Chloride (PVC)/Zinc Oxide (ZnO) Nanocomposite

Huda Alfannakh 

Physics Department, King Faisal University, P.O. Box 31982 Al-Ahsa, Saudi Arabia

Correspondence should be addressed to Huda Alfannakh; halfannakh@kfu.edu.sa

Received 12 January 2020; Revised 28 June 2020; Accepted 10 July 2020; Published 17 August 2020

Academic Editor: Yuezhong Meng

Copyright © 2020 Huda Alfannakh. This is an open access article distributed under the Creative Commons Attribution License, which permits unrestricted use, distribution, and reproduction in any medium, provided the original work is properly cited.

The behavior of polyvinyl chlorine (PVC)/zinc oxide (ZnO) nanoparticles was investigated. To improve the dispersion and distribution of zinc nanoparticles within the host polymer (PVC), they were treated with water before being added to the polymer. The nanocomposite samples were prepared by casting method using different weight ratios of ZnO nanoparticles. The prepared nanocomposite samples were characterized by thermogravimetric analysis (TGA). Both thermal stability and kinetic analysis of the prepared samples were investigated. The ZnO nanoparticles lower the activation energy and decrease the thermal stability of PVC. Kissinger, Flynn-Wall-Ozawa, and Kissinger-Akahira-Sunose models were used in the nonisothermal kinetic analysis of PVC/ZnO nanocomposite samples. The thermal stability behavior due to the addition of zinc oxide nanoparticles was explained and correlated with the behavior of the kinetic parameters of the samples. The AC conductivity as function of frequency and temperature was also investigated. The addition of ZnO nanoparticle increases the AC conductivity, and the temperature-independent region decreased by increasing temperature. Both S and A coefficients were predicted using the Jonscher power law and OriginLab software. The trends of S and A coefficients were discussed based on the glass transition of the host polymer.

1. Introduction

Thermoplastic polymers have physical and chemical properties that meet the requirements for many industrial applications. Among the thermoplastics, the industrial use of PVC is ranked second after polyethylene. It has been used in the manufacturing of electrical insulators, insulating floors, ceilings, medical devices, packaging, pipe industry, and many other countless applications [1]. Due to its tremendous importance in the manufacturing industry, PVC receives a lot of attention from researchers.

For example, in order to improve the thermal properties of PVC, Hajibeygi et al. [2] used a ternary nanocomposite containing PVC/chitosan-modified ZnO nanoparticles. They further investigated the thermal stability by using PVC-modified ZnO nanoparticles with imide functionalized polyethyleneimine (PEI). In both cases, they found that the ternary system possessed more thermal stability than host PVC polymer. Taha et al. [3] investigated the thermal stability of PVC/SnO₂ nanocomposite, and they found that

the glass transition increased for SnO₂-doped samples. In addition, the thermal stability increased for the high-temperature decomposition stage (350-550°C). PVC reinforced by ZnO nanoparticles was investigated by Mallakpour and Darvishzadeh [4]. According to their TGA data, the thermal stability of PVC at the high-temperature stage was increased by increasing the percent of ZnO/bovine serum albumin BSA nanoparticles. The thermal stability of PVC/TiO₂ nanoparticles covered by bovine serum was also investigated by Mallakpour and Shamsaddinimotlagh [5]. Their TGA analysis showed higher thermal stability for the nanocomposite samples than the host polymer in its pure form.

Hajibeygi et al. [6] investigated the thermal stability of PVC-modified ZnO nanoparticles with imide functionalized polyethyleneimine (PEI). The thermal stability of the prepared modified nanocomposite sample was increased.

PVC loaded with 2 wt.% ZnO nanoparticles was prepared to investigate the effect of molecular weight of PVC on the thermal properties of nanocomposite [7]. The glass transition

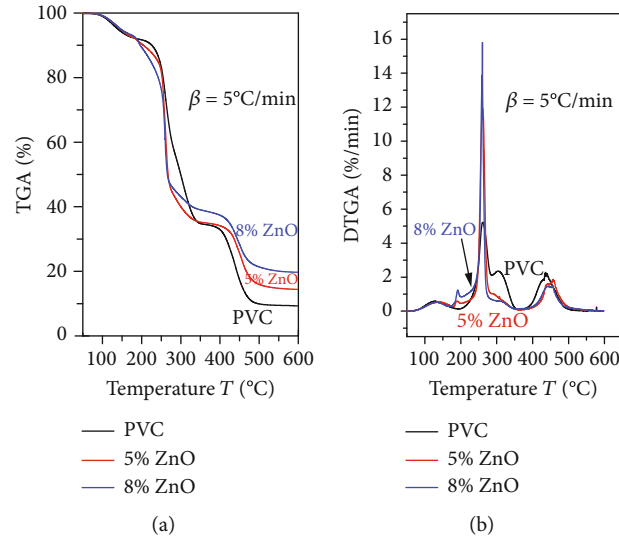


FIGURE 1: (a) TGA spectra and (b) DTGA spectra for PVC and PVC/ZnO nanocomposite at 5°C/min heating rate.

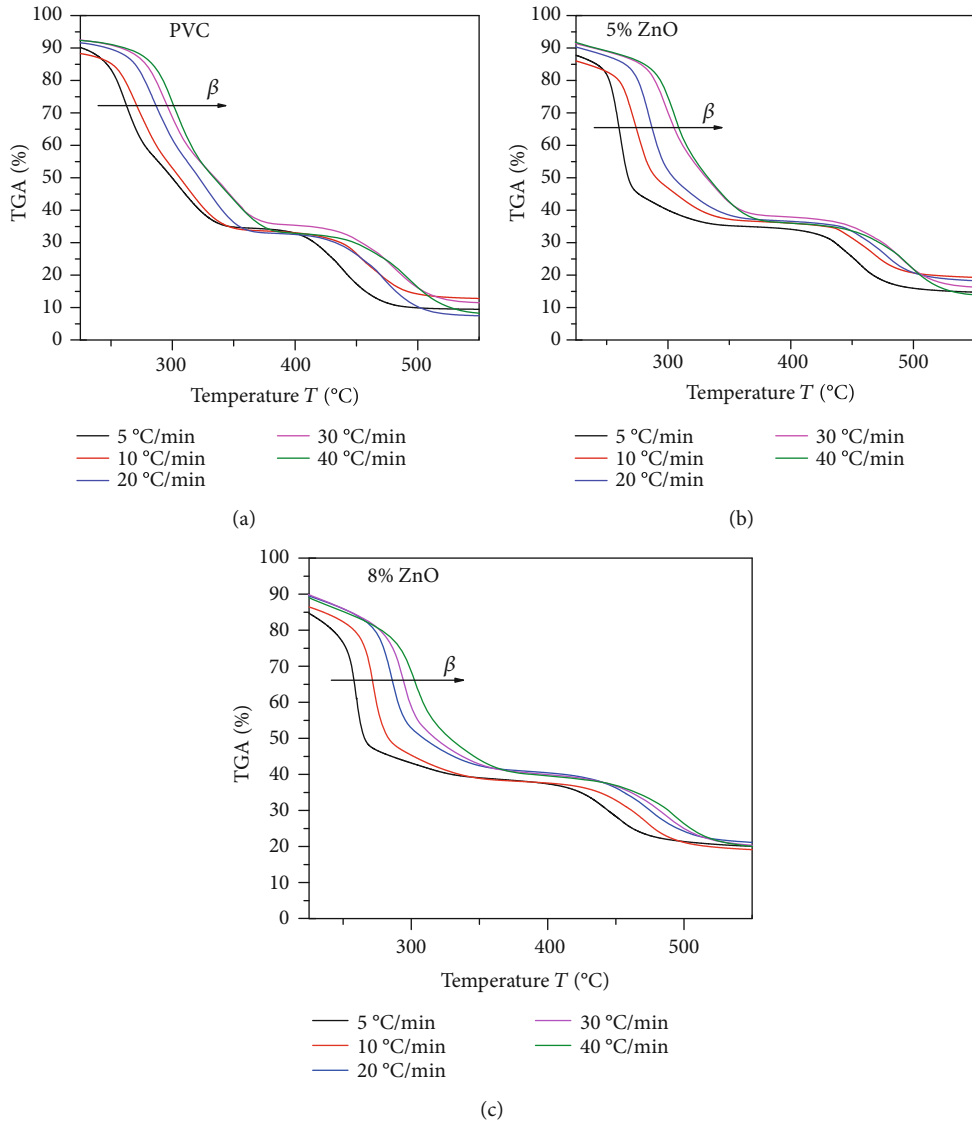


FIGURE 2: TGA spectra for (a) pure PVC, (b) 5 wt.% ZnO, and (c) 8 wt.% ZnO nanocomposite samples at different heating rates.

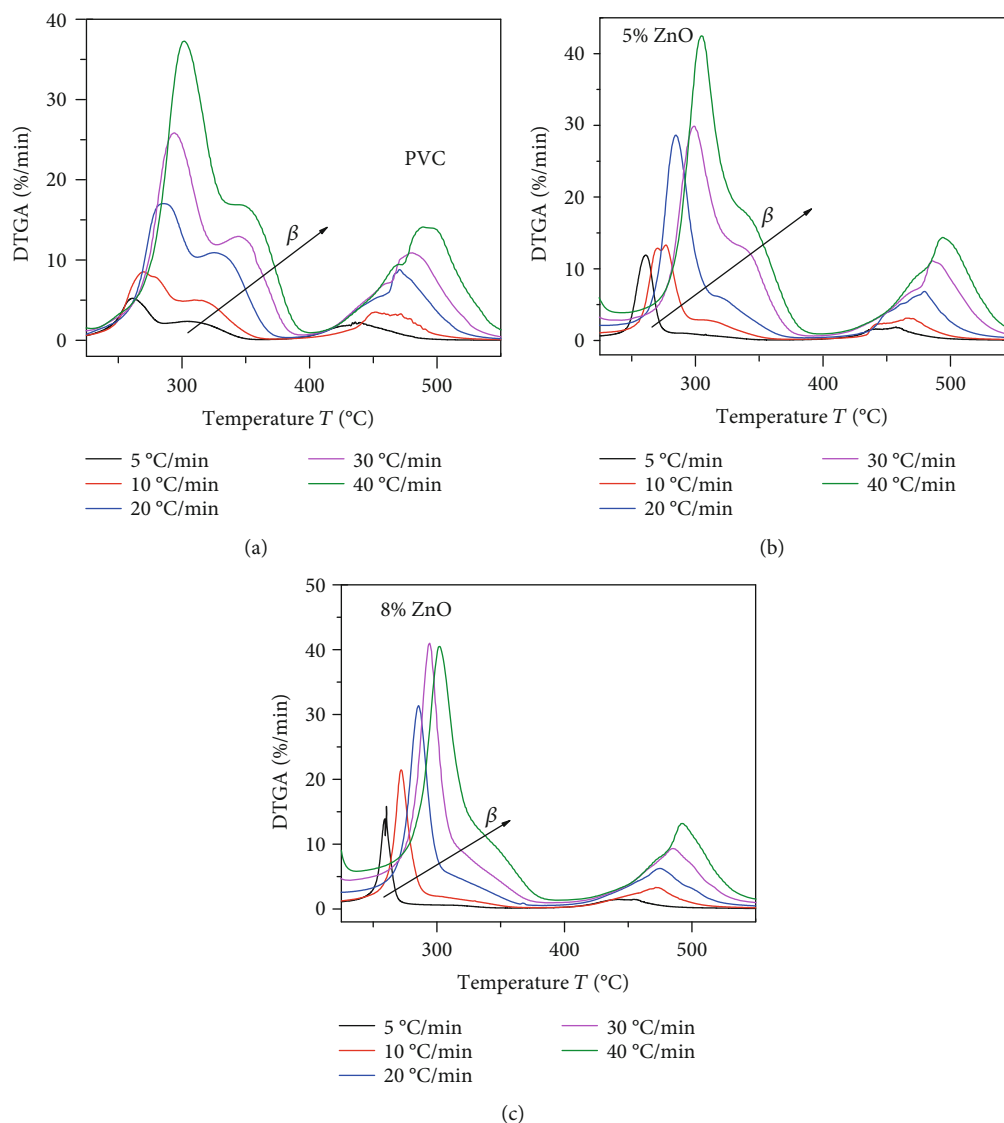


FIGURE 3: DTGA spectra for (a) pure PVC, (b) 5 wt.% ZnO, and (c) 8 wt.% ZnO nanocomposite samples at different heating rates.

of the prepared nanocomposite was increased, and it was noted that the higher the molecular weight, the greater the extent of the glass transition enhancement. Taha [8] has investigated the thermal stability for Pb_3O_4 /PVC nanocomposites. The data revealed that such nanocomposites have higher thermal stability than pure PVC film.

The thermal degradation of PVC/iron oxide-modified montmorillonite (MMT) nanocomposite was investigated [9] in air atmosphere, and the activation energies were obtained using the Kissinger model. The iron-modified PVC nanocomposite samples showed higher thermal stability and higher activation energy than the pure PVC. PVC/sepiolite nanocomposite sample decreases the thermal stability of PVC and the activation energy in both decomposition stages of PVC [10]. Sánchez-Jiménez et al. [11] investigated the kinetics of PVC decomposition and revealed that there are two main different processes. The first process is represented by nucleation and growth mechanism with activation

energy of about 114 kJ/mol while the second is represented by a diffusion-controlled model with an activation energy of about 202 kJ/mol. Many other researchers have investigated the thermal stability, thermal degradation, and kinetic analysis for PVC, PVC blend, and PVC nanocomposites using different kinetic models [12–20]. Several researchers investigate the conduction mechanism and the AC conductivity of such nanocomposite samples.

In the present work, we aim to investigate the kinetics of the thermal analysis of PVC/ZnO nanoparticle using different kinetic models. The effect of the addition of ZnO on the thermal stability and the AC conductivity of this type of nanocomposite will be discussed. TGA nonisothermal data at different heating rates will be used to calculate the activation energy (E_a) and preexponential factor (A) using the Kissinger, FWO, and KAS models. The Jonscher universal power law will be used to discuss the AC conductivity of the composite.

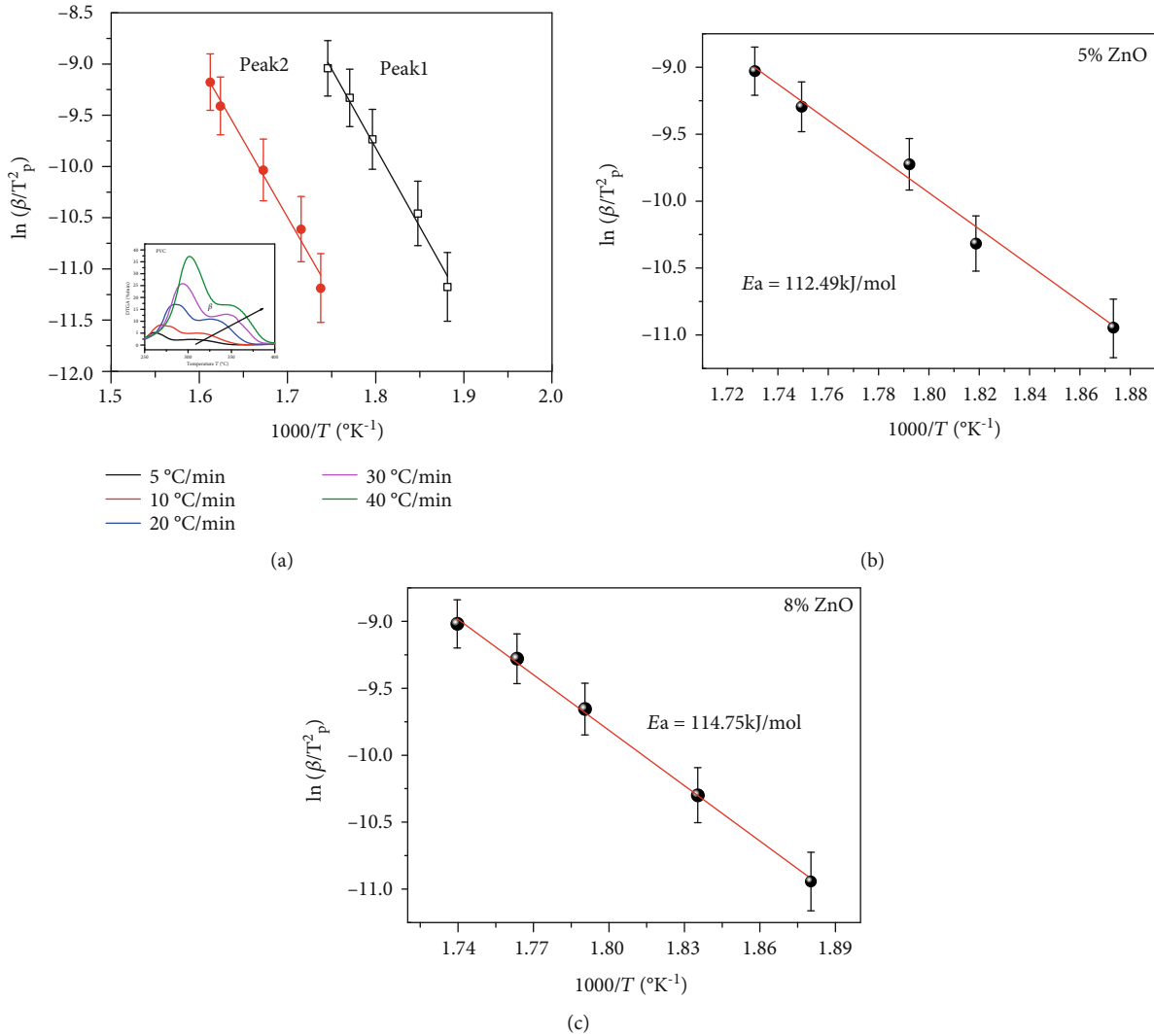


FIGURE 4: $\ln(\beta/T_p^2)$ vs. $1/T_p$ for (a) pure PVC, (b) 5 wt.% PVC/ZnO, and (c) 8 wt.% PVC/ZnO samples, respectively.

2. Model-Free Methods

2.1. Kissinger Method. The Kissinger model is one of the simplest models used to find the kinetic parameters of a reaction without going into the details of reaction mechanism [21]. In the Kissinger model, we rely on the relationship between $\ln(\beta/T_p^2)$ versus $1000/T_p$ for a series of degradation curves at different heating rates (β) where T_p is the temperature at maximum decomposition rate. For a first-order reaction, the following equation holds:

$$\ln\left(\frac{\beta}{T_p^2}\right) = \ln\left(\frac{AR}{E_a}\right) - \frac{E_a}{RT_p} \quad (1)$$

The apparent activation energy (E_a) can be deduced by finding the accurate slope of such relation (slope = $-E_a/R$).

2.2. Flynn-Wall-Ozawa Method. The FWO model depends on the relation between $\ln(\beta_i)$ versus $(1/T_{ai})$ for specific

values of conversion at different values of β . The following equation can be used for the FWO model [22, 23]:

$$\ln(\beta_i) = \ln\left(\frac{A_\alpha E_a}{R g(\alpha)}\right) - 5.331 - 1.052 \frac{E_a}{RT_{ai}} \quad (2)$$

Note that it is important to know that the function $g(\alpha)$ is constant for each given value of α . From the above relation, one can calculate the apparent activation energy for each α from the slope of the linear relation (slope = $-1.052E_a/R$).

2.3. Kissinger-Akahira-Sunose. Their model can be written as follows [24–26]:

$$\ln\left(\frac{\beta}{T_{ai}^2}\right) = \ln\left(\frac{A_\alpha R}{E_a g(\alpha)}\right) - \frac{E_a}{RT_{ai}} \quad (3)$$

by plotting $\ln(\beta_i/T_{ai}^2)$ vs. $1/T_{ai}$ and from the slope E_a can be obtained.

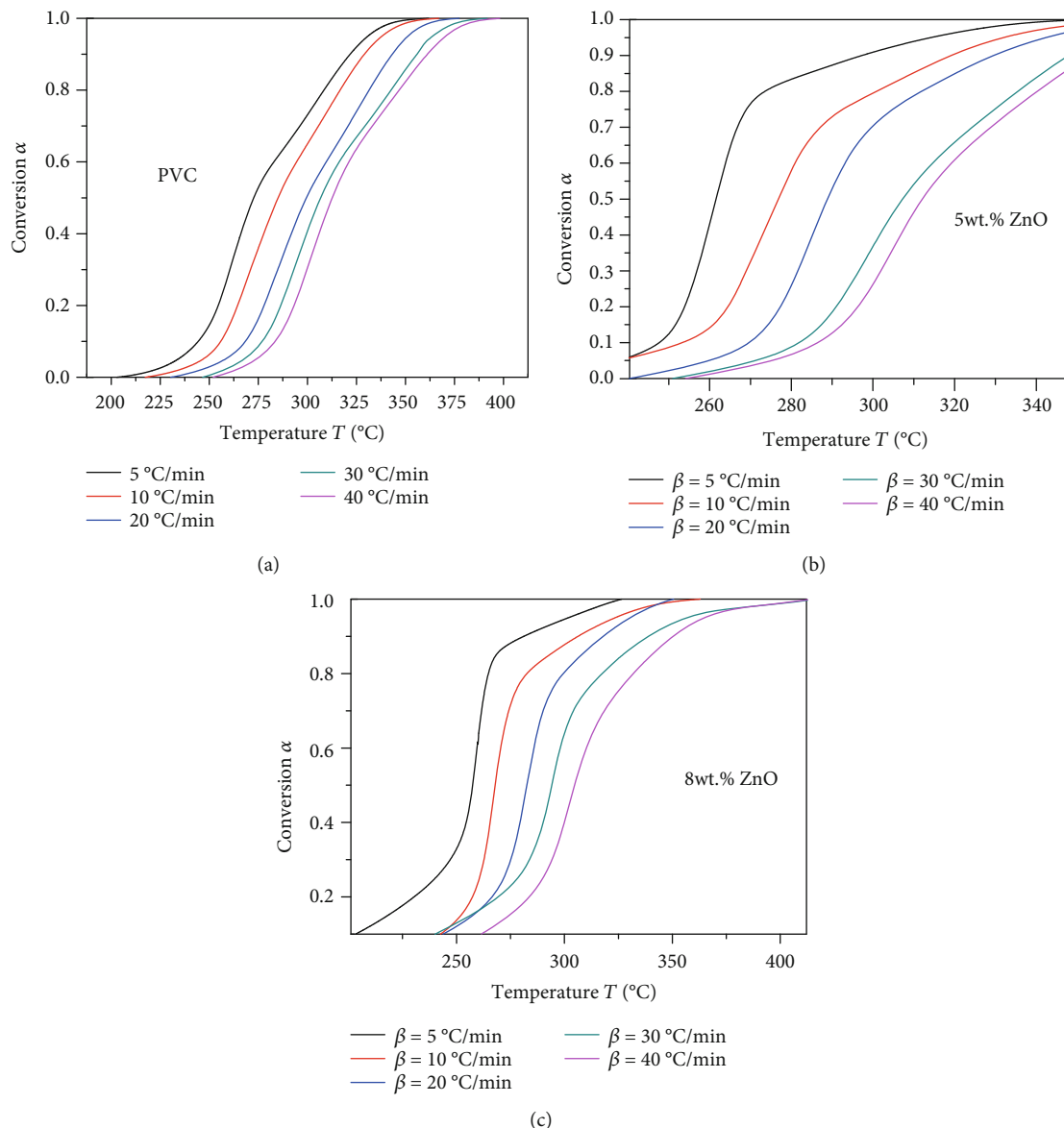


FIGURE 5: Temperature dependence of conversion α for (a) pure PVC, (b) 5 wt.% ZnO, and (c) 8 wt.% ZnO samples.

TABLE 1: The extracted data of the Kissinger model for pure PVC.

Sample	Peak	Intercept value	Preexponential A (min^{-1})	Slope value	Activation energy E_a (kJ/mol)	Statistics R^2
PVC	1	16.47	2.07×10^8	-14.59	121.31	0.98508
	2	13.20	7.54×10^6	-13.88	115.41	0.97
5 wt.% ZnO	1	14.41	2.46×10^7	-13.52	112.41	0.97
8 wt.% ZnO	1	15.04	4.68×10^7	-13.81	114.82	0.99

3. Sample Preparation

Polyvinyl chloride (PVC) (Saudi Basic Industries Corporation (SABIC), MW of 30,000) and ZnO nanoparticles (Sigma-Aldrich Chemicals; <100 nm) are used for sample preparation. PVC (1 g) was dissolved in 15 mL of THF at

room temperature ($\approx 23^\circ\text{C}$) using a magnetic stirrer for 4 hours. Zinc oxide nanoparticles were mixed with 1 mL of distilled water to obtain a paste of water-saturated nanoparticles. The obtained paste was transferred to a filter paper to remove excess water and left to dry at room temperature for two hours. The paste was ultrasonicated in 3 mL of THF

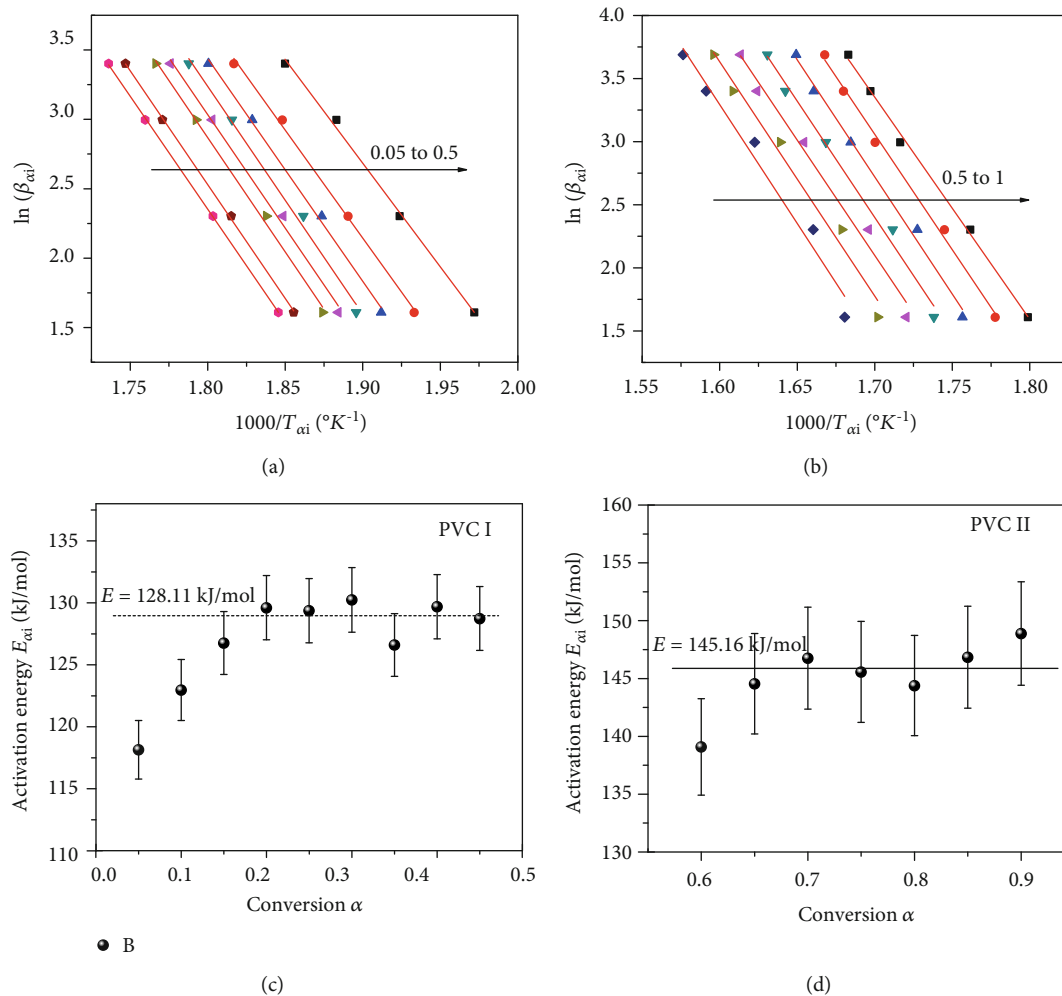


FIGURE 6: $\ln(\beta_{ai})$ vs. $1/T_{ai}$ for (a) pure PVC region I and (b) pure PVC region II and the dependence of activation energy on the conversion α for (c) pure PVC region I and (d) pure PVC region II.

solvent for 15 minutes. The dispersed pretreated ZnO was added to the prepared PVC-THF solution and ultrasonicated for three hours to ensure the homogeneity of the mixture. The mixture was transferred to the magnetic stirrer and stirred overnight to ensure homogeneity of the nanoparticle's distribution within the polymer. The mixture was poured into Petri dishes at a radius of six centimeters and left to dry for three days.

4. Results and Discussion

4.1. Thermal Gravimetric Analysis. Thermal gravimetric analysis (TGA) for pure PVC and PVC-ZnO nanocomposite (5 wt.% and 8 wt.% water-treated ZnO) was carried out using TA instruments Q500 (USA). All measurements were carried out in the temperature range 25–600°C with different scan rates with nitrogen purge at a flow rate of 60 mL/min. The sample weight was about 12 mg for all samples.

As revealed in several previous works [1, 11, 27, 28], the decomposition curve for pure PVC polymer consists of three main decomposition regions which are represented as three peaks in DTGA complex curve. The 1st main decomposition

process of PVC consists of two subsequent processes. These two processes are confined in the temperature range from about 175 to 375°C. The second main decomposition is confined between 350 and 550°C. The 1st stage corresponds to the evolution of hydrogen chloride causing formation of polyene structure while the 2nd stage is attributed to the thermal cracking of the carbonaceous-conjugated polyene sequences [7].

Samples loaded with treated zinc oxide nanoparticles have the same decomposition behavior as pure PVC sample except a DTGA peak near 200°C which can possibly be attributed to the direct chlorination of ZnO by the PVC monomer [29]. It is noted that nanocomposite samples have less thermal stability during the low-temperature stage (50 to 350°C). The mass loss at 225°C was about 10%, 13%, and 16% for the pure PVC, 5 wt.% ZnO, and 8 wt.% ZnO samples, respectively. The addition of treated ZnO accelerates the initiation of HCl. The formation of HCl accelerates the formation of double bond sequences in the polymer backbone [1, 7]. The rate of formation of HCl depends strongly on the presence of oxygen [11, 28]. Decomposition of water molecules adsorbed on ZnO particles will increase the HCl

TABLE 2: The extracted data of the FWO model for both reaction regions of pure PVC.

Alpha PVC	Intercept value	Preexponential A (min ⁻¹)	Slope value	Activation energy E_a (kJ/mol)	Statistics Adj. R^2	Average
PVC region 1						
0.05	31.08	4.7210 ¹⁴	-14.95	118.15	1.00	
0.1	31.70	9.1310 ¹⁴	-15.56	122.97	1.00	
0.15	32.31	1.7210 ¹⁵	-16.04	126.76	1.00	
0.2	32.76	2.7710 ¹⁵	-16.40	129.61	0.99	
0.25	32.50	2.1310 ¹⁵	-16.37	129.37	0.99	128.11
0.3	32.53	2.2110 ¹⁵	-16.48	130.24	1.00	
0.35	33.00	3.7310 ¹⁵	-16.40	126.60	0.98	
0.4	32.07	1.3910 ¹⁵	-16.41	129.69	1.00	
0.45	31.67	9.2710 ¹⁴	-16.29	128.74	1.00	
PVC region 2						
0.6	33.27	4.9610 ¹⁵	-17.60	139.09	1.00	
0.65	34.14	1.2310 ¹⁶	-18.29	144.55	0.99	
0.7	34.29	1.4410 ¹⁶	-18.57	146.76	0.99	
0.75	33.72	8.1110 ¹⁵	-18.42	145.57	0.99	145.16
0.8	33.16	4.6210 ¹⁵	-18.27	144.39	0.98	
0.85	33.36	5.7010 ¹⁵	-18.58	146.84	0.98	
0.9	33.44	6.2910 ¹⁵	-18.84	148.89	0.97	

formation due to the production of oxygen atoms. There are several references which studied the effect of zinc oxide on the thermal stability of PVC. For example, Lewis acids (e.g., ZnCl₂ and FeCl₃) [30–34] can accelerate and lower the activation energy of PVC degradation. Also, according to Zhang et al. [29], ZnO can react with HCl or directly with the PVC monomer. ZnCl₂ can form and catalyze the dehydrochlorination of PVC [35, 36], resulting in a lower activation energy. Finally, all these factors will lead to the reduction of thermal stability for the low-temperature degradation stage.

The rate of formation of HCl depends strongly on the presence of oxygen [11, 37, 38]. Decomposition of water molecules adsorbed on ZnO particles will increase the HCl formation due to the production of oxygen atoms. This will lead to the reduction of the thermal stability for the low-temperature degradation stage [37, 38].

For the high-temperature range, it is observed that the thermal stability of the samples increases by increasing the weight ratio of ZnO nanoparticles. This behavior may be attributed to the following two reasons. The first is that the number of double bond formation increases, which contributes to the thermal isolation for the remaining polymeric chains. By this way, the double bond (polyenes) structure will protect the remaining chains from degradation and increase the thermal stability. The second is that metal oxides act as adsorbents for HCl or as inhibitors of HCl formation due to their reaction with HCl, which in turn increases the thermal stability of the material [1].

4.2. Kinetic Thermal Analysis for Pure PVC and PVC/ZnO Nanocomposite. Kinetic thermal analysis for pure PVC and PVC/ZnO nanocomposite samples (Figures 1) was investi-

gated using the data collected by TGA measurements. Measurements were performed at different heating rates (5, 10, 20, 30, and 40°C/min) for temperature ranging from 40 to 550°C. Using the previous equations (equations (1)–(3)) of the three models (Kissinger, Flynn-Wall-Ozawa, and Kissinger-Akahira-Sunose models), the kinetic parameters for pure PVC and PVC/ZnO were calculated.

Figures 2(a)–2(c) represent the TGA spectra for pure PVC and 5 wt.% and 8 wt.% PVC/ZnO nanocomposite at different heating rates, respectively. Figures 3(a)–3(c) illustrate the corresponding DTGA spectra for these samples.

4.2.1. Kissinger Model. In the Kissinger model, the temperature corresponding to the maximum decomposition rate (T_p) was determined from the DTGA curves for each heating rate. By applying the Kissinger model to the 1st main decomposition processes (225 to 400°C), the relationship between $\ln(\beta/T_p^2)$ and $1/T_p$ for pure PVC and 5 wt.% and 8 wt.% PVC/ZnO was plotted and is shown in Figures 4(a)–4(c), respectively. The slope and the intercept of the straight line were determined to calculate the activation energy and the preexponential factor. The extracted data are recorded in Table 1. For nanocomposite samples, the second reaction within this temperature range was overlapped with the first reaction in a way that does not allow us to define the peak temperature for each curve, and therefore, we were unable to apply the model to this reaction region.

It is noted that the activation energies for the 1st reaction peak reduced due to the addition of ZnO nanoparticles. For pure PVC, E_a was found to be about 121 kJ/mol while for nanocomposite samples it was about 112 kJ/mol for 5 wt.% ZnO and about 114 kJ/mol for 8 wt.% ZnO sample.

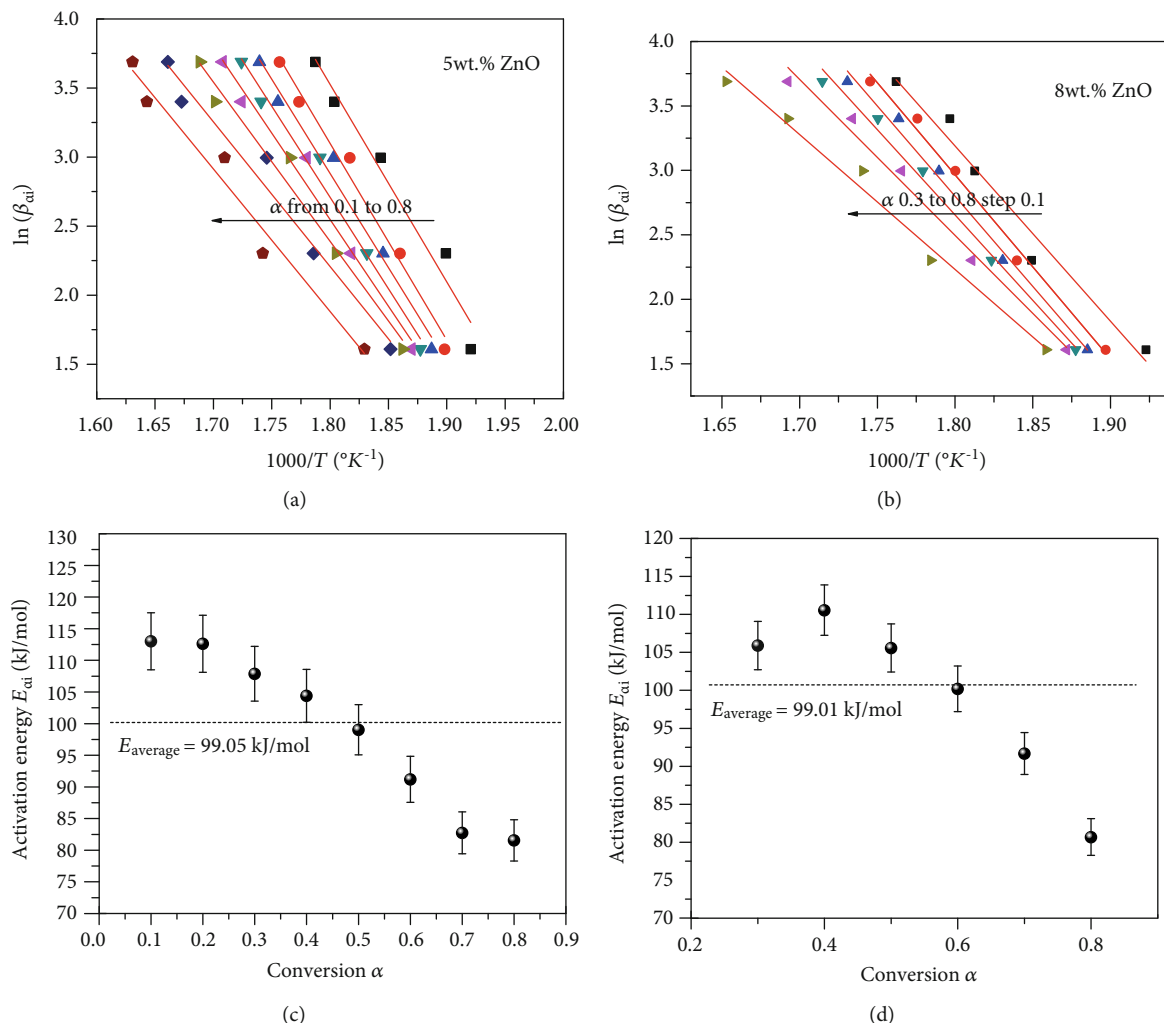


FIGURE 7: $\ln(\beta_{ai})$ vs. $1/T_{ai}$ for (a) 5wt.% PVC/ZnO and (b) 8wt.% PVC/ZnO samples and the dependence of activation energy on the conversion (α) for (c) 5 wt.% PVC/ZnO and (d) 8 wt.% PVC/ZnO samples.

4.2.2. Flynn-Wall-Ozawa Model. The Flynn-Wall-Ozawa model was used to calculate the activation energy of pure PVC and nanocomposite samples and compare it with the values calculated from the Kissinger model. By assuming that the value of $g(\alpha)$ is constant at each value of α and by drawing the relationship between $\ln(\beta_{ai})$ and $1/T_{ai}$ at different values of α , one can determine the activation energy E_{ai} for each value of α .

Figure 5 shows the conversion with temperature for pure and nanocomposite samples, considering that the range of reaction is a one-step transition. It is noted that the behavior of the conversion curve depends on the weight ratio of zinc oxide nanoparticles. In the case of the pure PVC sample, there were two regions with different rates of conversion and different reaction speeds. However, because of the inhibition role of ZnO to HCl formation, the conversion curve became a one-step reaction form with a little deviation at the edges of the curve. These sets of curves were used to investigate the relationship between $\ln(\beta_{ai})$ and $1/T_{ai}$ and determine the activation energies and preexponential factors.

Figures 6(a) and 6(b) illustrate the relation between $\ln(\beta_{ai})$ and $1/T_{ai}$ of PVC for both reaction regions. The calculated values of E_a as function of conversion α for both reaction regions are represented in Figures 6(c) and 6(d). The activation energy for the first reaction region varies from 118 to 128 kJ/mol with an average value of 128 kJ/mol, while the activation energy for the second reaction region changed from 139 to 149 kJ/mol with an average value of 145 kJ/mol. By comparing those values with the values obtained from the Kissinger model, we find that they are higher by 5% to 20%, respectively. Table 2 shows the extracted data of the FWO model for both reaction regions of pure PVC sample.

Figures 7(a)–7(d) represent $\ln(\beta_{ai})$ vs. $1/T_{ai}$ and the dependence of E_a on α for 5 wt.% and 8 wt.% PVC/ZnO nanocomposite samples. As shown in Figures 7(c) and 7(d), it is noted that the activation energy for 5 wt.% ZnO sample varied from 113 kJ/mol to 81 kJ/mol with an average of 99.05 kJ/mol. On the other side, E_a for the sample loaded with 8 wt.% ZnO varied from 106 kJ/mol to 81 kJ/mol with an average of 99.01 kJ/mol.

TABLE 3: The extracted data of the FWO model for both 5 wt.% and 8 wt.% PVC/ZnO nanocomposite samples.

Alpha	Intercept value	Preexponential A (min ⁻¹)	Slope value	Activation energy E _a (kJ/mol)	Statistics Adj. R ²	Average
PVC/5 wt.% ZnO						
0.1	29.27	7.3810 ¹³	-14.30	113.01	0.96	99.05
0.2	28.75	4.3510 ¹³	-14.25	112.62	0.98	
0.3	27.45	1.1410 ¹³	-13.65	107.88	0.98	
0.4	26.49	4.2310 ¹²	-13.21	104.40	0.98	
0.5	25.11	1.0010 ¹²	-12.53	99.03	0.98	
0.6	23.16	1.3110 ¹¹	-11.54	91.20	0.97	
0.7	21.06	1.4710 ¹⁰	-10.47	82.74	0.97	
0.8	20.46	7.8910 ⁹	-10.32	81.56	0.96	
PVC/8 wt.% ZnO						
0.3	27.38	1.04 × 10 ¹³	-13.4	105.90	0.98	99.01
0.4	28.22	2.51 × 10 ¹³	-13.99	110.56	0.99	
0.5	26.91	6.50 × 10 ¹²	-13.36	105.58	0.98	
0.6	25.54	1.57 × 10 ¹²	-12.68	100.21	0.98	
0.7	23.43	1.74 × 10 ¹¹	-11.60	91.68	0.97	
0.8	20.67	9.72 × 10 ⁹	-10.21	80.69	0.98	

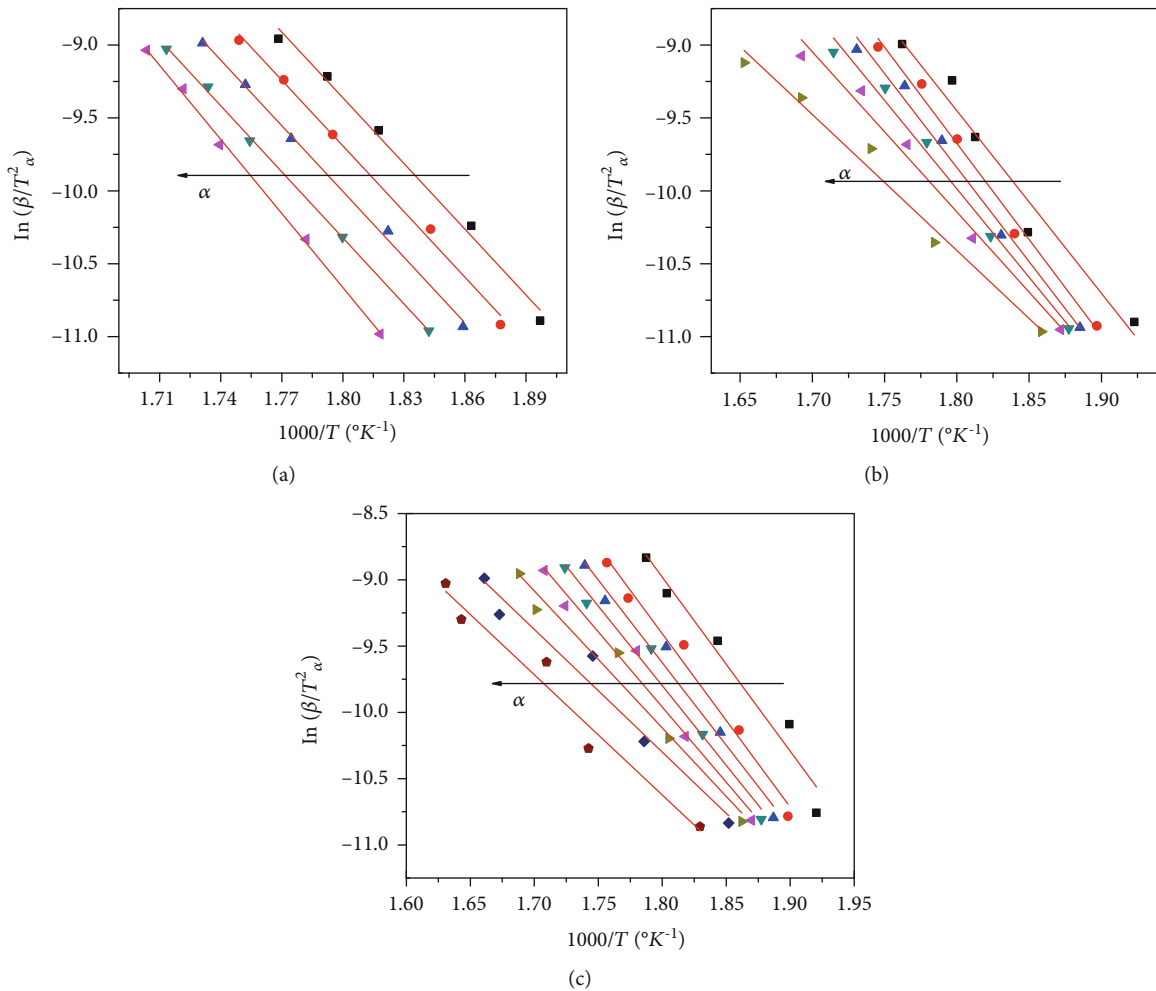


FIGURE 8: $\ln(\beta/T_{ai}^2)$ vs. $1/T_{ai}$ for (a) pure PVC, (b) 5 wt.% PVC/ZnO, and (c) 8 wt.% PVC/ZnO samples.

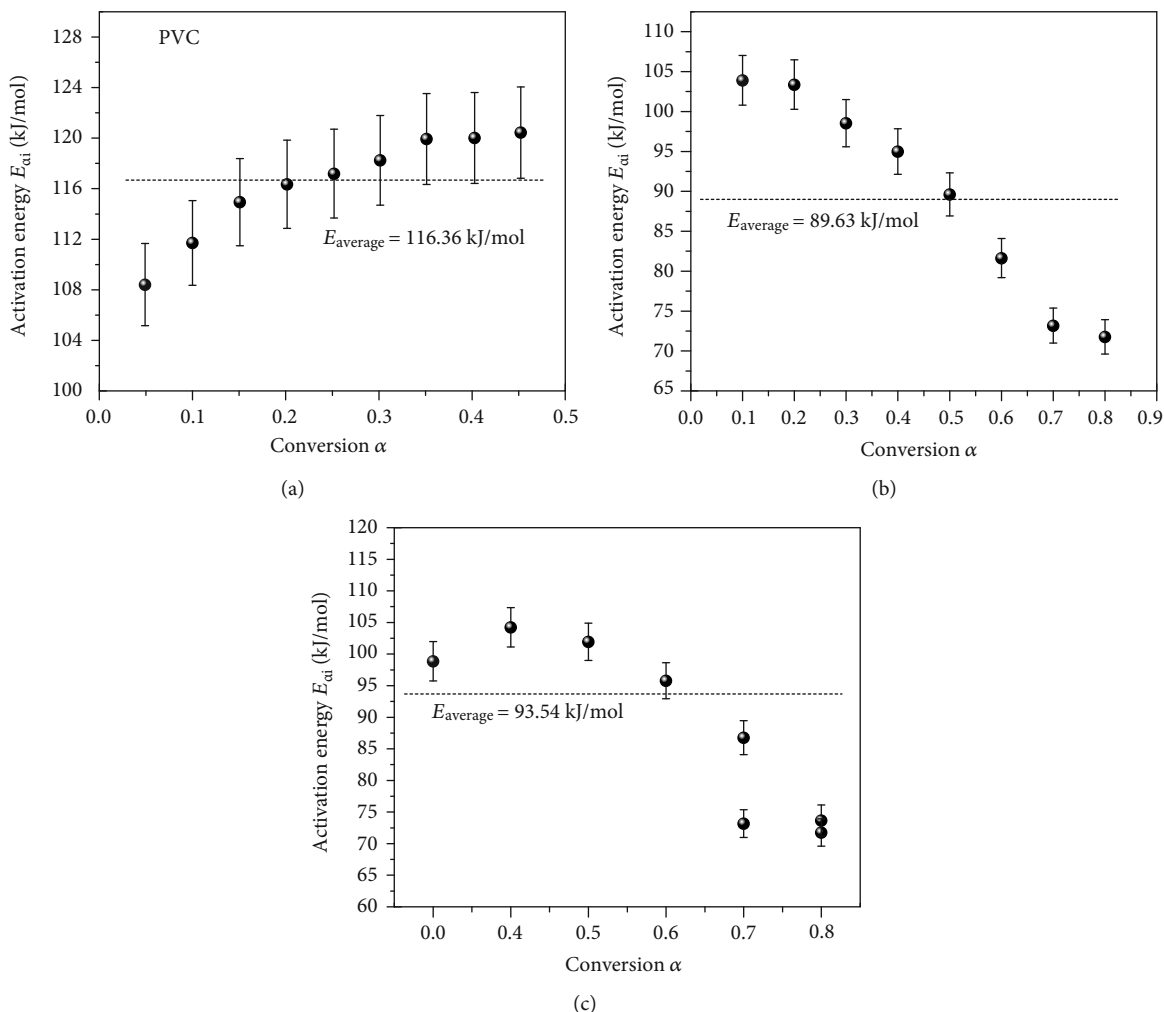


FIGURE 9: The dependence of activation energy on the conversion α for (a) pure PVC, (b) 5 wt.% PVC/ZnO, and (c) 8 wt.% PVC/ZnO samples.

Table 3 shows the extracted data of the FWO model for both 5 wt.% and 8 wt.% PVC/ZnO nanocomposite samples. The average activation energies for both nanocomposite samples are nearly equal to 99 kJ/mol and are less than that obtained by using the Kissinger model (≈ 112 and 114 kJ/mol). From the table, we observe that the average of the activation energy values corresponding to intermediate values of α (0.3 to 0.5) is the nearest to the predicted value using the Kissinger model, while small and large α values have activation energy less or greater than that predicted by the Kissinger model. This means that if we neglect the two edges of conversion curve we will have average values for activation energy closed to that predicted by the Kissinger model because we will reduce the errors due to the overlapping of the two decomposition processes.

4.2.3. Kissinger-Akahira-Sunose (KAS). The relationship between $\ln(\beta/T_{oi}^2)$ and $1/T_{oi}$ at different values of α are illustrated in Figure 8 for pure PVC and PVC/ZnO nanocomposites. The dependence of the calculated activation energies on conversion α for pure and nanocomposite sam-

ples is illustrated in Figure 9. The average activation energies for pure, 5 wt.%, and 8 wt.% ZnO nanoparticles were 116.4, 89.6, and 93.5 kJ/mol, respectively. Table 4 shows the extracted data of the KAS model for PVC and 5 wt.% and 8 wt.% PVC/ZnO nanocomposite samples.

From the obtained results, the addition of zinc nanoparticles led to a decrease in the thermal stability of the samples during the low-temperature range ($T < 350^\circ\text{C}$), which was investigated with kinetic thermal analysis models. The kinetic thermal analysis showed that the activation energy of the samples decreased by adding ZnO nanoparticles significantly through both FWO and KSA models. These results are consistent with the results of thermal stability, which were explained based on the contribution of oxygen emitted from the decomposition of adsorbed water on ZnO nanoparticle surface in accelerating the HCl formation (at low-temperature region) besides the role of ZnO chlorination in accelerating the decomposition process. At the high-temperature region, ZnO nanoparticles play an important role in inhibiting the role of HCl in the decomposition process of the polymer [29].

TABLE 4: The extracted data of the KAS model for PVC and 5 wt.% and 8 wt.% PVC/ZnO nanocomposite samples.

Alpha PVC	Intercept value	Preexponential A (min ⁻¹)	Slope value	Activation energy E_a (kJ/mol)	Statistics Adj. R^2	Average
PVC region 1						
0.05	16.29	1.63×10^8	-13.76	108.75	1.00	
0.1	16.52	2.11×10^8	-14.16	111.91	1.00	
0.15	16.94	3.29×10^8	-14.54	114.91	1.00	
0.2	17.08	3.86×10^8	-14.73	116.41	0.99	
0.25	17.05	3.76×10^8	-14.82	117.12	0.99	116.36
0.3	17.13	4.13×10^8	-14.96	118.23	1.00	
0.35	17.37	5.29×10^8	-15.17	119.89	1.00	
0.4	17.23	4.63×10^8	-15.19	120.05	1.00	
0.45	17.03	3.77×10^8	-15.18	119.97	1.00	
PVC region 2						
0.6	18.56	1.90×10^9	-16.45	130.01	1.00	
0.65	19.41	4.62×10^9	-17.12	135.30	0.99	
0.7	19.53	5.30×10^9	-17.39	137.43	0.99	
0.75	18.94	2.91×10^9	-17.23	136.17	0.99	135.74
0.8	18.37	1.62×10^9	-17.07	134.90	0.98	
0.85	18.54	1.96×10^9	-17.36	137.20	0.97	
0.9	18.60	2.11×10^9	-17.61	139.17	0.96	
PVC/5 wt.% ZnO						
0.1	14.69	3.14×10^7	-13.15	103.92	0.95	
0.2	14.13	1.79×10^7	-13.08	103.37	0.98	
0.3	12.82	4.59×10^6	-12.47	98.55	0.98	
0.4	11.84	1.68×10^6	-12.02	94.99	0.97	
0.5	10.45	3.90×10^5	-11.34	89.62	0.97	89.63
0.6	8.48	4.96×10^4	-10.33	81.64	0.96	
0.7	6.36	5.35×10^3	-9.26	73.18	0.96	
0.8	5.72	2.78×10^3	-9.08	71.76	0.95	
PVC/8 wt.% ZnO						
0.3	13.07	5.95×10^6	-12.51	98.87	0.95	
0.4	14.06	1.69×10^7	-13.19	104.24	0.99	
0.5	13.39	8.40×10^6	-12.90	101.95	0.99	
0.6	11.83	1.67×10^6	-12.12	95.78	0.99	93.54
0.7	9.62	1.66×10^5	-10.98	86.78	0.98	
0.8	6.37	5.46×10^3	-9.32	73.66	0.98	

4.3. *AC Conductivity.* Figure 10 shows the variation in AC conductivity as a function of frequency at different temperatures (30 to 110°C) for pure PVC and PVC-ZnO nanocomposite films (5 wt.% and 8 wt.%). It is observed that all the prepared samples exhibit the same behavior but with different values over the whole range of measured frequency. The Jonscher universal power law (equation (4)) [39] was used to investigate the frequency dependence of conductivity

for such nanocomposite. The total electrical conductivity $\sigma(\omega)$ is composed of the summation of AC ($\sigma_{ac}(\omega)$) and DC ($\sigma_{dc}(0)$) conductivities, and according to the Jonscher power law, the frequency dependence of total conductivity can be written as

$$\sigma(\omega) = \sigma_{dc}(0) + \sigma_{ac}(\omega) = \sigma_{dc} + A \omega^s. \quad (4)$$

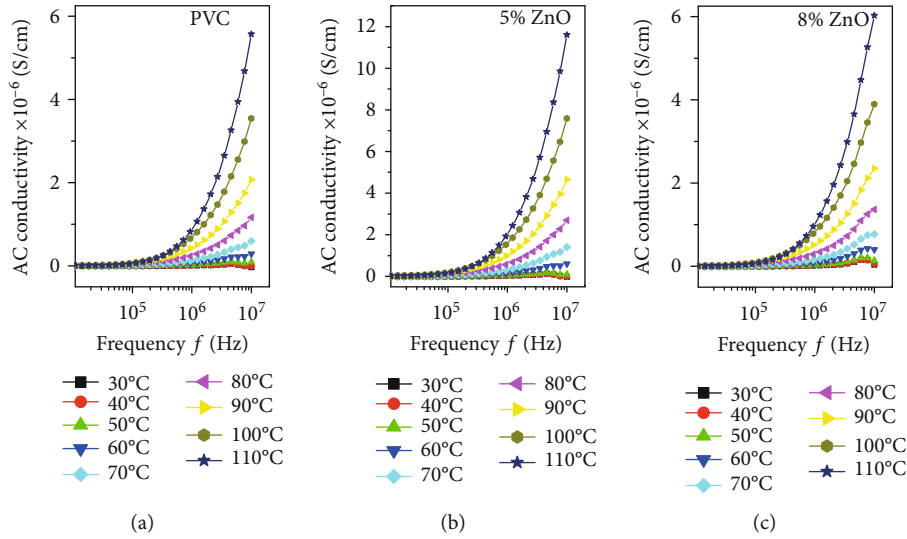


FIGURE 10: Variation of AC conductivity (σ_{ac}) with frequency for (a) pure PVC, (b) 5% ZnO, and (c) 8% ZnO nanocomposite films.

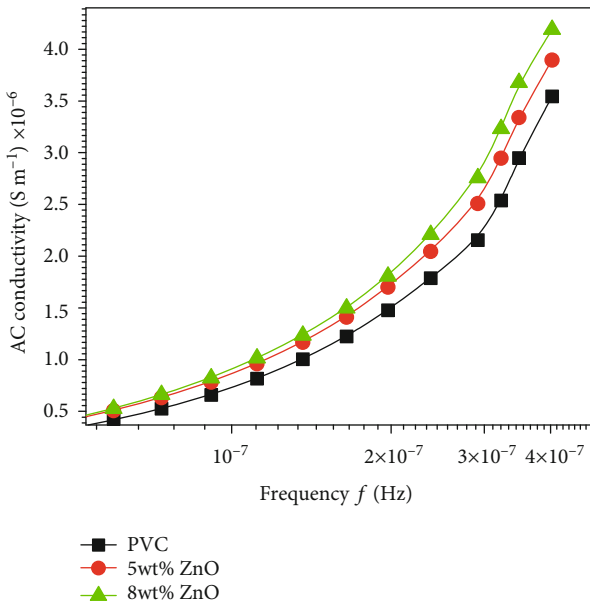


FIGURE 11: AC conductivity for pure PVC and PVC/ZnO nanocomposite samples.

The DC conductivity part is frequency independent while AC conductivity is the frequency-dependent part. Coefficient “A,” which represents the strength of polarizability, is a temperature-dependent constant. The power law exponent (s) (which generally varies between 0 and 1) is also temperature dependent. The exponent “ s ” denotes to the degree of interaction between carriers and lattice or surrounding molecules. A lower value of s indicates the increase in σ_{dc} contribution [40].

It is noted that the AC conductivity increased and the temperature-independent region decreases with temperature for all samples. Also, the AC electrical conductivity increases with increasing ZnO NPs (Figure 11). The increase of the conductivity with ZnO wt.% can be regarded to the increase in the number of charge carriers which are able to contribute

in the conduction mechanism. Moreover, the presence of ZnO NPS may contribute in decreasing the chain agglomeration of the host polymer. In addition, the increase of the conductivity can be considered as an indicator to the homogenous dispersion of the filler (ZnO NPs) through the host polymer which emphasizes the absence of aggregation of the filler (which causes reduction in conductivity and acts as trap centers for the free charge carrier) within the prepared samples.

To illustrate the behavior of samples, Figures 12–14 show the behavior of pure PVC and nanocomposite samples (5 wt.% and 8 wt.%) through five frequency bands. It is noted that for the low-frequency band there are no detectable relaxation peaks and this attributed to the rule of the DC conductivity. For both intermediate- and high-frequency bands, the AC conductivity values corresponding to the relaxation peaks increase with increasing frequency in addition to the shift to higher temperatures. The peak symmetry (for high-frequency range) indicates a single relaxation process.

The coefficients A and S obtained by applying the Jonscher universal power law and fitting using Origin software version 8.5 are illustrated in Figure 15. As observed from the figure, the values of coefficient S lie between 1 and 0.65. Coefficient “ S ” signifies the degree of interaction between chains in pure PVC samples and represents both interactions between chains of host polymer with each other and between host polymer chain and filler for composite samples. The behavior of the S coefficient related to the host polymer glass transition (T_g about 85°C) because the chain interaction of chain filler interaction depends on temperature [41]. Below T_g , PVC chains have less degree of freedom to contribute to AC and DC due to impurity and space charge becomes the predominant factor. During this stage, we noted that S decreases with temperature up to the temperature where the chains become able to move (T_g) after which coefficient S starts increasing with temperature. The AC conductivity above T_g represents the predominant conduction mechanism. The interaction between chains and filler appears as shift in the S - T curve to higher

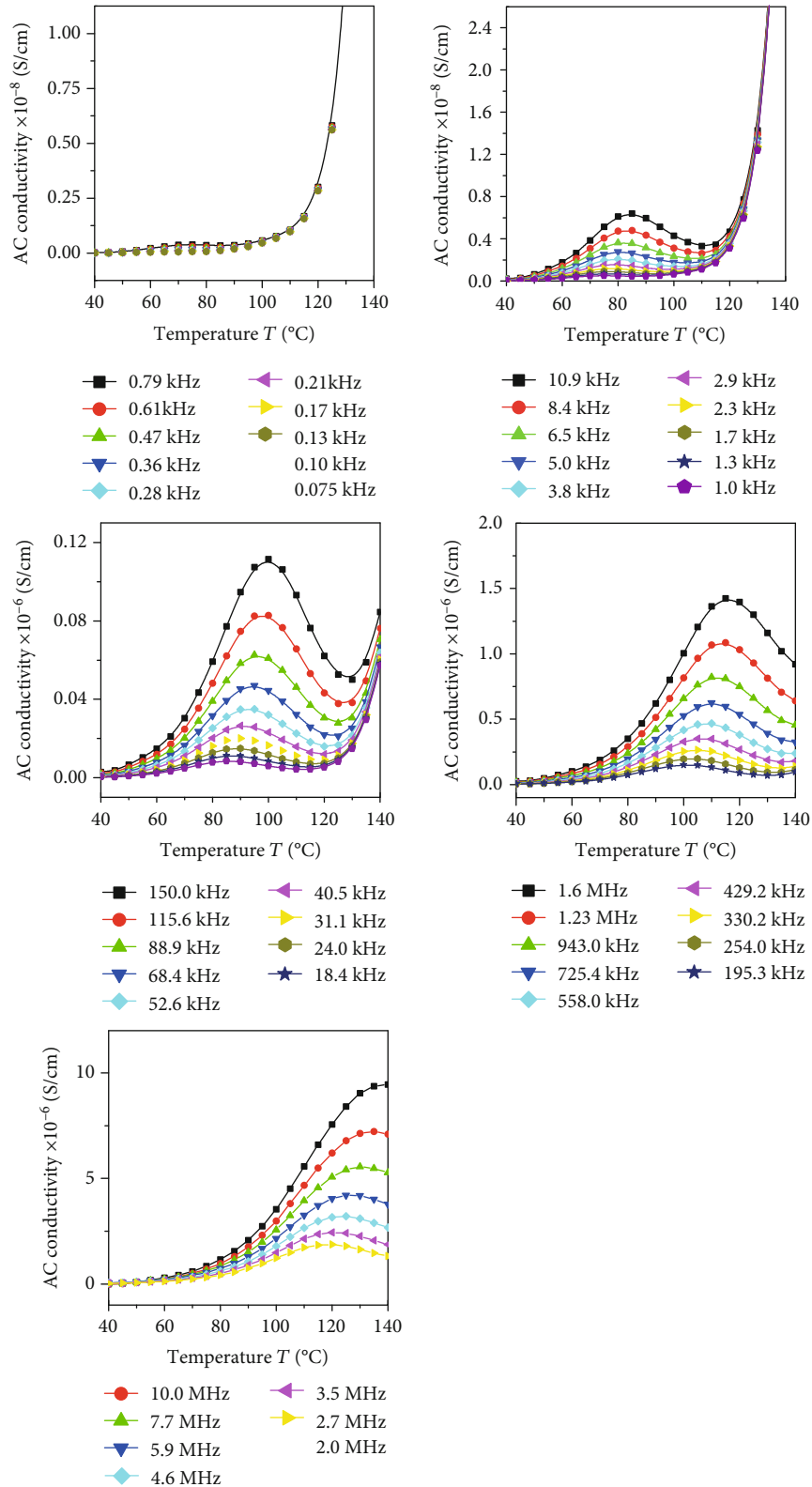


FIGURE 12: AC conductivity for pure PVC sample at difference frequency ranges.

temperature. The conduction above T_g will be due to the segmental chain movement, and the presence of ZnO will facilitate such motion.

It is noted that the behavior of coefficient “A” is contrary to that of coefficient “S” (coefficient A increases with temperature and then decreases), and this is normal where before T_g

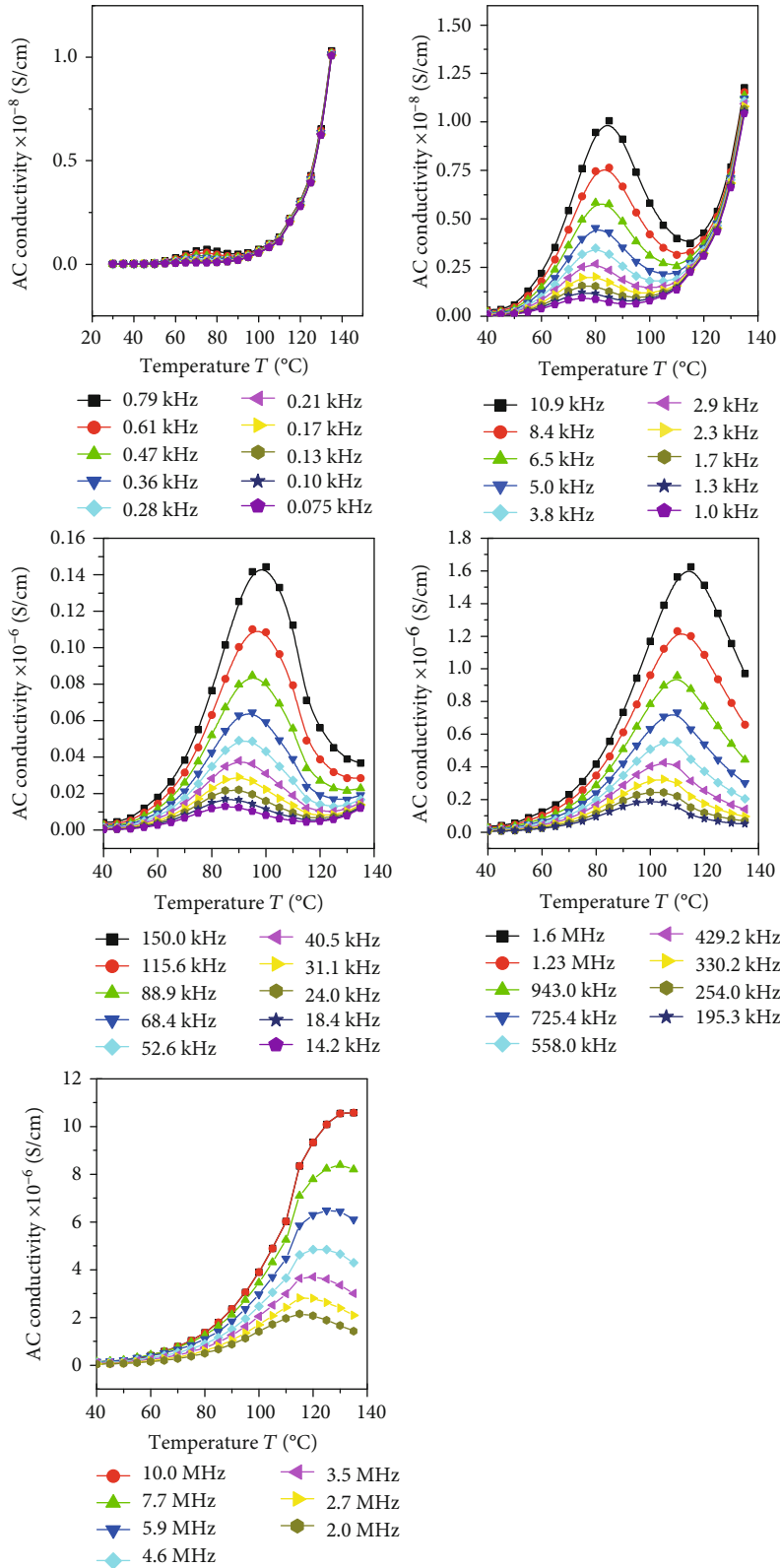


FIGURE 13: AC conductivity for pure 5 wt.% PVC/ZnO nanocomposite sample at difference frequency ranges.

charge carriers have the ability to be polarized and to arrange themselves, while above T_{seg} the degree of randomness increases and the AC conduction due to chain motion

becomes predominant. The temperature corresponding to the maximum value of coefficient “A” is slightly changed (93 to 95°C).

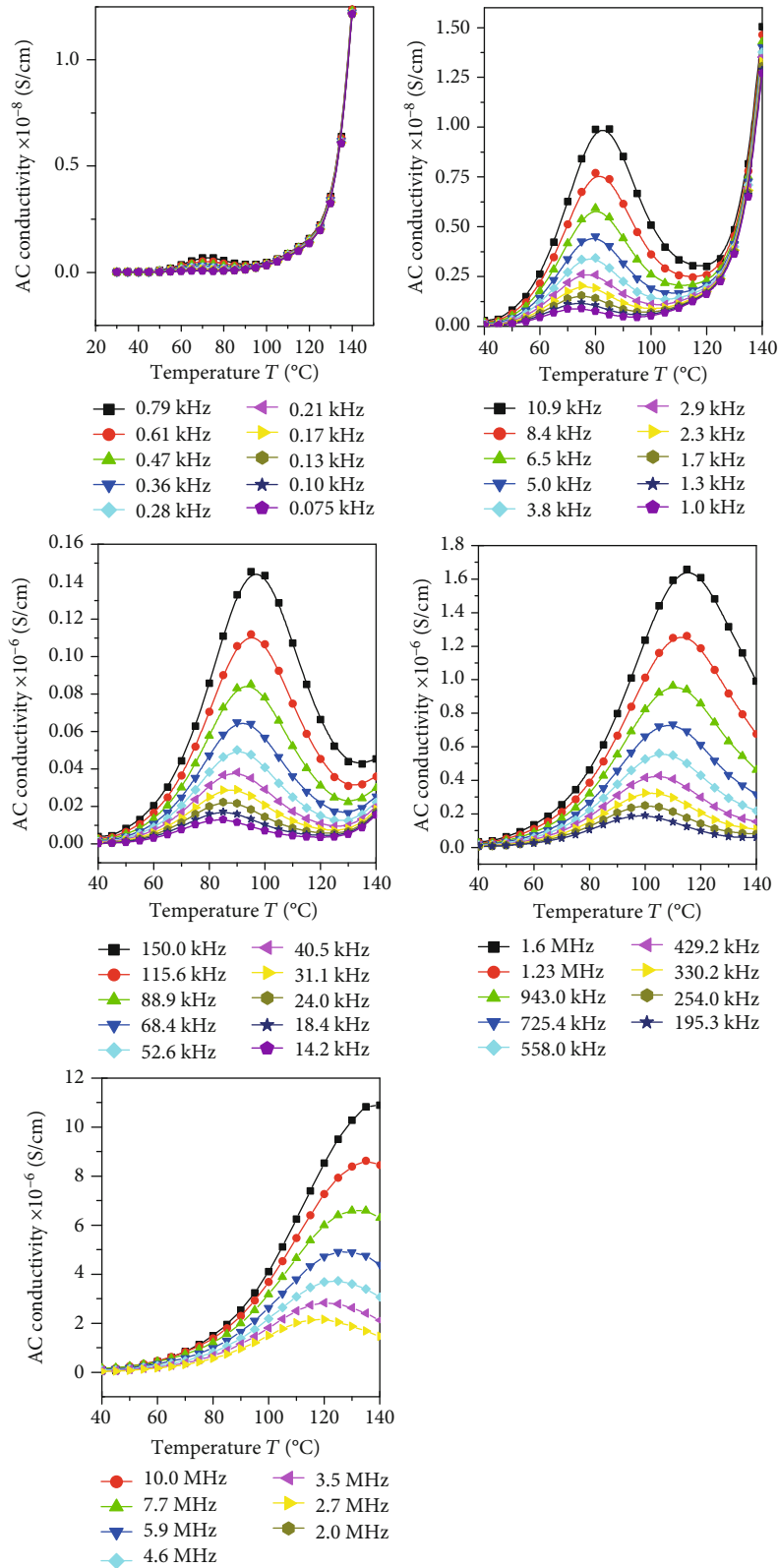


FIGURE 14: AC conductivity for pure 8 wt.% PVC/ZnO nanocomposite sample at difference frequency ranges.

5. Conclusion

Polymer nanocomposite samples composed of distilled water-treated ZnO nanoparticles and PVC polymer were

prepared by casting method. The thermal stability of the samples was studied, and the samples were found to undergo a decrease in thermal stability during the low-temperature range (up to 350°C). The thermal stability of the samples

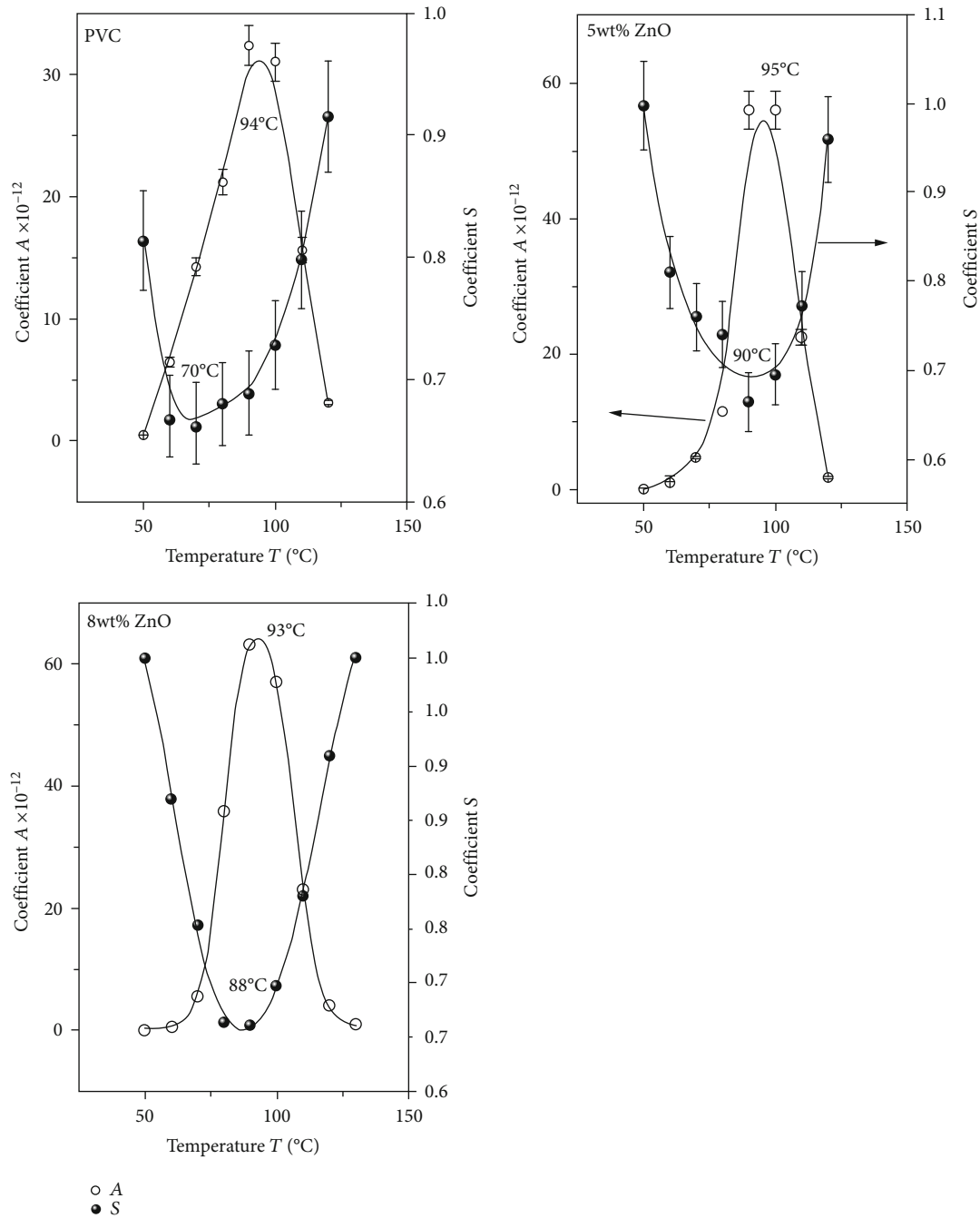


FIGURE 15: Temperature dependence of S and A coefficients for PVC pure and PVC/ZnO nanocomposite.

increased at temperatures higher than 350°C. The results of thermal stability interpreted taking into account the role of adsorbed water on the ZnO surface. The adsorbed water accelerates HCl formation, thus decreasing the thermal stability. At the high-temperature range, the effective role of ZnO in inhibiting HCl formation leads to increased thermal stability. The nonisothermal kinetic analysis of PVC/ZnO nanocomposite samples was investigated by the Kissinger, Flynn-Wall-Ozawa, and Kissinger-Akahira-Sunose models. Although the conditions of derivative for each model are different, the variation between the results was at the acceptable level. The deviation between the Akahira-Sunose and FWO

models was less than 9%, which is close to the difference between the Kissinger model and the FWO model (11%). All results are also consistent with lower activation energy of polymer after adding the zinc oxide nanoparticles. The AC conductivity as function of frequency and temperature was also investigated. The addition of ZnO nanoparticle increased the AC conductivity, and the temperature-independent region decreased by increasing temperature. Both S and A coefficients were predicted using the Jonscher power law and OriginLab software. The trends of S and A coefficients were discussed based on the glass transition of the host polymer.

Data Availability

The data used to support the findings of this study are available from the corresponding author upon request.

Conflicts of Interest

The authors declare that they have no conflicts of interest.

Acknowledgments

The author acknowledges the Deanship of Scientific Research at King Faisal University for the financial support under Nasher Track (Grant No. 186052).

References

- [1] J. Yu, L. Sun, C. Ma, Y. Qiao, and H. Yao, "Thermal degradation of Pvc: a review," *Waste Management*, vol. 48, pp. 300–314, 2016.
- [2] M. Hajibeygi, M. Maleki, M. Shabaniyan, F. Ducos, and H. Vahabi, "New polyvinyl chloride (Pvc) nanocomposite consisting of aromatic polyamide and chitosan modified Zn nanoparticles with enhanced thermal stability, low heat release rate and improved mechanical properties," *Applied Surface Science*, vol. 439, pp. 1163–1179, 2018.
- [3] T. A. Taha, Z. Ismail, and M. M. Elhawary, "Structural, optical and thermal characterization of PVC/SnO₂ nanocomposites," *Applied Physics A*, vol. 124, no. 4, p. 307, 2018.
- [4] S. Mallakpour and M. Darvishzadeh, "Nanocomposite materials based on poly(vinyl chloride) and bovine serum albumin modified Zn through ultrasonic irradiation as a green technique: optical, thermal, mechanical and morphological properties," *Ultrasonics Sonochemistry*, vol. 41, pp. 85–99, 2018.
- [5] S. Mallakpour and S. Shamsaddinimotlagh, "Ultrasonic-promoted rapid preparation of Pvc/TiO₂-Bsa nanocomposites: characterization and photocatalytic degradation of methylene blue," *Ultrasonics Sonochemistry*, vol. 41, pp. 361–374, 2018.
- [6] M. Hajibeygi, M. Maleki, and M. Shabaniyan, "The effects of poly (amide-imide) coating on the thermal, combustion and mechanical properties of polyvinyl chloride ZnO nanocomposites," *Progress in Organic Coatings*, vol. 122, pp. 96–106, 2018.
- [7] M. Dastpaki and H. A. Khonakdar, "Thermal, thermomechanical, and morphological characterization of poly (vinyl chloride)(Pvc)/ZnO nanocomposites: Pvc molecular weight effect," *Journal of Vinyl and Additive Technology*, vol. 25, no. s2, pp. E63–E71, 2019.
- [8] T. A. Taha, "Optical and thermogravimetric analysis of Pb3O4/Pvc nanocomposites," *Journal of Materials Science: Materials in Electronics*, vol. 28, no. 16, pp. 12108–12114, 2017.
- [9] Y. Sun, M. Gao, Z. Chai, and H. Wang, "Thermal behavior of the flexible polyvinyl chloride including montmorillonite modified with iron oxide as flame retardant," *Journal of Thermal Analysis and Calorimetry*, vol. 131, no. 1, pp. 65–70, 2018.
- [10] Y. Turhan, M. Doğan, and M. Alkan, "Characterization and some properties of poly (vinyl chloride)/sepiolite nanocomposites," *Advances in Polymer Technology*, vol. 32, Supplement 1E82 pages, 2013.
- [11] P. E. Sánchez-Jiménez, A. Perejón, J. M. Criado, M. J. Diáñez, and L. A. Pérez-Maqueda, "Kinetic model for thermal dehydrochlorination of poly(vinyl chloride)," *Polymer*, vol. 51, no. 17, pp. 3998–4007, 2010.
- [12] J. Huang, X. Li, G. Zeng, X. Cheng, H. Tong, and D. Wang, "Thermal decomposition mechanisms of poly (vinyl chloride): a computational study," *Waste Management*, vol. 76, pp. 483–496, 2018.
- [13] M. Al-Harashsheh, A. Al-Otoom, L. Al-Makhadmah et al., "Pyrolysis of poly(vinyl chloride) and—electric arc furnace—dust mixtures," *Journal of Hazardous Materials*, vol. 299, pp. 425–436, 2015.
- [14] M. Jabbari, D. Åkesson, M. Skrifvars, and M. J. Taherzadeh, "Novel lightweight and highly thermally insulative silica aerogel-doped poly(vinyl chloride)-coated fabric composite," *Journal of Reinforced Plastics and Composites*, vol. 34, no. 19, pp. 1581–1592, 2015.
- [15] J. Chen, Z. Liu, J. Jiang, X. Nie, Y. Zhou, and R. E. Murray, "A novel biobased plasticizer of epoxidized cardanol glycidyl ether: synthesis and application in soft poly(vinyl chloride) films," *RSC Advances*, vol. 5, no. 69, pp. 56171–56180, 2015.
- [16] J. Chen, Z. Liu, X. Li, P. Liu, J. Jiang, and X. Nie, "Thermal behavior of epoxidized cardanol diethyl phosphate as novel renewable plasticizer for poly (vinyl chloride)," *Polymer Degradation and Stability*, vol. 126, pp. 58–64, 2016.
- [17] M. Jakić, N. S. Vrandečić, and M. Erceg, "Kinetic analysis of the non-isothermal degradation of poly(vinyl chloride)/poly(ethylene oxide) blends," *Journal of Thermal Analysis and Calorimetry*, vol. 123, no. 2, pp. 1513–1522, 2016.
- [18] S. Qian, H. Wang, E. Zarei, and K. Sheng, "Effect of hydrothermal pretreatment on the properties of moso bamboo particles reinforced polyvinyl chloride composites," *Composites Part B: Engineering*, vol. 82, pp. 23–29, 2015.
- [19] M. Li, J. Zhang, K. Huang, S. Li, J. Jiang, and J. Xia, "Mixed calcium and zinc salts of dicarboxylic acids derived from rosin and dipentene: preparation and thermal stabilization for Pvc," *RSC Advances*, vol. 4, no. 108, pp. 63576–63585, 2014.
- [20] A. P. T. Demir and S. Ulutan, "Degradation kinetics of Pvc plasticized with different plasticizers under isothermal conditions," *Journal of Applied Polymer Science*, vol. 132, no. 10, 2015.
- [21] E. Homer, "Kissinger, reaction kinetics in differential thermal analysis," *Analytical Chemistry*, vol. 29, pp. 1702–1706, 1957.
- [22] T. Ozawa, "Estimation of activation energy by isoconversion methods," *Thermochimica Acta*, vol. 203, pp. 159–165, 1992.
- [23] T. Ozawa, "A new method of analyzing thermogravimetric data," *Bulletin of the Chemical Society of Japan*, vol. 38, no. 11, pp. 1881–1886, 1965.
- [24] A. C. R. Lim, B. L. F. Chin, Z. A. Jawad, and K. L. Hii, "Kinetic analysis of rice husk pyrolysis using Kissinger-Akahira-Sunose (Kas) method," *Procedia engineering*, vol. 148, pp. 1247–1251, 2016.
- [25] H.-m. Xiao, X.-q. Ma, and Z.-y. Lai, "Isoconversional kinetic analysis of co-combustion of sewage sludge with straw and coal," *Applied Energy*, vol. 86, no. 9, pp. 1741–1745, 2009.
- [26] N. Sbirrazzuoli, Y. Girault, and L. Elégant, "Simulations for evaluation of kinetic methods in differential scanning calorimetry. Part 3—peak maximum evolution methods and isoconversional methods," *Thermochimica Acta*, vol. 293, no. 1–2, pp. 25–37, 1997.
- [27] Y. A. El-Shekeil, S. M. Sapuan, M. Jawaid, and O. M. Al-Shuja'a, "Influence of fiber content on mechanical, morphological and thermal properties of kenaf fibers reinforced poly(vinyl

- chloride)/thermoplastic polyurethane poly-blend composites,” *Materials & Design*, vol. 58, pp. 130–135, 2014.
- [28] M. Jakić, N. S. Vrandečić, and I. Klarić, “Thermal degradation of poly(vinyl chloride)/poly(ethylene oxide) blends: thermogravimetric analysis,” *Polymer Degradation and Stability*, vol. 98, no. 9, pp. 1738–1743, 2013.
- [29] B. Zhang, X.-Y. Yan, K. Shibata, T. Uda, M. Tada, and M. Hirasawa, “Thermogravimetric-mass spectrometric analysis of the reactions between oxide (ZnO, Fe₂O₃ or ZnFe₂O₄) and polyvinyl chloride under inert atmosphere,” *Materials Transactions, JIM*, vol. 41, no. 10, pp. 1342–1350, 2000.
- [30] M. Al-harshsheh, S. Kingman, L. Al-Makhadmah, and I. E. Hamilton, “Microwave treatment of electric arc furnace dust with Pvc: dielectric characterization and pyrolysis-leaching,” *Journal of Hazardous Materials*, vol. 274, pp. 87–97, 2014.
- [31] M. Al-Harshsheh, A. Al-Otoom, M. Al-Jarrah, M. Altarawneh, and S. Kingman, “Thermal analysis on the pyrolysis of tetrabromobisphenol A and electric arc furnace dust mixtures,” *Metallurgical and Materials Transactions B*, vol. 49, no. 1, pp. 45–60, 2018.
- [32] M. Al-Harshsheh, S. Kingman, and I. Hamilton, “Microwave treatment of electric arc furnace dust with tetrabromobisphenol A: dielectric characterization and pyrolysis-leaching,” *Journal of Analytical and Applied Pyrolysis*, vol. 128, pp. 168–175, 2017.
- [33] M. Al-Harshsheh, “Thermodynamic analysis on the thermal treatment of electric arc furnace dust-Pvc blends,” *Arabian Journal for Science and Engineering*, vol. 43, no. 11, pp. 5757–5769, 2018.
- [34] M. Al-Harshsheh, M. Aljarrah, A. Al-Otoom, M. Altarawneh, and S. Kingman, “Pyrolysis kinetics of tetrabromobisphenol A (Tbbpa) and electric arc furnace dust mixtures,” *Thermochimica Acta*, vol. 660, pp. 61–69, 2018.
- [35] Z. Ahmad and W. Manzoor, “Thermogravimetric analysis of Zncl₂ catalyzed degradation of Pvc,” *Journal of Thermal Analysis*, vol. 38, no. 10, pp. 2349–2357, 1992.
- [36] A. Ballistreri, S. Foti, G. Montaudo, and E. Scamporrino, “Evolution of aromatic compounds in the thermal decomposition of vinyl polymers,” *Journal of Polymer Science: Polymer Chemistry Edition*, vol. 18, no. 4, pp. 1147–1153, 1980.
- [37] G. Wypych, *Pvc Degradation and Stabilization*, Elsevier, 2015.
- [38] W. H. Starnes and X. Ge, “Mechanism of autocatalysis in the thermal dehydrochlorination of poly (vinyl chloride),” *Macromolecules*, vol. 37, no. 2, pp. 352–359, 2004.
- [39] A. K. Jonscher, “The ‘universal’ dielectric response,” *nature*, vol. 267, no. 5613, pp. 673–679, 1977.
- [40] T. B. Schröder and J. C. Dyre, “Scaling and universality of ac conduction in disordered solids,” *Physical Review Letters*, vol. 84, no. 2, pp. 310–313, 2000.
- [41] Y. Bréchet, J.-Y. Cavaillé, E. Chabert et al., “Polymer based nanocomposites: effect of filler-filler and filler-matrix interactions,” *Advanced Engineering Materials*, vol. 3, no. 8, pp. 571–577, 2001.

Research Article

3D Network Structural Poly (Aryl Ether Ketone)-Polybenzimidazole Polymer for High-Temperature Proton Exchange Membrane Fuel Cells

Junqiao Jiang,¹ Erli Qu,¹ Min Xiao ,¹ Dongmei Han,^{1,2} Shuanjin Wang ,¹ and Yuezhong Meng ¹

¹The Key Laboratory of Low-Carbon Chemistry & Energy Conservation of Guangdong Province, State Key Laboratory of Optoelectronic Materials and Technologies, School of Materials Science and Engineering, Sun Yat-sen University, Guangzhou 510275, China

²School of Chemical Engineering and Technology, Sun Yat-sen University, Zhuhai 519082, China

Correspondence should be addressed to Shuanjin Wang; wangshj@mail.sysu.edu.cn and Yuezhong Meng; mengyzh@mail.sysu.edu.cn

Received 4 June 2020; Revised 20 July 2020; Accepted 29 July 2020; Published 14 August 2020

Academic Editor: Sagar Roy

Copyright © 2020 Junqiao Jiang et al. This is an open access article distributed under the Creative Commons Attribution License, which permits unrestricted use, distribution, and reproduction in any medium, provided the original work is properly cited.

Poor mechanical property is a critical problem for phosphoric acid-doped high-temperature proton exchange membranes (HT-PEMs). In order to address this concern, in this work, a 3D network structural poly (aryl ether ketone)-polybenzimidazole (PAEK-*cr*-PBI) polymer electrolyte membrane was successfully synthesized through crosslinking reaction between poly (aryl ether ketone) with the pendant carboxyl group (PAEK-COOH) and amino-terminated polybenzimidazole (PBI-4NH₂). PAEK-COOH with a poly (aryl ether ketone) backbone endows superior thermal, mechanical, and chemical stability, while PBI-4NH₂ serves as both a proton conductor and a crosslinker with basic imidazole groups to absorb phosphoric acid. Moreover, the composite membrane of PAEK-*cr*-PBI blended with linear PBI (PAEK-*cr*-PBI@PBI) was also prepared. Both membranes with a proper phosphoric acid (PA) uptake exhibit an excellent proton conductivity of around 50 mS cm⁻¹ at 170°C, which is comparable to that of the well-documented PA-doped PBI membrane. Furthermore, the PA-doped PAEK-*cr*-PBI membrane shows superior mechanical properties of 17 MPa compared with common PA-doped PBI. Based upon these encouraging results, the as-synthesized PAEK-*cr*-PBI gives a highly practical promise for its application in high-temperature proton exchange membrane fuel cells (HT-PEMFCs).

1. Introduction

Proton exchange membrane fuel cells (PEMFCs) have drawn much attention as clean power generation devices due to their many attractive features, such as high efficiency, high power density, and environmental friendliness for potential application as power sources in stationary transportation and portable devices [1–5]. Proton exchange membranes (PEMs) are key components of the PEMFCs, which play the main role of proton transport and fuel isolation. Compared with conventional low-temperature PEMFCs, high-temperature PEMFCs (HT-PEMFCs) operate at above

100°C, which made it possess many advantages, such as simple water and heat management, high CO tolerance, and less dependence on platinum catalysts [6–8].

Among all the types of HT-PEMs, phosphoric acid-doped polybenzimidazole (PA-PBI) membranes have been considered to be the most promising candidates for a high-temperature proton exchange membrane owing to its good chemical and thermal stability and excellent proton conductivity under anhydrous conditions at high temperature [9–12]. In order to obtain high proton conductivity, it is necessary to dope an excess amount of phosphoric acid (PA) in the membrane [13]. However, due to the strong plasticization

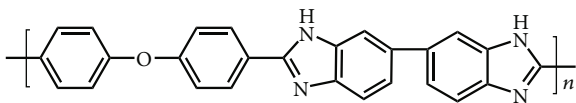


FIGURE 1: The molecular structure of poly (4,4'-(diphenyl ether)-5,5'-bibenzimidazole) (PBI).

of PA molecules, high proton conductivity is usually at the expense of the mechanical strength of the membrane [14–17]. Besides, the preparation of a high-strength PA-PBI membrane requires high molecular weight of PBI, which exhibits poor solubility in organic solvents and makes it fairly hard to prepare uniform casting solution [18]. Therefore, to realize high-performance HT-PEMs and high-efficiency HT-PEMFCs, it is one of the important issues to settle the balance between proton conductivity and mechanical properties of phosphoric acid-doped polymer membranes.

In fact, several strategies have been proposed to deal with the issue. Crosslinking is considered an effective strategy to enhance the properties of PA-doped membranes for HT-PEMFCs [19–23]. In the past few decades, a variety of crosslinkers have been widely studied, including small molecular and macromolecular crosslinkers. Small molecular crosslinkers such as epoxides [24, 25] and halides [26–28] are more frequently used for the improvement of the membrane properties. Compared with small molecular crosslinkers, macromolecular crosslinkers will give higher overall performance to HT-PEMs. Recently, Yang et al. [29] studied the covalently crosslinking PBI membrane using chloromethyl polysulfone as the macromolecular crosslinker. Their results show that the properties of the crosslinked membranes with high PA doping level are almost unchanged during the test. In addition, other macromolecular crosslinkers such as poly (vinyl benzyl chloride) [30] and bromomethylated poly (aryl ether ketone) [31] have also been adopted to prepare crosslinked PBI membranes. Unfortunately, most of these methods are based on the sacrifice of N-H sites on the imidazole ring of the PBI main chain, which ultimately impedes the absorption of phosphoric acid and proton transport [32]. All in all, it is an urgent demand to design a reasonable polymer framework and a suitable covalent crosslinker to satisfy the actual requirements of HT-PEMs. To our knowledge, poly (aryl ether ketone) (PAEK) is extensively used in the preparation of various electrolyte membranes in fuel cells due to its good thermal, mechanical, and chemical stability [33–36].

In this work, we prepared a 3D network structural poly (aryl ether ketone)-PBI (PAEK-*cr*-PBI) through crosslinking reaction between PAEK with the pendant carboxyl group (PAEK-COOH) and amino-terminated imidazole (PBI-4NH₂). For the purpose of enhancing the mechanical strength of a PA-doped membrane without the sacrifice of proton conductivity, a new crosslinker (PBI-4NH₂, polybenzimidazole terminated with amino groups) was designed and synthesized. This kind of crosslinked membrane gets rid of the binding of PBI as a polymer framework. Besides, poly (aryl ether ketone) has good thermal stability to meet the test requirements of HT-PEMFCs, and the 3D network structure of the membrane can maintain good mechanical properties

after phosphoric acid doping. In addition, we also prepared the composite membrane PAEK-*cr*-PBI@PBI, which was obtained by blending PAEK-*cr*-PBI and PBI polymers. In order to better evaluate the performance of the as-synthesized PAEK-*cr*-PBI and PAEK-*cr*-PBI@PBI membranes, we compared the well-documented PBI membrane with it. The properties of these membranes, including their solubility in common solvent, morphology analysis, thermal stability, oxidative stability, proton conductivity, and mechanical strength, were studied and compared.

2. Experiment

2.1. Materials and Chemicals

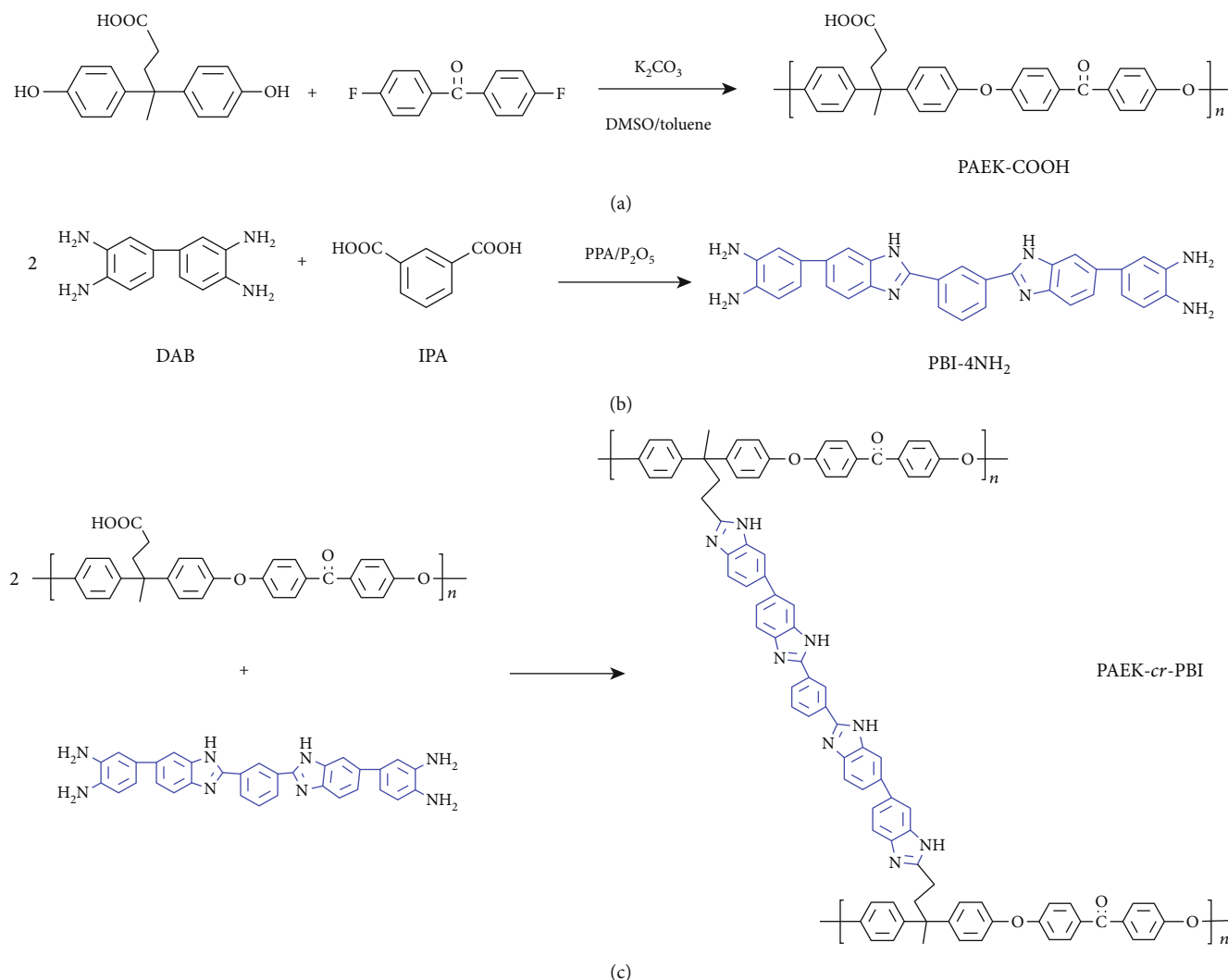
2.1.1. Materials. Poly (4,4'-(diphenyl ether)-5,5'-bibenzimidazole) (PBI, 6000 Pa-S) was obtained from Shanghai Shengjun Plastic Technology Co., Ltd. Figure 1 shows the molecular structure of PBI.

2.1.2. Chemicals. 4,4-Bis(4-hydroxyphenyl)-valeric acid (98%), phosphorus pentoxide (P₂O₅), polyphosphoric acid (PPA), phosphoric acid solution (85 wt%), and 1-methyl-2-pyrrolidinone (NMP) were obtained from Aladdin Chemistry Co. Ltd. 4,4'-Difluorobenzophenone (99%), isophthalic acid (IPA), and 3,3'-diaminobenzidine (DAB, 97%) were obtained from Shanghai Macklin Biochemical Co. Ltd. Potassium carbonate (K₂CO₃), toluene, isopropyl alcohol, tetrahydrofuran (THF), and hydrochloric acid (HCl) were purchased from Guangzhou Chemical Reagent Factory. Ammonia solution (25 wt%) was purchased from Tianjin Fuyu Fine Chemical Co. Ltd.

2.2. Synthesis

2.2.1. Synthesis of PAEK-COOH. Poly (arylene ether ketone) with the pendant carboxyl group (PAEK-COOH) was synthesized via the step condensation polymerization [33, 37, 38]. The synthetic pathway of PAEK-COOH is shown in Scheme 1(a); in a 250 mL three-neck round-bottom flask equipped with a magnetic stirrer, a condenser, a Dean-Stark trap, and a nitrogen inlet, 4,4-bis(4-hydroxyphenyl)-valeric acid (2.86 g, 0.01 mol) and 4,4'-difluorobenzophenone (2.18 g, 0.01 mol) were dissolved in 40 mL DMSO and 45 mL toluene. Then, K₂CO₃ (3.46 g, 0.025 mol) was added to the reaction flask. Under an atmosphere of nitrogen, the mixture was heated to 145°C and maintained at this temperature for 4 h until the water was totally separated by means of a Dean-Stark trap using toluene. Then, the system temperature was elevated to 170°C to render polymerization for 22 h.

Purification of the polymers was done by decantation of the supernatant from the reaction mixture after cooling to room temperature; then, HCl and THF were added at a ratio of 1:4; thus, the mixture was stirred until the solid polymer was completely dissolved. After the stirring, the orange-colored polymer layer floating on the top of the liquid phase was collected. The PAEK-COOH solution in THF (orange-colored polymer layer) was precipitated by dropping it into 500 mL of isopropyl alcohol in a 1 L beaker. The obtained white polymer was washed with isopropyl alcohol, followed



SCHEME 1: Synthesis of (a) PAEK-COOH, (b) PBI-4NH₂, and (c) PAEK-cr-PBI.

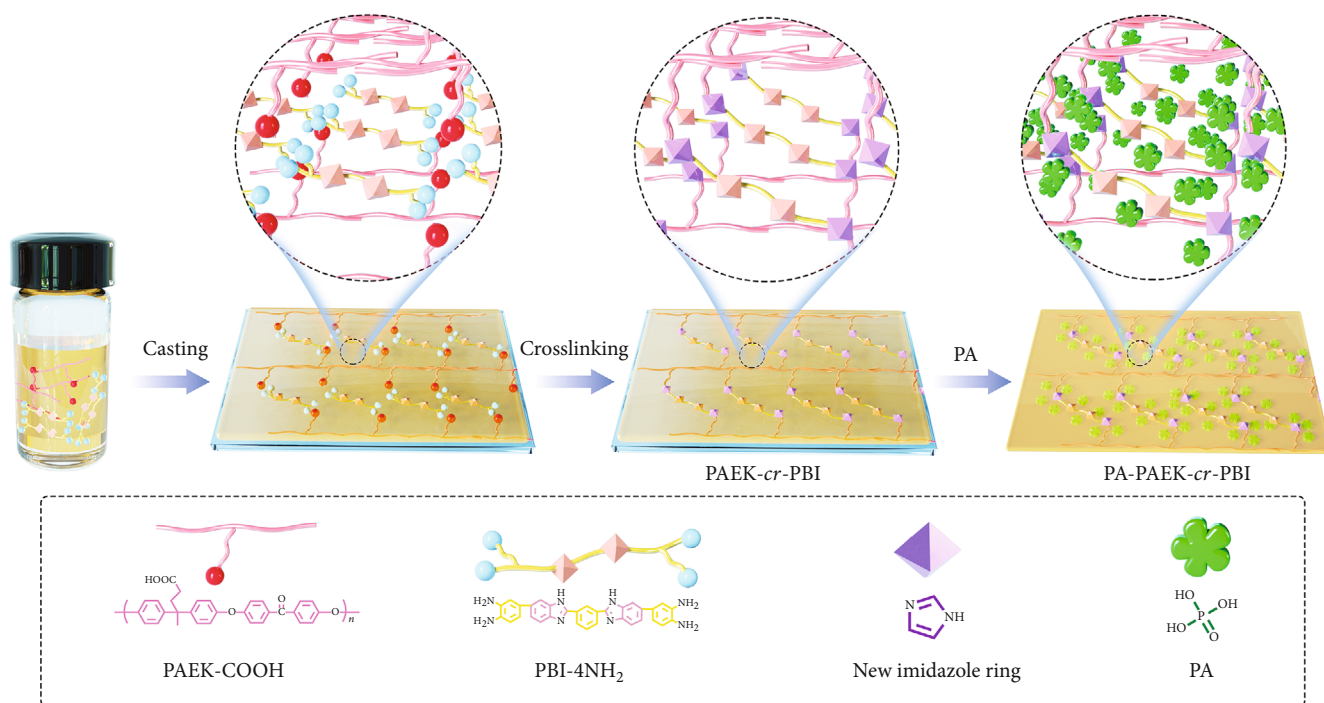
by deionized water. Then, the purified product, PAEK-COOH, was dried in a 100°C dry oven for 24 h.

2.2.2. Synthesis of the Crosslinker (PBI-4NH₂). The amine-terminated polybenzimidazole (PBI-4NH₂) was synthesized by the condensation reaction of 3,3'-diaminobenzidine (DAB) with isophthalic acid (IPA) in polyphosphoric acid (PPA) [39, 40], as shown in Scheme 1(b). In a 100 mL dry three-neck flask equipped with a nitrogen inlet and a nitrogen outlet, 27 g of PPA and 7 g of phosphorus pentoxide were heated at 120°C under nitrogen flow and mechanically stirred about 4 h till a clear solution was observed. After cooling to room temperature, DAB (1.2856 g, 6 mmol) and IPA (0.4985 g, 3 mmol) were added; then, the reaction mixture was mechanically stirred, slowly heated to 190°C, and kept at this temperature for 20 h. After cooling to about 80°C, the viscous solution was slowly poured into the ice deionized water and then was neutralized to pH 7 with dilute solution of ammonium hydroxide solution (5 wt%). The product was filtered and washed with deionized water several times and dried

in a freeze dryer for 2 days at minus 60°C to remove the residual solvents completely.

2.3. Preparation of Membranes

2.3.1. Preparation of the PAEK-cr-PBI Membrane. The synthesis route of PAEK-cr-PBI is shown in Scheme 1(c), and the PAEK-cr-PBI membrane was fabricated by a solution casting method, as shown in Scheme 2. The calculated result of the carboxyl equivalent in PAEK-COOH is 2.15 mmol/g. Firstly, PAEK-COOH (300.0 mg) was dissolved in 2–3 mL 1-methyl-2-pyrrolidinone (NMP) to form a uniformly transparent solution. Then, the PBI-4NH₂ (168.6 mg, the molar ratio of diamino to carboxyl is 1:1) was dissolved completely in 2 mL NMP. The total polymer concentration was controlled to be 8–15% (*w/v*). After that, the solution of PBI-4NH₂ was added dropwise into the solution of PAEK-COOH in NMP and then stirred for 4 h to obtain a uniform solution. The resulting polymer solution was cast onto a clean glass plate followed by heating at 80°C for 5 h to remove residual solvent and then a further thermal treatment at 150°C for 2 h and then put in a



SCHEME 2: Schematic diagram of the preparation procedure of the PA-doped 3D network structural PAEK-*cr*-PBI membrane.

vacuum at 190°C for 12 h for further crosslinking. The obtained membrane was then peeled off, washed thoroughly with deionized water, and dried at 100°C for 24 h.

2.3.2. Preparation of the PAEK-*cr*-PBI@PBI Membrane. Similar to the PAEK-*cr*-PBI membrane, the composite PAEK-*cr*-PBI@PBI membrane was also fabricated by a solution casting method. What needs to be explained here is that the mass ratio between PAEK-*cr*-PBI and PBI is 4 : 1; the detail of the preparation process is as follows: PAEK-COOH (300.0 mg) and PBI (117.2 mg) were dissolved in 3 mL 1-methyl-2-pyrrolidinone (NMP) to form a uniformly transparent solution. Then, the PBI-4NH₂ (168.6 mg) was dissolved completely in the 1-2 mL NMP. The rest of the procedure is the same as the preparation process of the PAEK-*cr*-PBI membrane.

2.3.3. Preparation of the PBI Membrane. The preparation method of the PBI membrane is the most convenient: 0.5 g PBI was dissolved in 5 mL NMP and stirred for 24 h at room temperature to obtain a homogeneous solution. Then, the polymer solution was cast on a flat glass plate and then dried at 80°C for 24 h.

2.4. Characterizations

2.4.1. Structural Characterization. ¹H NMR spectra of the PAEK-COOH and PBI-4NH₂ were recorded on a Bruker DRX-500 NMR spectrometer with deuterated DMSO (DMSO-*d*₆) as the solvent and tetramethylsilane (TMS) as the standard at room temperature. The molecular weight of synthesized PAEK-COOH was measured using a gel permeation chromatography (GPC) system (Waters 515 HPLC Pump, Waters 2414 detector), and the measurement was carried out at 30°C with the THF solvent. The surface and cross-

section morphologies of the membranes were recorded on scanning electron microscopy (FE-SEM, Quanta 400F).

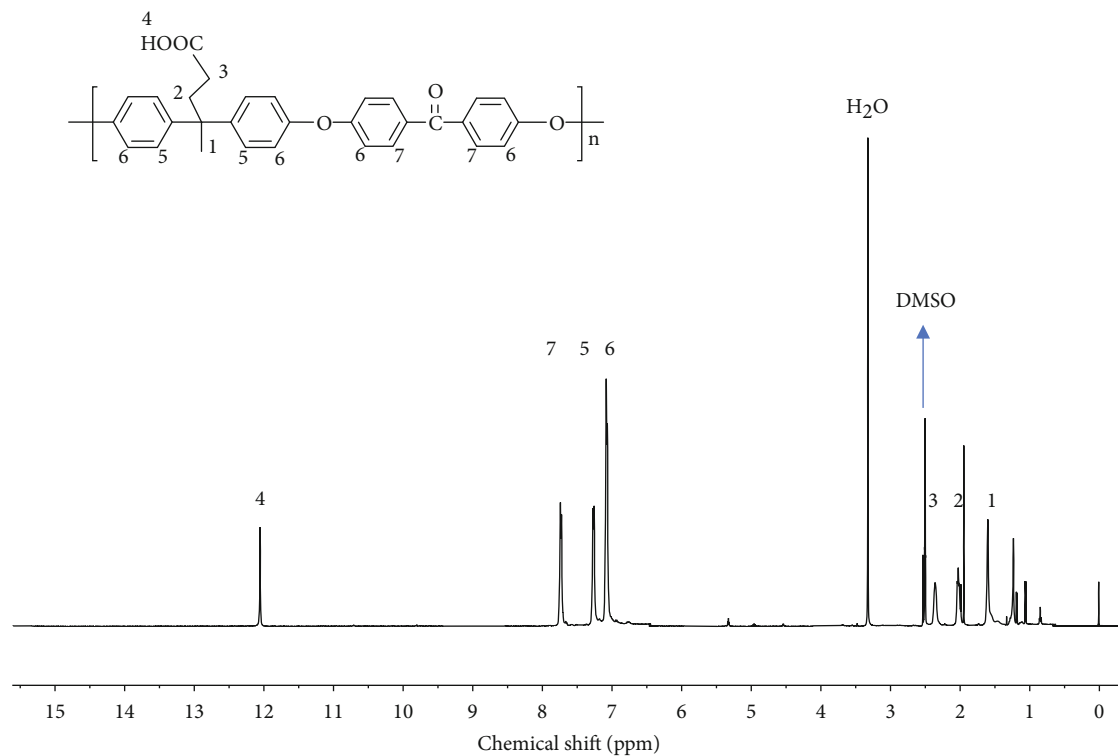
2.4.2. Solubility Test. The crosslinking degree was characterized by measuring the solubility of the PAEK-*cr*-PBI and PAEK-*cr*-PBI@PBI membranes in common solvents. The membranes were immersed in NMP for 12 h at 90°C. Then, the residual samples in the NMP solution were collected, dried, and weighed. The weight residue of the membranes was calculated by the following equation:

$$\text{Gel content(\%)} = \frac{W_A}{W_B} \times 100\%, \quad (1)$$

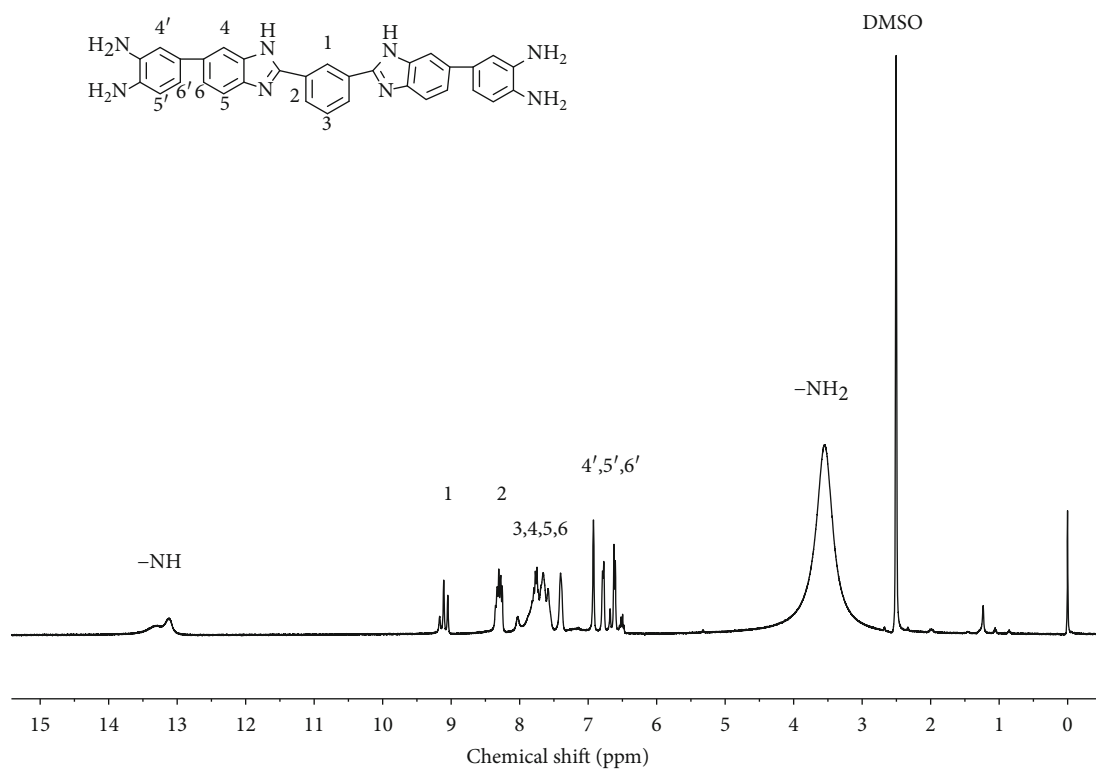
where W_A is the weight of membranes after the test and W_B is the weight of membranes before the test.

2.4.3. PA Uptake and Swellings. The PBI, PAEK-*cr*-PBI, and PAEK-*cr*-PBI@PBI membranes were dried in a vacuum oven at 80°C for 12 h. After measuring the weight, length, width, and thickness, they were immersed in 85 wt% phosphoric acid solution at 120°C for 15 h. The membranes were taken out and wiped with tissue wipes. After drying at 100°C for 12 h, PA uptake and the length, width, and thickness of each sample were measured immediately. Each type of membranes was tested for three samples, and the average value was reported. The PA uptake ratio of the membrane was calculated by the following equation:

$$\text{PA uptake(\%)} = \frac{W_{PA} - W_D}{W_D} \times 100\%, \quad (2)$$



(a)



(b)

FIGURE 2: ¹H NMR spectra of (a) PAEK-COOH and (b) PBI-4NH₂.

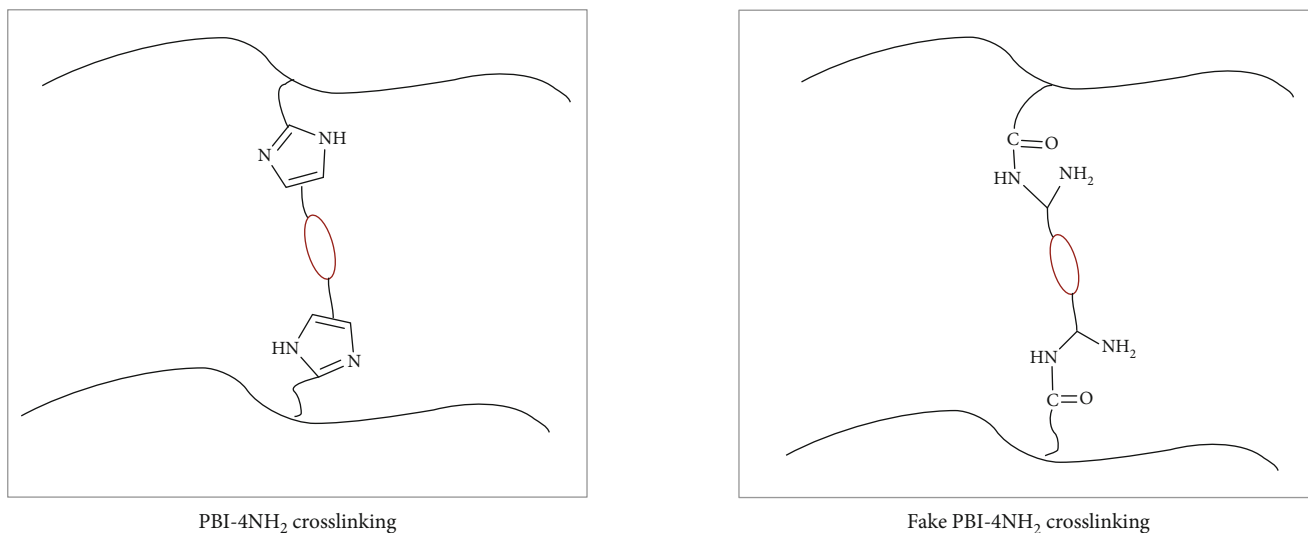


FIGURE 3: Schematic representation of the possible crosslinking structures of the PAEK-*cr*-PBI membrane.

where W_{PA} is the weight of the PA-doped membrane and W_D is the weight of the undoped dry membrane. The dimensional swelling ratio of the membrane was calculated by the following equations:

$$S_{\text{area}} (\%) = \frac{A_{PA} - A_D}{A_D} \times 100\%, \quad (3)$$

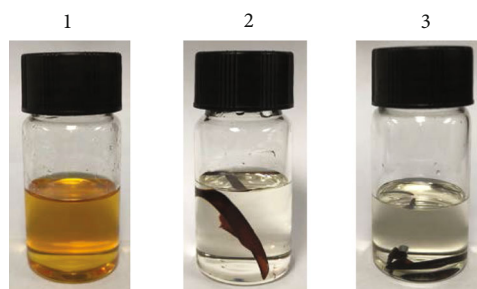
$$S_{\text{volume}} (\%) = \frac{V_{PA} - V_D}{V_D} \times 100\%,$$

where A_D and V_D represent the area and volume of the dry membrane, respectively, and A_{PA} and V_{PA} represent the area and volume of the wet membrane, respectively, after being immersed in 85 wt% phosphoric acid solution at 120°C.

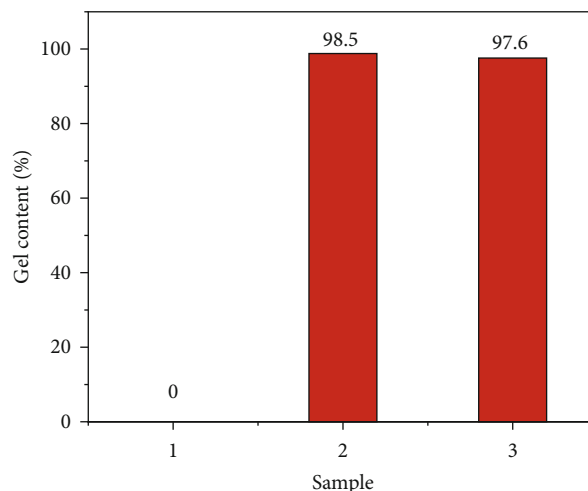
2.4.4. Thermal Stability. The thermogravimetric (TGA) curves of membranes were obtained by Pyris 1 TGA (PerkinElmer) under the nitrogen atmosphere. All the samples were pre-heated at 100°C for 2 h to eliminate the absorbed water and organic solvents before testing. Then, the samples were tested from 50 to 800°C with a heating rate of 10°C min⁻¹.

2.4.5. Oxidative Stability. To test oxidative stability, the undoped membrane samples were immersed into Fenton's reagent (3% H₂O₂ solution containing 4 ppm Fe²⁺) at 80°C for 40 h; then, the samples were removed from the solution and dried in a vacuum oven at 120°C for 12 h. Each type of membranes was tested for 3 samples, and the average value was reported. The residual weight of the samples represented the oxidative stability [18, 41].

2.4.6. Proton Conductivity. The proton conductivities of PBI, PAEK-*cr*-PBI, and PAEK-*cr*-PBI@PBI membranes were measured by electrochemical impedance spectroscopy (EIS) using a PGSTAT204 electrochemical workstation (AUT50992, AUTOLAB). The membrane sample was immersed in 85 wt% PA solution for 12 h at room temperature before testing. The impedance measurement was performed under anhy-



(a)



(b)

FIGURE 4: (a) Photographs and (b) gel content of membranes after the solubility test in NMP at 90°C for 12 h. (1) PBI, (2) PAEK-*cr*-PBI, and (3) PAEK-*cr*-PBI@PBI.

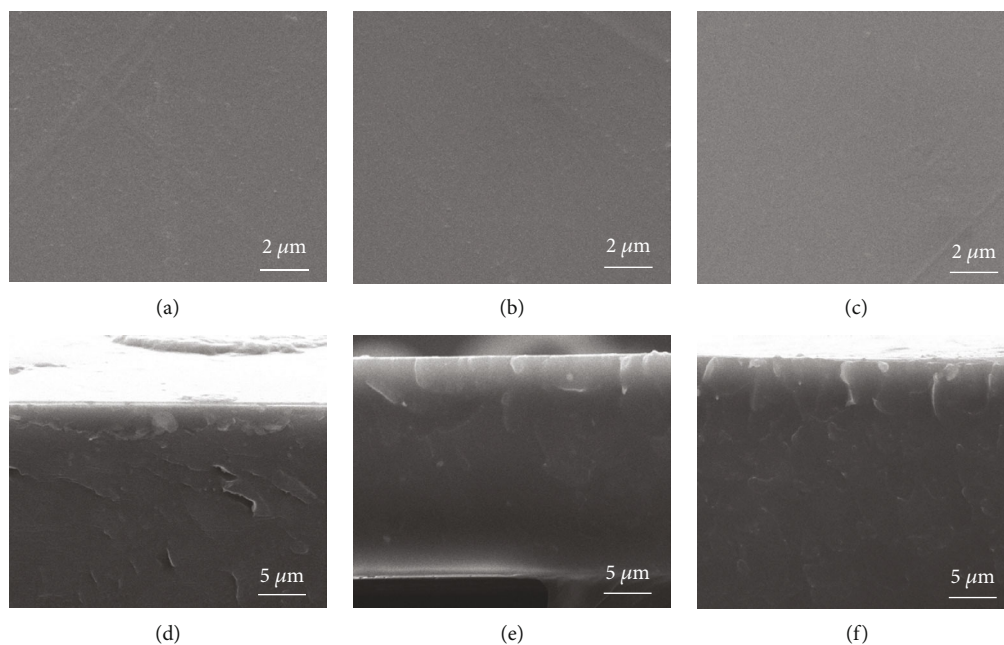


FIGURE 5: SEM micrographs of the surface (up) and cross-section (down) of PA-undoped membranes: (a, d) PBI, (b, e) PAEK-*cr*-PBI, and (c, f) PAEK-*cr*-PBI@PBI.

drous conditions from 120°C to 170°C in the frequency range of 0.1 Hz to 100 kHz. The conductivity is calculated by the following equation:

$$\sigma = \frac{L}{R \times W \times T}, \quad (4)$$

where L (cm) is the distance between two electrodes, R (Ω) is the membrane resistance obtained by a Nyquist plot, and W (cm) and T (cm) are the width and thickness of the membrane, respectively.

2.4.7. Mechanical Properties. The mechanical properties of PA-doped membranes were evaluated on a tensile tester (New SANS, Shenzhen, China) with a stretching speed of 10 mm/min under an ambient atmosphere. The size of all the samples is 6 mm \times 40 mm. Before testing, the PA-doped membranes were dried in a vacuum oven at 100°C for 24 h to remove any absorbed water or organic solvents. Each type of membranes was tested for 4 samples, and the average value was reported.

3. Results and Discussion

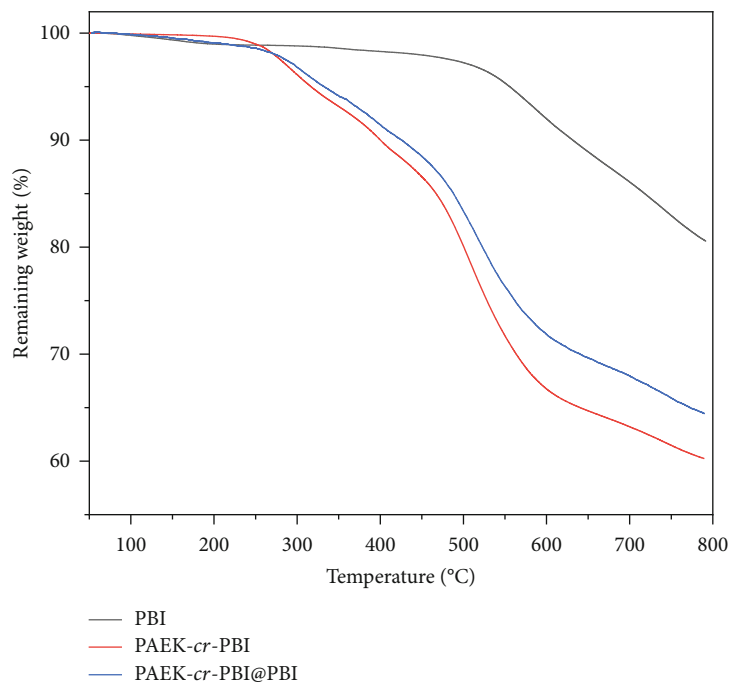
3.1. Chemical Structure Identification. From the GPC analysis, the number and weight average molecular weights of PAEK-COOH were 40,000 and 92,000 g mol⁻¹, respectively. This result suggests that the polymer possesses a high enough molecular weight to form a membrane.

The synthesized PAEK-COOH and PBI-4NH₂ were analyzed using ¹H NMR (500 MHz, DMSO-d₆), and the presence of carboxyl and amino groups was confirmed as shown in Figure 1. As it can be seen in Figure 2(a), the protons in the benzene ring of the polymer main chain show chemical shifts

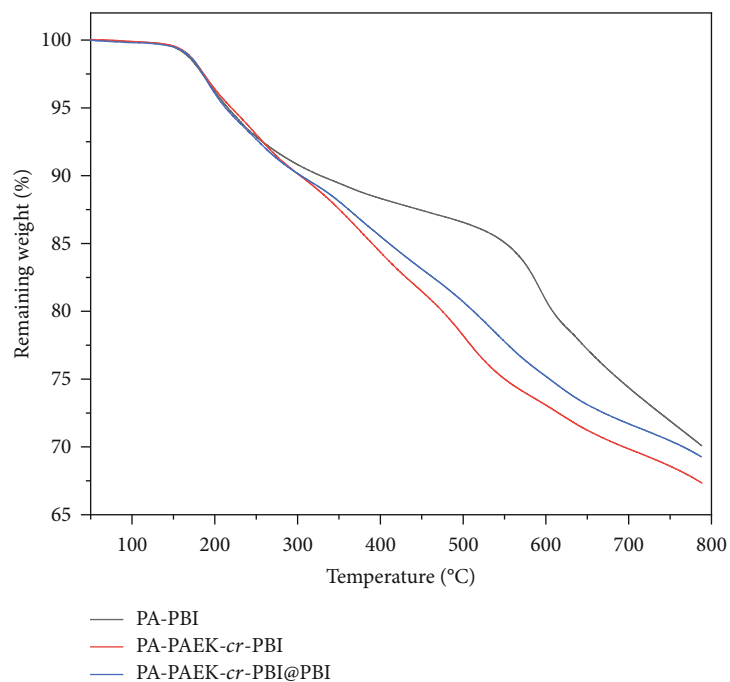
at 7.06, 7.27, and 7.73 ppm; the NMR peak at 12.05 ppm comes from the proton in the carboxyl group of PAEK-COOH. In Figure 2(b), the broad peak at 13.10 ppm is attributed to the -NH proton of the benzimidazole groups. Peaks of 9.05-9.16 ppm are assigned to protons (H1) near the two benzimidazole groups. Peaks in the range of 6.93-6.50 ppm are ascribed to aromatic protons of benzene rings (H3', H4', and H5') at both ends. Peaks in the range of 8.28-7.41 are attributed to the remaining aromatic protons (H2-6). The broad peak at 3.55 ppm is attributed to protons of the terminal amino group. The results of peak distribution indicate that the desired PBI-4NH₂ was prepared successfully.

The schematic representation of the possible crosslinking structures of the crosslinked membrane is shown in Figure 3. Because of the insolubility of the crosslinked membrane (PAEK-*cr*-PBI), it is difficult to confirm the imidazolization between PAEK-COOH and PBI-4NH₂ by the conventional analysis.

The solubility test was carried out to ascertain the crosslinking degree of PAEK-*cr*-PBI and PAEK-*cr*-PBI@PBI successfully. It is easy to know that if a complete dissolution of the membrane occurs, there is no crosslinking in the membrane. On the other hand, if the membrane has a residual sample after a period of immersing, the membrane is approved to be crosslinked. As shown in Figure 4, PAEK-*cr*-PBI and PAEK-*cr*-PBI@PBI membrane samples maintained the structural integrity after immersing in NMP at 90°C for 12 h. The weight of the PAEK-*cr*-PBI and PAEK-*cr*-PBI@PBI sample was over 97% after treatment. These results confirm that the crosslinking occurred between PAEK-COOH and PBI-4NH₂. In addition, there was no significant dissolution of PBI in the PAEK-*cr*-PBI@PBI membrane, which may be owing to the network structure of PAEK-*cr*-PBI suppressing PBI molecular



(a)



(b)

FIGURE 6: TGA curves of (a) PA-undoped and (b) PA-doped membranes under the N_2 atmosphere.

chain movement. On the contrary, the noncrosslinked membranes (PBI) completely dissolved in NMP in 2 h.

3.2. Morphology Analysis. The surface and cross-section morphologies of the prepared membranes were studied using SEM micrography. In Figure 5, it is observed that PAEK-cr-PBI and PAEK-cr-PBI@PBI membranes show a completely homogenous and compact structure without pores as well as the PBI membrane, which is essential for separating the

fuel and oxidant during fuel cell operation and benefits the fuel cell performance.

3.3. Thermal Stability. Thermal stability of polymer electrolytes is one of the most critical features for long-term durability of fuel cells, especially in high-temperature operation. The thermal stability of PA-undoped and PA-doped membranes was studied by TGA under the nitrogen atmosphere. As shown in Figure 6(a), two-step degradation can be observed

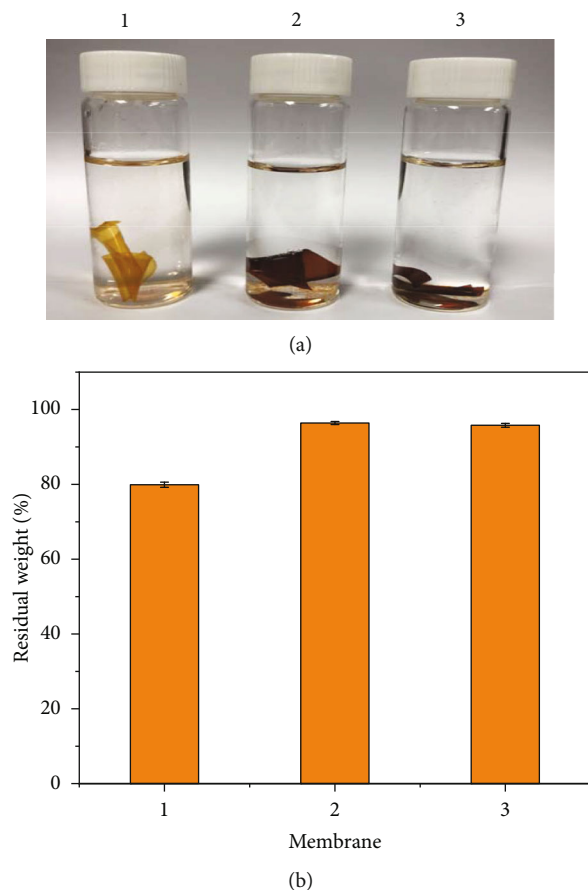


FIGURE 7: (a) Photographs and (b) residual weight of the membranes after the Fenton test: (1) PBI, (2) PAEK-cr-PBI, and (3) PAEK-cr-PBI@PBI.

in both undoped PAEK-cr-PBI and PAEK-cr-PBI@PBI membrane samples. The first weight loss beginning at around 250°C was attributed to the degradation of imidazole groups and carboxyl groups on the side chains, which suggested that the amino and carboxyl groups do not react completely. The second step observed at about 470°C was due to the degradation of the polymer main chain, including poly (aryl ether ketone) (PAEK) and poly (4,4'-(diphenyl ether)-5,5'-bibenzimidazole) (PBI). On the other hand, the undoped PBI membrane decomposed only in one step at around 500°C. After doping with PA, as shown in Figure 6(b), for all the membranes, weight loss appeared earlier at about 160°C because of the dehydration of phosphoric acid. Nonetheless, the degradation of polymer membranes itself was observed in the temperature range similar to that of PA-undoped polymer membranes. The TGA results show that both PAEK-cr-PBI and PAEK-cr-PBI@PBI membranes exhibit excellent thermal stabilities and can be used for HT-PEMFCs.

3.4. Oxidative Stability. To estimate the long-term stability of PEMs, the oxidative stability of the membranes was measured by the Fenton test. During the fuel cell operation, the incom-

TABLE 1: PA doping behavior of the membranes.

Membrane	PA uptake (%)	S_{area} (%)	S_{volume} (%)
PBI	231 ± 8	50 ± 2	136 ± 7
PAEK-cr-PBI	193 ± 5	37 ± 2	79 ± 4
PAEK-cr-PBI@PBI	224 ± 6	43 ± 2	124 ± 5

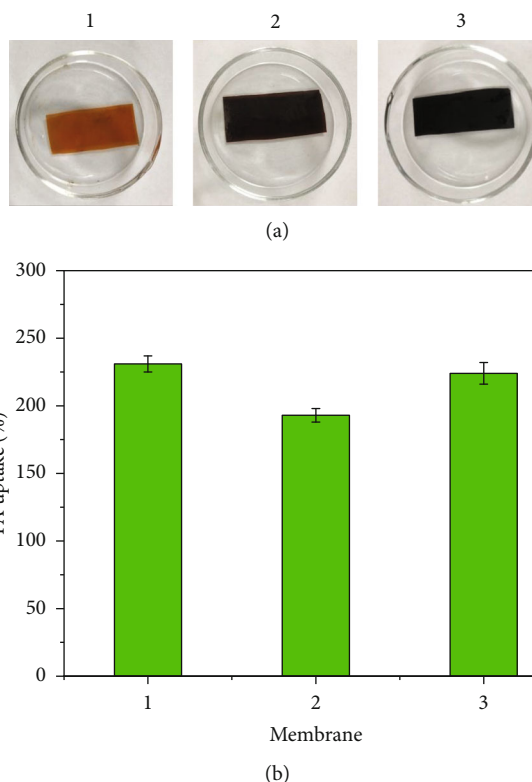


FIGURE 8: (a) Photographs of the PA-doped membrane and (b) PA uptake of the membranes: (1) PBI, (2) PAEK-cr-PBI, and (3) PAEK-cr-PBI@PBI.

plete reduction of oxygen produces HO^\bullet and HO_2^\bullet radicals. Subsequently, these lively radicals attack the skeleton of the polymer membrane, which causes membrane degradation. The degradation of the membranes was investigated by determining the weight loss. As shown in Figure 7, the PAEK-cr-PBI and PAEK-cr-PBI@PBI membranes show superior oxidative stabilities as compared to the PBI membrane. It is because the densely crosslinked structure reduces the possibility of radical species to attack the polymer chain. After 40 h of the Fenton test, only 79.9% of the initial weight of the linear PBI membrane remained. However, the residual weight values of PAEK-cr-PBI and PAEK-cr-PBI@PBI are both more than 95%. The results indicated that the polymer PAEK-cr-PBI exhibited excellent oxidative stability.

3.5. PA Uptakes and Swellings. The proton transport of HT-PEMs depends on the dissociation of phosphoric acid, so the content of free phosphoric acid has a direct impact on proton conductivity of HT-PEM materials. The PA-doped membranes were obtained by immersing the dried membranes into 85 wt% phosphoric acid solution at 120°C for 15 h, and the PA

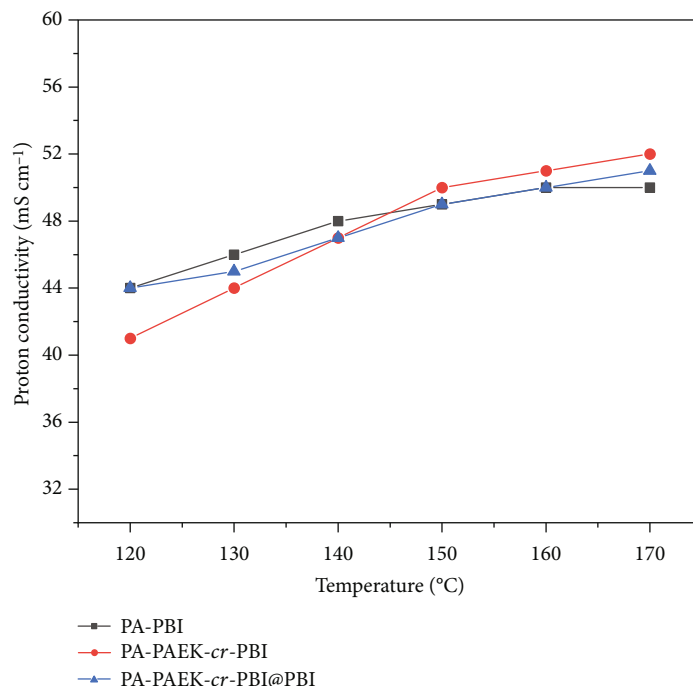


FIGURE 9: Proton conductivity of PA-doped membranes.

uptake and swelling ratio of the membrane are summarized in Table 1. To make it easier to follow, the photographs of the PA-doped membranes and histogram of PA uptake of the PBI, PAEK-*cr*-PBI, and PAEK-*cr*-PBI@PBI membranes are shown in Figure 8.

As it can be seen in Figure 8, the highest PA uptake was obtained by the PBI membrane. However, the PA uptakes of the membranes synthesized in this study are not disappointing. As it can be seen in Table 1, the PAEK-*cr*-PBI and PAEK-*cr*-PBI@PBI membranes have a PA uptake of 193% and 224%, respectively. Obviously, the PAEK-*cr*-PBI@PBI membrane, which is the membrane PAEK-*cr*-PBI blended with some PBI, did absorb more phosphoric acid than the PAEK-*cr*-PBI membrane without PBI.

In respect to the swelling of the membrane caused by doping PA molecules, the PAEK-*cr*-PBI membrane showed a volume swelling of below 80% and an area swelling of below 40%. The low swelling of the PA-doped PAEK-*cr*-PBI membrane probably benefited from its crosslinked structure and the skeleton stability of the poly (aryl ether ketone) matrix. However, the swelling of the membrane with PBI (PAEK-*cr*-PBI@PBI) was higher than that of the pristine PAEK-*cr*-PBI membrane. That may be due to the enhancement of PA uptake of the membrane or the plasticizing effect of phosphoric acid on the PAEK-*cr*-PBI framework.

3.6. Proton Conductivities. The proton conductivity measurement was carried out from 120 to 170°C in anhydrous condition. In order to evaluate the proton conductivity of crosslinked PAEK-*cr*-PBI and PAEK-*cr*-PBI@PBI membranes, the well-documented PBI membrane was selected as the comparison. In Figure 9, the proton conductivities of all the membranes increase with the increase in the testing temperature as we expected. It is interesting to see that these

three kinds of membranes have almost the same proton conduction ability, which demonstrates that the proton conductivity of the PAEK-*cr*-PBI and PAEK-*cr*-PBI@PBI membranes is comparable to that of the traditional PBI membrane. However, there is a change observed in the slope above 150°C for the proton conductivity curves of all membranes, which may be due to the transformation of a proton conducting mechanism, because the condensed phosphoric acids such as the dimer (pyrophosphoric acid ($H_4P_2O_7$)), trimer (meta- or tripolyphosphoric acid ($H_5P_3O_{10}$)), and larger fused structures were formed when the temperature is over 150°C [1]. Obviously, when the temperature is over 150°C, the PAEK-*cr*-PBI membrane with the lowest PA uptake exhibits the highest proton conductivity, which illustrates that the 3D network structure of the membrane is conducive to proton conduction.

3.7. Mechanical Properties. It is well known that the excellent mechanical properties of HT-PEMs are essential for practical application. The typical stress-strain curves of the membranes at room temperature are shown in Figure 10, and the mechanical properties are displayed in Table 2. As shown in Figure 10, the PA-doped PAEK-*cr*-PBI membrane exhibits the best tensile strength of 17 MPa among the three kinds of membranes as expected. In the meanwhile, the PA-doped PAEK-*cr*-PBI@PBI membrane also showed fairly excellent mechanical strength of over 10 MPa. However, the tensile strength of the PA-doped PBI membrane is only about 3.5 MPa. These results show that the PA-doped 3D network structural PAEK-*cr*-PBI membrane has outstanding mechanical properties; moreover, it can be used as a support material to improve the mechanical properties of PA-doped PBI membrane without reducing the proton conductivity.

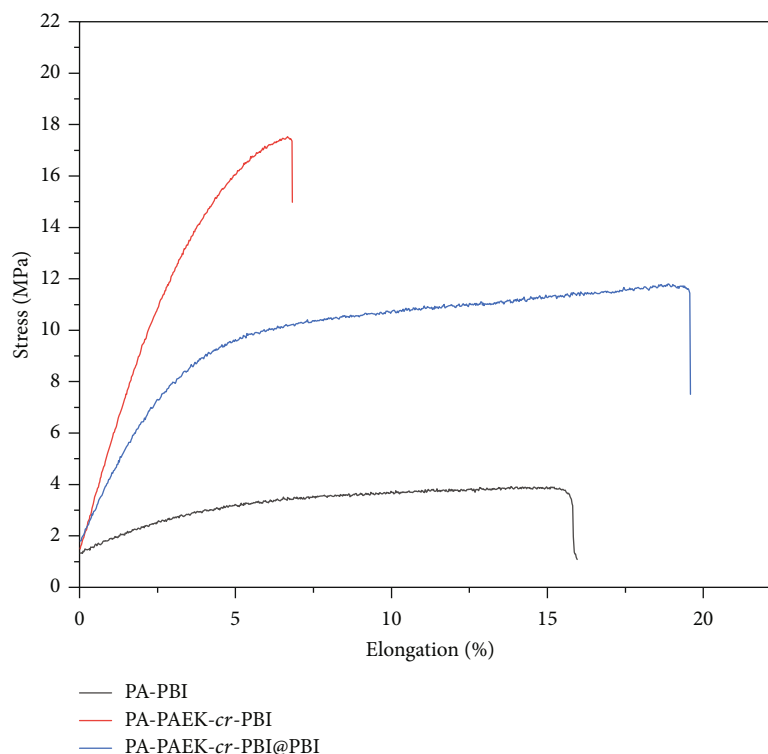


FIGURE 10: Mechanical properties of PA-doped membranes at room temperature.

TABLE 2: Summary of proton conductivities and mechanical properties of PA-doped membranes.

Membrane	PA uptake (%)	Proton conductivity (mS cm^{-1}) ^a	Tensile strength (MPa) ^b	Elongation (%) ^b
PBI	231 ± 8	50	3.5 ± 0.4	15.8 ± 2.4
PAEK- <i>cr</i> -PBI	193 ± 5	52	17.0 ± 0.4	9.7 ± 1.1
PAEK- <i>cr</i> -PBI@PBI	224 ± 6	51	11.4 ± 0.3	19.7 ± 3.2

^aMeasured at 170°C and under anhydrous condition. ^bMeasured at room temperature.

4. Conclusions

In this work, a 3D network structural PAEK-*cr*-PBI membrane was prepared and investigated as HT-PEMs for HT-PEMFCs. The 3D network structural membrane PAEK-*cr*-PBI and the composite membrane PAEK-*cr*-PBI@PBI both showed excellent thermal stability which is suitable for operation in the high-temperature range of $120\sim 180^\circ\text{C}$. Moreover, the PAEK-*cr*-PBI and PAEK-*cr*-PBI@PBI membranes exhibit excellent proton conductivities of about 50 mS cm^{-1} at 170°C , which are comparable to those of the traditional PBI membrane. As an encouraging result, the PA-doped PAEK-*cr*-PBI membrane showed superior mechanical properties of 17 MPa than the PA-doped linear PBI membrane, which is only 3.5 MPa . These results show that the as-synthesized PAEK-*cr*-PBI gives a highly practical promise for its application in HT-PEMFCs.

Data Availability

All of the data used to support the findings of this study are included within the article.

Conflicts of Interest

There is no conflict of interest.

Acknowledgments

This work was supported by the National Key Research and Development Program (2018YFA0702002), the Link Project of the National Natural Science Foundation of China and Guangdong Province (Grant No. U1601211), the National Key Research and Development Program (Japan-China Joint Research Program) (2017YFE9127900), the National Natural Science Foundation of China (51573215, 21506260, 21706294, and 21376276), the Natural Science Foundation of Guangdong Province (2016A030313354), Guangdong Science and Technology Department (Grant Nos. 2016A050503001, 2016B010114004, and 2017B090901003), the Guangzhou Science and Technology Plan Project (Grant Nos. 201804020025 and 201707010424), and the Fundamental Research Funds for the Central Universities (Grant Nos. 17lgjc37, 18lgpy32, and 19lgpy07).

References

- [1] W. Ma, C. Zhao, J. Yang et al., "Cross-linked aromatic cationic polymer electrolytes with enhanced stability for high temperature fuel cell applications," *Energy & Environmental Science*, vol. 5, no. 6, pp. 7617–7625, 2012.
- [2] J. Yang, Q. Li, L. N. Cleemann et al., "Crosslinked hexafluoropropylidene polybenzimidazole membranes with chloromethyl polysulfone for fuel cell applications," *Advanced Energy Materials*, vol. 3, no. 5, pp. 622–630, 2013.
- [3] S. Wang, C. Zhao, W. Ma et al., "Silane-cross-linked polybenzimidazole with improved conductivity for high temperature proton exchange membrane fuel cells," *Journal of Materials Chemistry A*, vol. 1, no. 3, pp. 621–629, 2013.
- [4] Z. Guo, X. Xu, Y. Xiang, S. Lu, and S. P. Jiang, "New anhydrous proton exchange membranes for high-temperature fuel cells based on PVDF–PVP blended polymers," *Journal of Materials Chemistry A*, vol. 3, no. 1, pp. 148–155, 2015.
- [5] K. J. Kallitsis, R. Nannou, A. K. Andreopoulou et al., "Cross-linked wholly aromatic polyether membranes based on quinoline derivatives and their application in high temperature polymer electrolyte membrane fuel cells," *Journal of Power Sources*, vol. 379, pp. 144–154, 2018.
- [6] S. S. Araya, F. Zhou, V. Liso et al., "A comprehensive review of PBI-based high temperature PEM fuel cells," *International Journal of Hydrogen Energy*, vol. 41, no. 46, pp. 21310–21344, 2016.
- [7] A. Chandan, M. Hattenberger, A. el-kharouf et al., "High temperature (HT) polymer electrolyte membrane fuel cells (PEMFC) - A review," *Journal of Power Sources*, vol. 231, pp. 264–278, 2013.
- [8] F. Liu, S. Wang, H. Chen et al., "Cross-linkable polymeric ionic liquid improve phosphoric acid retention and long-term conductivity stability in polybenzimidazole based PEMs," *ACS Sustainable Chemistry & Engineering*, vol. 6, no. 12, pp. 16352–16362, 2018.
- [9] J. Fang, X. Lin, D. Cai, N. He, and J. Zhao, "Preparation and characterization of novel pyridine-containing polybenzimidazole membrane for high temperature proton exchange membrane fuel cells," *Journal of Membrane Science*, vol. 502, pp. 29–36, 2016.
- [10] J. A. Asensio, E. M. Sánchez, and P. Gómez-Romero, "Proton-conducting membranes based on benzimidazole polymers for high-temperature PEM fuel cells. A chemical quest," *Chemical Society Reviews*, vol. 39, no. 8, pp. 3210–3239, 2010.
- [11] F. J. Pinar, P. Cañizares, M. A. Rodrigo, D. Úbeda, and J. Lobato, "Long-term testing of a high-temperature proton exchange membrane fuel cell short stack operated with improved polybenzimidazole-based composite membranes," *Journal of Power Sources*, vol. 274, pp. 177–185, 2015.
- [12] S. Gao, H. Xu, T. Luo et al., "Novel proton conducting membranes based on cross-linked sulfonated polyphosphazenes and poly(ether ether ketone)," *Journal of Membrane Science*, vol. 536, pp. 1–10, 2017.
- [13] L. Vilčiauskas, M. E. Tuckerman, G. Bester, S. J. Paddison, and K. D. Kreuer, "The mechanism of proton conduction in phosphoric acid," *Nature Chemistry*, vol. 4, no. 6, pp. 461–466, 2012.
- [14] J. Kerres and V. Atanasov, "Cross-linked PBI-based high-temperature membranes: stability, conductivity and fuel cell performance," *International Journal of Hydrogen Energy*, vol. 40, no. 42, pp. 14723–14735, 2015.
- [15] Y. Cai, Z. Yue, X. Teng, and S. Xu, "Phosphoric acid doped crosslinked polybenzimidazole/modified graphene oxide composite membranes for high temperature proton exchange membrane applications," *Journal of The Electrochemical Society*, vol. 165, no. 11, pp. F914–F920, 2018.
- [16] Y. Cai, Z. Yue, X. Teng, and S. Xu, "Radiation grafting graphene oxide reinforced polybenzimidazole membrane with a sandwich structure for high temperature proton exchange membrane fuel cells in anhydrous atmosphere," *European Polymer Journal*, vol. 103, pp. 207–213, 2018.
- [17] Y. Cai, Z. Yue, Q. Jiang, and S. Xu, "Modified silicon carbide whisker reinforced polybenzimidazole used for high temperature proton exchange membrane," *Journal of Energy Chemistry*, vol. 27, no. 3, pp. 820–825, 2018.
- [18] J. Jiang, X. Zhu, H. Qian et al., "Cross-linked sulfonated poly(ether ether ketone) electrolytes bearing pendent imidazole groups for high temperature proton exchange membrane fuel cells," *Sustainable Energy & Fuels*, vol. 3, no. 9, pp. 2426–2434, 2019.
- [19] D. Joseph, N. N. Krishnan, D. Henkensmeier et al., "Thermal crosslinking of PBI/sulfonated polysulfone based blend membranes," *Journal of Materials Chemistry A*, vol. 5, no. 1, pp. 409–417, 2017.
- [20] C.-H. Shen and S. L.-C. Hsu, "Synthesis of novel cross-linked polybenzimidazole membranes for high temperature proton exchange membrane fuel cells," *Journal of Membrane Science*, vol. 443, pp. 138–143, 2013.
- [21] Z. Yue, Y.-B. Cai, and S. Xu, "Phosphoric acid-doped organic-inorganic cross-linked sulfonated poly(imide-benzimidazole) for high temperature proton exchange membrane fuel cells," *International Journal of Hydrogen Energy*, vol. 41, no. 24, pp. 10421–10429, 2016.
- [22] Z. Yue, Y.-B. Cai, and S. Xu, "Phosphoric acid-doped cross-linked sulfonated poly(imide-benzimidazole) for proton exchange membrane fuel cell applications," *Journal of Membrane Science*, vol. 501, pp. 220–227, 2016.
- [23] Z. Yue, Y.-B. Cai, and S. Xu, "Proton conducting sulfonated poly(imide-benzimidazole) with tunable density of covalent/ionic cross-linking for fuel cell membranes," *Journal of Power Sources*, vol. 286, pp. 571–579, 2015.
- [24] J. Yang, Y. Xu, P. Liu, L. Gao, Q. Che, and R. He, "Epoxides cross-linked hexafluoropropylidene polybenzimidazole membranes for application as high temperature proton exchange membranes," *Electrochimica Acta*, vol. 160, pp. 281–287, 2015.
- [25] H.-L. Lin, Y.-C. Chou, T. L. Yu, and S. W. Lai, "Poly(benzimidazole)-epoxide crosslink membranes for high temperature proton exchange membrane fuel cells," *International Journal of Hydrogen Energy*, vol. 37, no. 1, pp. 383–392, 2012.
- [26] C.-H. Shen, L. C. Jheng, S. L. C. Hsu, and J. Tse-Wei Wang, "Phosphoric acid-doped cross-linked porous polybenzimidazole membranes for proton exchange membrane fuel cells," *Journal of Materials Chemistry*, vol. 21, no. 39, pp. 15660–15665, 2011.
- [27] Q. Li, C. Pan, J. O. Jensen, P. Noyé, and N. J. Bjerrum, "Cross-linked polybenzimidazole membranes for fuel cells," *Chemistry of Materials*, vol. 19, no. 3, pp. 350–352, 2007.
- [28] M. Han, G. Zhang, Z. Liu et al., "Cross-linked polybenzimidazole with enhanced stability for high temperature proton exchange membrane fuel cells," *Journal of Materials Chemistry*, vol. 21, no. 7, pp. 2187–2193, 2011.

- [29] J. Yang, D. Aili, Q. Li et al., "Covalently cross-linked sulfone polybenzimidazole membranes with poly (vinylbenzyl chloride) for fuel cell applications," *Chem Sus Chem*, vol. 6, no. 2, pp. 275–282, 2013.
- [30] S. Wang, C. Zhao, W. Ma et al., "Macromolecular cross-linked polybenzimidazole based on bromomethylated poly (aryl ether ketone) with enhanced stability for high temperature fuel cell applications," *Journal of Power Sources*, vol. 243, pp. 102–109, 2013.
- [31] L. Wang, Z. Liu, Y. Liu, and L. Wang, "Crosslinked polybenzimidazole containing branching structure with no sacrifice of effective N-H sites: towards high-performance high-temperature proton exchange membranes for fuel cells," *Journal of Membrane Science*, vol. 583, pp. 110–117, 2019.
- [32] C. M. Tuan and D. Kim, "Anion-exchange membranes based on poly(arylene ether ketone) with pendant quaternary ammonium groups for alkaline fuel cell application," *Journal of Membrane Science*, vol. 511, pp. 143–150, 2016.
- [33] D. D. Tham and D. Kim, "C2 and N3 substituted imidazolium functionalized poly(arylene ether ketone) anion exchange membrane for water electrolysis with improved chemical stability," *Journal of Membrane Science*, vol. 581, pp. 139–149, 2019.
- [34] G. Li, C. Zhao, C. Zhu et al., "Side-chain-type quaternized naphthalene-based poly (arylene ether ketone) s for anhydrous high temperature proton exchange membranes," *RSC Advances*, vol. 6, no. 101, pp. 98854–98860, 2016.
- [35] L. Lin, Z. Chen, Z. Zhang et al., "New comb-shaped ionomers based on hydrophobic poly(aryl ether ketone) backbone bearing hydrophilic high concentration sulfonated micro-cluster," *Polymer*, vol. 96, pp. 188–197, 2016.
- [36] D. Liu, Y. Xie, S. Li et al., "High dimensional stability and alcohol resistance aromatic poly (aryl ether ketone) polyelectrolyte membrane synthesis and characterization," *ACS Applied Energy Materials*, vol. 2, no. 3, pp. 1646–1656, 2019.
- [37] N. Lee, D. T. Duong, and D. Kim, "Cyclic ammonium grafted poly (arylene ether ketone) hydroxide ion exchange membranes for alkaline water electrolysis with high chemical stability and cell efficiency," *Electrochimica Acta*, vol. 271, pp. 150–157, 2018.
- [38] S. Zhu, Z. Chen, B. Han, G. Wang, Z. Jiang, and S. Zhang, "Novel nanocellular poly (aryl ether ketone) foams fabricated by controlling the crosslinking degree," *RSC Advances*, vol. 5, no. 64, pp. 51966–51974, 2015.
- [39] S. Maity and T. Jana, "Polybenzimidazole block copolymers for fuel cell: synthesis and studies of block length effects on nanophase separation, mechanical properties, and proton conductivity of PEM," *ACS Applied Materials & Interfaces*, vol. 6, no. 9, pp. 6851–6864, 2014.
- [40] W. Li, X. Guo, and J. Fang, "Synthesis and properties of sulfonated polyimide–polybenzimidazole copolymers as proton exchange membranes," *Journal of Materials Science*, vol. 49, no. 7, pp. 2745–2753, 2014.
- [41] J. Jang, D.-H. Kim, M.-K. Ahn et al., "Phosphoric acid doped triazole-containing cross-linked polymer electrolytes with enhanced stability for high-temperature proton exchange membrane fuel cells," *Journal of Membrane Science*, vol. 595, p. 117508, 2020.

Research Article

A Novel Gel Polymer Electrolyte by Thiol-Ene Click Reaction Derived from CO₂-Based Polycarbonate for Lithium-Ion Batteries

Wenhan Luo,^{1,2} Kuirong Deng,¹ Shuanjin Wang,¹ Shan Ren,¹ Dongmei Han,³ Yufei Wang,⁴ Min Xiao ,¹ and Yuezhong Meng ¹

¹The Key Laboratory of Low-carbon Chemistry & Energy Conservation of Guangdong Province/State Key Laboratory of Optoelectronic Materials and Technologies, School of Materials Science and Engineering, Sun Yat-sen University, Guangzhou 510275, China

²College of Light Industry and Food, Zhongkai University of Agriculture and Engineering, Guangzhou, China

³School of Chemical Engineering and Technology, Sun Yat-sen University, Zhuhai 519082, China

⁴Analytical and Testing Center of Guangzhou University, Guangzhou, China

Correspondence should be addressed to Min Xiao; stsxm@mail.sysu.edu.cn and Yuezhong Meng; mengyzh@mail.sysu.edu.cn

Received 16 February 2020; Accepted 9 June 2020; Published 17 July 2020

Academic Editor: Yohei Kotsuchibashi

Copyright © 2020 Wenhan Luo et al. This is an open access article distributed under the Creative Commons Attribution License, which permits unrestricted use, distribution, and reproduction in any medium, provided the original work is properly cited.

Here, we describe the synthesis of a CO₂-based polycarbonate with pendent alkene groups and its functionalization by grafting methoxypolyethylene glycol in view of its application possibility in gel polymer electrolyte lithium-ion batteries. The gel polymer electrolyte is prepared by an in-situ thiol-ene click reaction between polycarbonate with pendent alkene groups and thiolated methoxypolyethylene glycol in liquid lithium hexafluorophosphate electrolyte and exhibits conductivity as remarkably high as $2.0 \times 10^{-2} \text{ S cm}^{-1}$ at ambient temperature. To the best of our knowledge, this gel polymer electrolyte possesses the highest conductivity in all relevant literatures. A free-standing composite gel polymer electrolyte membrane is obtained by incorporating the gel polymer electrolyte with electrospun polyvinylidene fluoride as a skeleton. The as-prepared composite membrane is used to assemble a prototype lithium iron phosphate cell and evaluated accordingly. The battery delivers a good reversible charge-discharge capacity close to 140 mAh g⁻¹ at 1 C rate and 25°C with only 0.022% per cycle decay after 200 cycles. This work provides an interesting molecular design for polycarbonate application in gel electrolyte lithium-ion batteries.

1. Introduction

Rechargeable lithium-ion batteries manifest enormous daily influence in electrochemical devices for microchip technology, consumer electronics, battery electric vehicles, and industrial energy storage [1, 2]. The electrolyte, providing the passage of ions to create the battery current, is a primary component of lithium-ion battery [3, 4]. Liquid electrolytes generally consist of lithium salts and organic solvent, including ethylene carbonate, propylene carbonate, dimethyl carbonate, or diethyl carbonate. These most conventional and typical volatile organic solvents sometimes produce volatilization and leakage issues during long-term operation [5–8].

Solid polymer electrolytes (SPE), defined as a polymer matrix dispersed with lithium salts, possess improved safety features, minimized dendrite growth, and good processability. However, the high interfacial impedance, low conductivity, and high cost on the contrary limit their areal application [9–13]. As a compromise proposal, gel polymer electrolytes (GPE) possess advantageous characteristics including high reliability, nonleakage, as well as high corresponding performance. Plentiful polymer matrixes, such as polyethylene oxide (PEO), [14–16] polyvinyl chloride (PVC), [17, 18] polyacrylonitrile (PAN), [19, 20] poly(methyl methacrylate) (PMMA), [21, 22] polyvinylidene fluoride (PVDF), [23–25] and poly(vinylidene fluoride-hexafluoropropylene) (PVDF-

HFP) copolymer, [26, 27], have been widely studied as frameworks in GPE. However, some handicaps, such as low ionic conductivity and transfer number, of GPE impede the performance of homologous batteries [28–30]. Various efforts have been devoted to design and modify polymer structure in order to improve battery performance [31–34].

Polycarbonates synthesized from CO₂ and epoxides have received considerable attention [35–37]. Conversion of CO₂ into economic, environment-friendly, and functional polycarbonates has been achieved since the pioneers Inoue and coworkers in 1969 [38]. Poly(propylene carbonate) (PPC), one of the most extensively studied CO₂-based polycarbonates, has also been studied as GPE due to the similar structure to conventional carbonate-based solvents applied in electrolytes. Yu and coworkers prepared PPCMA gel polymer electrolyte by the terpolymer of carbon dioxide, propylene oxide, and maleic anhydride. The ionic conductivity of the GPE at room temperature reaches up to $8.43 \times 10^{-3} \text{ S cm}^{-1}$ [39]. Zhao and coworkers explored a rigid-flexible coupling cellulose-supported PPC polymer electrolyte using LiNi_{0.5}Mn_{1.5}O₄ salt. The polymer electrolyte exhibited wider electrochemical window up to 5.0 V, higher ion transference number of 0.68, and higher ionic conductivity of $1.14 \times 10^{-3} \text{ S cm}^{-1}$ with commercial separator at room temperature [40]. Zhou and coworkers prepared a series of ionic liquid polymer electrolytes composed of PPC host, LiClO₄ and 1-butyl-3-methylimidazolium tetrafluoroborate (BMIM⁺BF₄⁻), which exhibits a high ionic conductivity of $1.5 \times 10^{-3} \text{ S cm}^{-1}$ at room temperature [41]. Huang and coworkers developed poly(propylene carbonate)/poly(methyl methacrylate)-coated polyethylene gel polymer electrolyte, poly(vinylidene fluoride)/poly(propylene carbonate) gel polymer electrolyte, and polybutadiene rubber-interpenetrating cross-linking poly(propylene carbonate) network gel polymer electrolytes by physical blending methods and the corresponding coin cells achieve good charge-discharge capacity, cyclic stability, and rate performance [42–44]. In our previous work, CO₂-based and fluorinated polysulfonamide single-ion conducting CO₂-based polymer electrolytes for lithium-ion batteries has also been achieved, but the Li-ion conductivity was still low [45, 46].

No relevant research has ever reported GPE conductivity with the same order of magnitude compared to their liquid counterparts ($\sigma \approx 10^{-2} \text{ S cm}^{-1}$). In this work, we describe a novel GPE derived from functionalized CO₂-base polycarbonate to improve the lithium ionic conductivity and battery performance. This GPE was prepared from the terpolymer of propylene oxide (PO), allyl glycidyl ether (AGE), and CO₂. Functional thiolated polyethylene glycol (mPEG-SH) was grafted to the side chains through the thiol-ene click reaction. Compared to normal linear polycarbonate, the long, flexible branch group of PEG units benefits segmental mobility, which can improve the transport of lithium ions. The application feasibility in high-performance LIBs of this GPE is explored by electrochemical stability and ionic conductivity test. A skeleton of PVDF serves as a supporter and separator to manufacture composite membrane. The cell performance of the composite GPE was also evaluated.

2. Experimental

2.1. Materials. Propylene oxide (PO) and allyl glycidyl ether (AGE) were refluxed over CaH₂ for 20 hours and distilled under high pure nitrogen gas before use. Carbon dioxide of 99.99% purity was supplied from a high-pressure cylinder equipped with copper pipe and relief valves. Zinc glutarate (ZnGA) catalyst was prepared according to our previous work [47]. 3-Mercaptopropionic acid (MPA, 99%), methoxy-polyethylene glycol (mPEG, average molecular 2000), 2,6-di-tert-butyl-4-methylphenol (BHT, 99.5%), p-toluenesulfonic acid (PTSA, 99%), and 2,2-dimethoxy-2-phenylacetophenone (DMPA, 99%) were purchased from Aladdin. LiFePO₄ (MTI Kejing Co., Ltd), Super P (TIMCAL), and poly(vinylidene-fluoride) (PVDF, Arkema) were used as received without further purification. Solvents such as methanol, tetrahydrofuran, dichloromethane, hydrochloric acid, and diethyl ether were all analytical reagent grade and used without any further treatment.

2.2. Synthesis of PPCAGE. A 500 mL high-pressure autoclave equipped with a programmable temperature controller and a stainless-steel mechanical stirrer was used to carry out the terpolymerization of PO, AGE, and CO₂. Typically, 1.0 g ZnGA catalyst was placed into the autoclave. Then, the autoclave with the catalyst inside was sealed and further dried for 6 h under vacuum at 120°C. After cooling down to room temperature, PO and AGE with 8:2 molar ratio were inhaled into the vacuumed autoclave immediately. Then, the autoclave was pressurized to 5.0 MPa with CO₂ and maintained at 60°C. After 40 hours, the autoclave was cooled down and CO₂ pressure release following. The primeval polymer was dissolved in moderate dichloromethane and 0.5 g of BHT was appended into the solution to prevent the self-crosslinking phenomenon. The viscous solution polymer solution acid was poured into high-speed stirred cold ethanol detergent with 5% hydrochloric until all albus polymer was precipitated. The purification was repeated twice to completely remove catalyst and monomers. The ultimate polymer precipitates (PPCAGE) were dried under vacuum at 50°C for more than 24 h to pull out the solvent.

2.3. Thiolation of mPEG Using Mercaptoacetic Acid. A quantity of 12.0 g (6 mmol) mPEG and 6.36 g (60 mmol) MPA were dissolved in 100 mL toluene. The mixture was stirred and heated to 50°C. Then, 0.109 g (0.6 mmol) of PTSA was introduced into the solution. The thiolation reaction waged after the solution further heated to 130°C, stirred, and refluxed overnight in a dean-stark apparatus. A small quantity was analyzed by ¹H NMR to verify the complete reaction. The crude mixture was refined by precipitating in 2 L of ether. The mPEG-SH intermediate yield was 94% (11.86 g).

2.4. In-Situ Preparation of GPE@PVDF Membrane. Electrospun PVDF membrane was obtained according to Huang's work [34]. A typical 10% polymer content gel electrolyte precursor was prepared as follow: 0.202 g (0.33 mmol alkene) PPCAGE, 0.693 g (0.33 mmol) mPEG-SH, and 8.45 mg (0.033 mmol) of DMPA were dissolved in 8.05 g of 1 M LiPF₆/EC/DMC liquid electrolyte followed by stirring for 4 h till

all polymer dissolved. 20 μL precursor was added dropwise onto the PVDF membrane. After 5 min soak, the composite membrane was exposed to UV light (365 nm) for 10 min, then the membrane was ready to test and assemble cell.

2.5. Materials Characterization. ^1H NMR spectra of the polymers were recorded by Bruker DRX-500 NMR spectrometer, using chloroform-d (CDCl_3) as solvent and tetramethylsilane as internal standard. Polymer molecular weight (M_w and M_n) of resultant product was measured by gel permeation chromatography (GPC) system (Waters 515 HPLC Pump, Waters 2414 detector) with a set of columns (Waters Styragel 500, 10,000, and 100,000 \AA) and chloroform (HPLC grade) as eluent. Glass transition temperature (T_g) of the samples was determined from the second heating run by a differential scanning calorimeter (DSC, Netzsch Model 204).

2.6. Ionic Conductivity Measurement. Ionic conductivities of the PPCAGE-g-mPEG GPEs were demonstrated by electrochemical impedance spectroscopy (EIS). The GPEs were in-situ prepared in an electrolytic tank in an argon atmosphere inside a glovebox. The equipment was placed into a self-designed vessel alongside a temperature controller. Electrochemical impedance spectroscopy in the 1 Hz to 1 MHz frequency range with an AC excitation voltage of 10 mV A was recorded by a Solartron 1255B frequency response analyzer in a temperature range of 25 to 80°C after maintaining the samples at each test temperature for over 1 h till thermal equilibration state. The bulk resistance can be calculated according to the equivalent fit circuit model to the data. The ionic conductivity (σ) was calculated by the equation as follow:

$$\sigma = \frac{L}{R_b A}, \quad (1)$$

where L is the thickness of the sample, R_b is the bulk resistance, and A is the effective overlap area of the sample.

2.7. Electrochemical Stability Window Measurement. The electrochemical stability window was determined by linear sweep voltammetry (LSV). GPE@PVDF membrane was stacked up with lithium foil as a reference electrode between stainless steel working electrodes. The tests were performed between 0 and 6.0 V (vs. Li/Li^+) at the scan rate of 1 mV s^{-1} .

2.8. Assemble LFP/GPE@PVDF/Li Coin Cell. With a weight ratio of 80:10:10, lithium iron phosphate (LFP), carbon black (CB), and PVDF were mixed up and grinded in NMP. The above mixture was then cast onto aluminum foil and dried at 80°C to prepare the cathode plate. The loading of LFP is around 1.7 mg cm^{-2} . The battery was assembled by sandwiched LFP plate, GPE@PVDF membranes (PVDF/liquid electrolyte membrane for comparison), and Li wafer seriatim. Then, the battery was sealed into a 2032 type coin cell by a tablet press. Charge and discharge tests for all batteries were performed at room temperature in a calorstat. The upper cut-off voltage was set at 4.0 V and the lower cut-off voltage at 2.5 V.

3. Results and Discussion

3.1. Terpolymerization of PO, AGE, and CO_2 . Terpolymerization of PO, AGE, and CO_2 (Scheme 1 and Table S1) was successfully realized using ZnGA as an effective catalyst under 5.0 MPa CO_2 atmosphere at 60°C in a high-pressure autoclave.

The ^1H NMR spectrum of purified terpolymers (PPCAGE) is shown in Figure 1. The chemical shift at 5.1–5.3 ppm and 5.8 ppm correspond to allyl groups $-\text{CH}=\text{CH}_2$ from allyl glycidyl ether monomer, showing that the AGE units were incorporated into the PPC mainchain successfully. The resonance peaks at 4.2 and 5.0 ppm are assigned to CH_2 and CH in the carbonate unit, respectively. The tiny peaks at 3.4–3.7 ppm corresponding to ether linkages indicate that the terpolymer is an alternating copolymer of epoxides and CO_2 , consisting of PO- CO_2 carbonate units and AGE- CO_2 carbonate units. The mole percentage of the AGE- CO_2 carbonate unit is 12.2% according to the peak area of the peak at 5.8 ppm and 5.0 ppm. The resulting PO versus AGE ratio within the terpolymers is higher than the feed ratio, which illustrates that the polymerization reactivity of PO is higher than that of AGE.

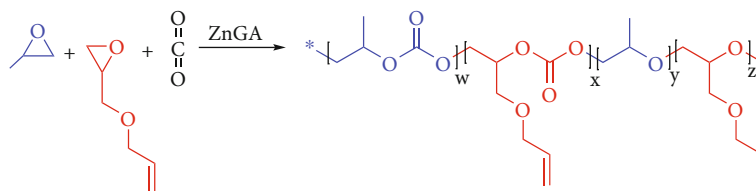
A unimodal GPC trace of polymer product shown in Figure S1 indicates the molecular weight of 68400 and provides the direct evidence that the resulting polymer is a terpolymer rather than a mixture of PPC homopolymer and PAGEC homopolymer. Usually, the GPC trace of the mixture will more likely to be multiplet.

DSC measurement shows the amorphous character of the terpolymers, without any melting point (Figure S2). The glass transition temperature of the terpolymers is lower than 11.0°C. This is because that AGE units possess a flexible long pendant group, which favors segmental motion. The PPCAGE polymer is further functionalized to prepare new brand gel polymer electrolytes (GPEs). TGA curve of terpolymer PPCAGE also shows a decomposition temperature around 300°C (Figure S3).

3.2. Thiolation of Polyethylene Glycol Methyl Ether. Synthesis of thiol-functionalized mPEG-SH (Scheme 2) were achieved by esterification coupling between the hydroxyl end of mPEG and the carboxylic acid groups of MPA using PTSA as catalyst and toluene as solvent.

After precipitating the products in ether to remove MPA unit and PTSA catalyst, ^1H NMR spectra (Figure 2(a)) was used for product identification. The proton peaks at 1.6–1.7 ppm correspond to thiol proton. Peaks at 2.7–2.8 ppm correspond to the proton covalent in methylene next to thiol group. Peaks at 3.7 ppm correspond to PEG backbone. In particular, the peaks at 3.7 ppm and 4.3 ppm prove a successful couple between mPEG and MPA. FTIR spectroscopy further confirmed that thiol groups are present in the product (S-H stretch at 2550 cm^{-1}), as shown in Figure 2(b).

3.3. Grafting mPEG on PPCAGE via Thiol–Ene Click Reaction. Synthesis of PPCAGE-g-mPEG grafted polymer was successfully realized by a rapid thiol-ene click reaction with high reaction selectivity and conversion, quick reaction



SCHEME 1: Terpolymerization of propylene oxide (PO), allyl glycidyl ether (AGE), and carbon dioxide (CO_2) catalyzed by ZnGA.

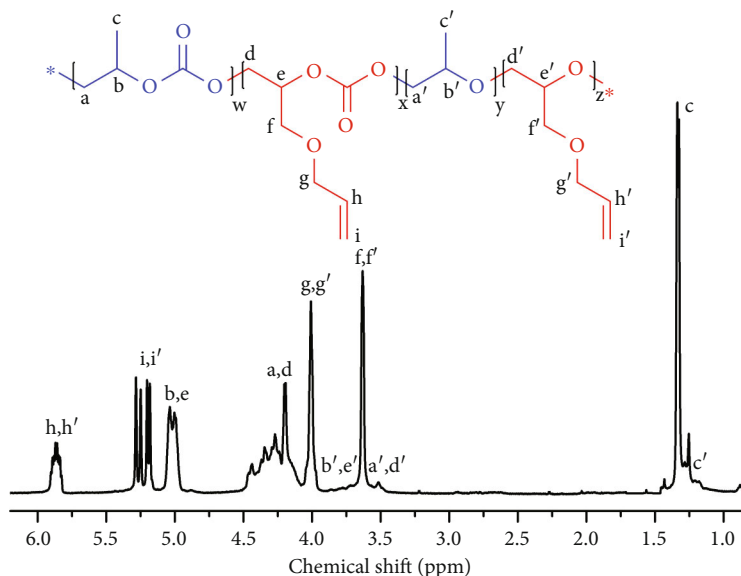
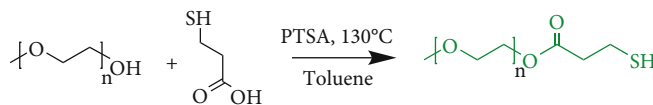


FIGURE 1: ^1H -NMR spectrum of terpolymer PPCAGE.



SCHEME 2: Thiolation of polyethylene glycol monomethyl ethers with MPA.

rate, as well as moderate reaction conditions. Thiolated mPEG-SH can be easily grafted onto PPCAGE side chain via thiol-ene click reaction employing DMPA as photoinitiator in common 1 M $\text{LiPF}_6/\text{EC}/\text{DMC}$ liquid electrolyte (Scheme 3).

The ^1H NMR spectrum of the resulting mPEG-grafted pendant polymer (PPCAGE-g-mPEG) is shown in Figure 3. The methylene proton signals of the pendant mPEG are distinctly visible at 2.6 ppm and 2.8 ppm, which evidence the objective functionalization reaction. Disappearance of peaks at 5.1 to 5.3 ppm and 5.8 ppm corresponding to the proton in allyl groups $-\text{CH}=\text{CH}_2$ confirms the complete conversion of the alkene groups. A photo was taken to show the polymer solution transform before and after UV-irradiation (inserted in Figure 3), showing the mixture changed from cloudy solution into uniform and transparent gel. Another proof is given by IR and TGA spectrum in Figures S4 and S5.

3.4. Ionic Conductivity of GPEs. Figure 4 and Table S2 demonstrate the correspondence of ionic conductivity (σ) with temperature and polymer content in GPE. The ion

conductivity of LiPF_6 liquid electrolyte is $2.3 \times 10^{-2} \text{ S cm}^{-1}$ at 25°C . Apparently from the experiment result, the ionic conductivity of GPE decreases with PPCAGE-g-mPEG polymer content increasing. The value decreases to 2.0×10^{-2} , 1.7×10^{-2} , 1.5×10^{-2} , and $6.6 \times 10^{-3} \text{ S cm}^{-1}$ when polymer content is 5 wt.%, 10 wt.%, 20 wt.% and 30 wt.%, in turns. According to the ion conduction mechanism in a similar system [43, 48], lithium-ion can shuttle back and forth through the gel layer via both liquid state route and polymer state route. It is reasonable since the ion conductivity depends on the concentration of Li^+ and mobility of Li^+ . The more the PPCAGE-g-mPEG solid content, the less the concentration and mobility of Li^+ , thus the lower the ionic conductivity is. To better understand the ion conduction behavior in a polymer electrolyte, the activation energy E_a can be estimated by fitting the curves in Figure 4 to Arrhenius equation:

$$\sigma = \sigma_0 \exp\left(\frac{-E_a}{RT}\right), \quad (2)$$

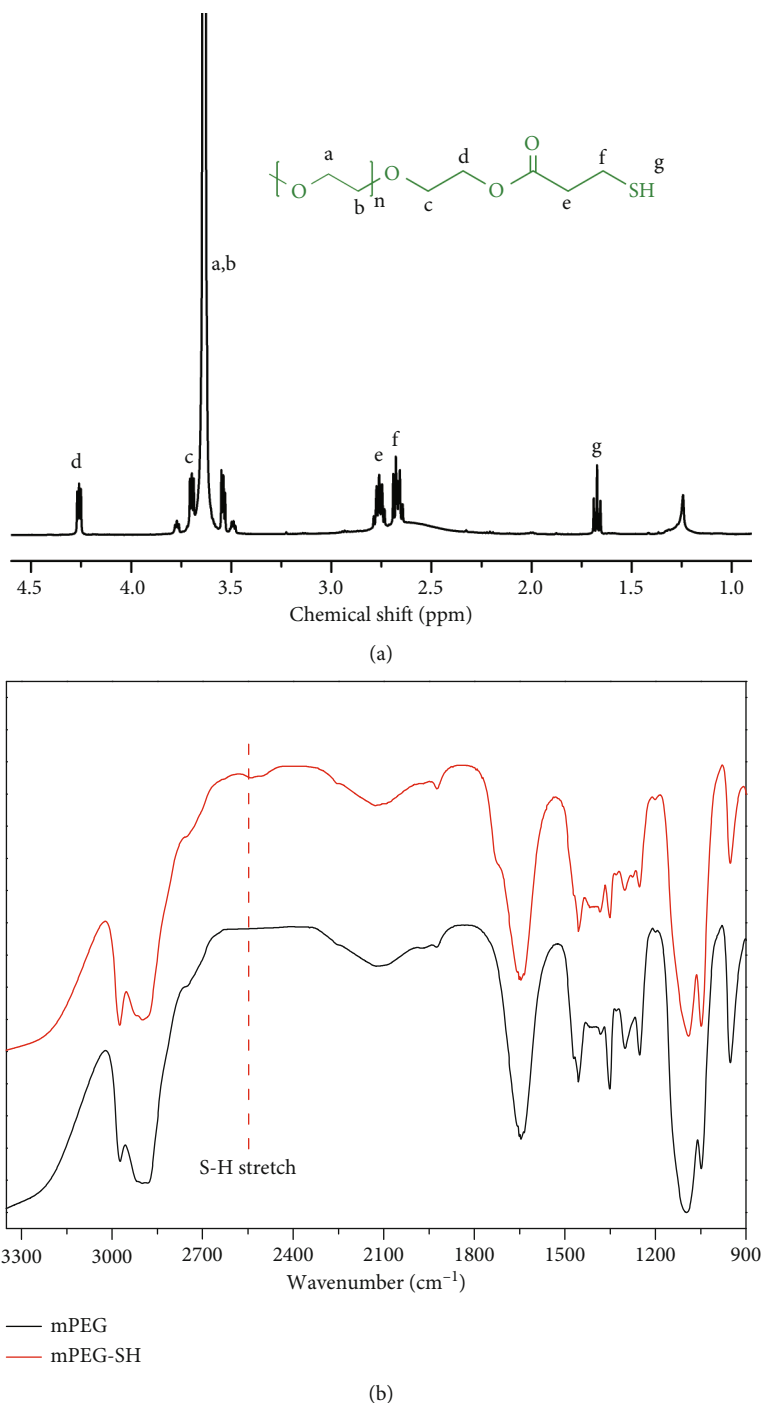
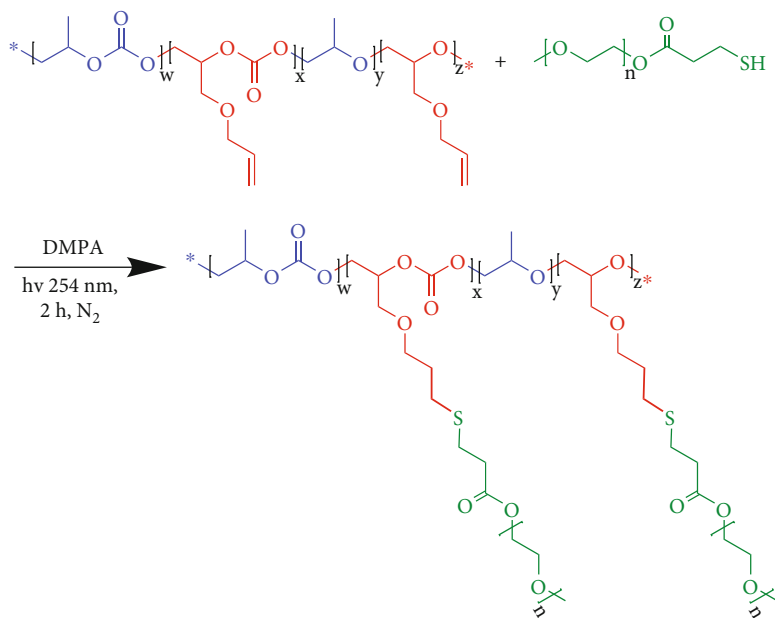


FIGURE 2: (a) ¹H-NMR spectrum of mPEG-SH; (b) IR spectrum of mPEG before and after thiolation.

Where σ is the ionic conductivity, σ_0 is a pre-exponential factor, R is the Boltzmann constant, and T is the temperature. E_a could be calculated from the slopes of the linear relationship. The E_a value of the GPE with 5 wt.%, 10 wt.%, 20 wt.%, and 30 wt.% polymer contents are in turns incremental 1.02, 1.21, 1.27, and 1.90 kJ mol⁻¹. On the base of free volume model, the activation energy depends on the mobility of ion carriers [49]. This is reasonable since the increase in PPCAGE-g-mPEG polymer matrix content

can affect liquid electrolyte ratio, which involuntarily results in mobility descension of the carriers.

3.5. Fabrication of GPE@PVDF Membrane. Because of sticky nature and weak strength of PPCAGE-g-mPEG gel electrolyte, it is hard to scissors into a desire shape. An electrospun PVDF membrane was utilized to be the scaffold. In the line of the preparation method given in Section 2.4, the grafted polymer gel was incorporated into surface



SCHEME 3: Synthesis of PPCAGE-g-mPEG grafted polymer.

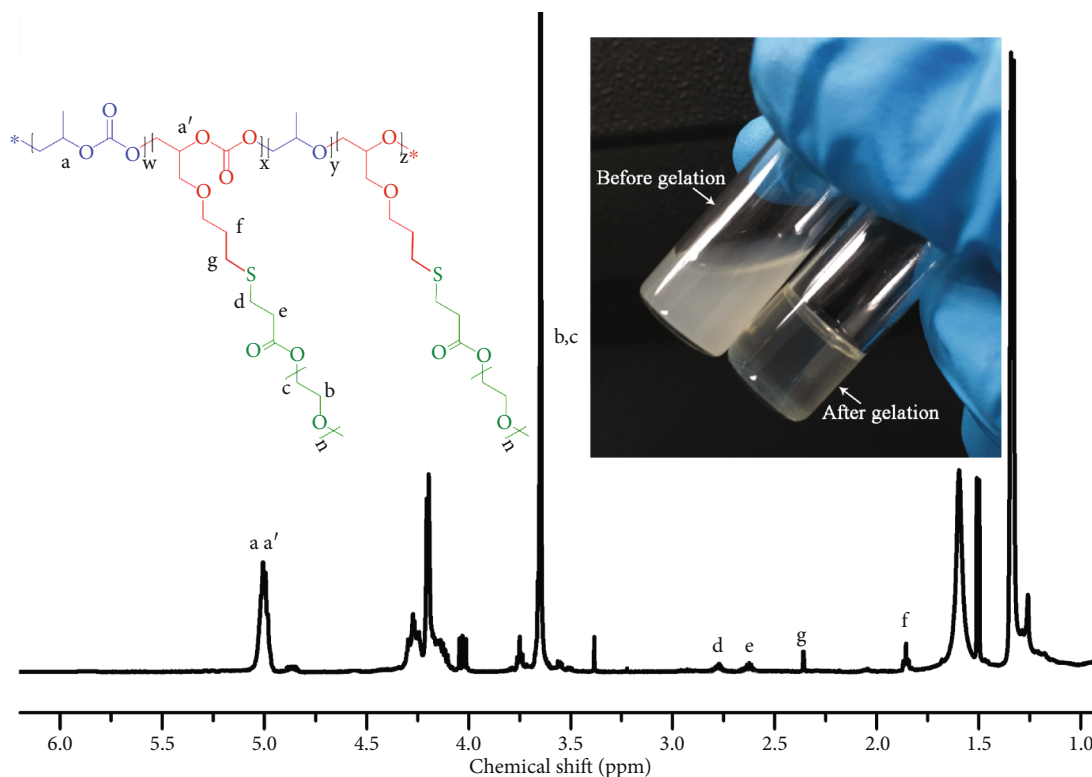


FIGURE 3: ¹H-NMR spectrum of PPCAGE-g-mPEG with inserting photo of the polymer solution before and after UV-irradiation.

and pores of PVDF separator to fabricate GPE@PVDF composite membrane. The morphologies of electrospun PVDF membrane and the composite gel electrolyte membrane are clearly observed from SEM images shown in Figure 5.

The primary PVDF separator has a visibly fibrous and porous structure. While PVDF skeleton is crop-full by PPCAGE-g-mPEG gel, the surface of PVDF separator is also soaked with gel mass. A notable feature is the transformation of PVDF surface morphology. With increasing polymer gel

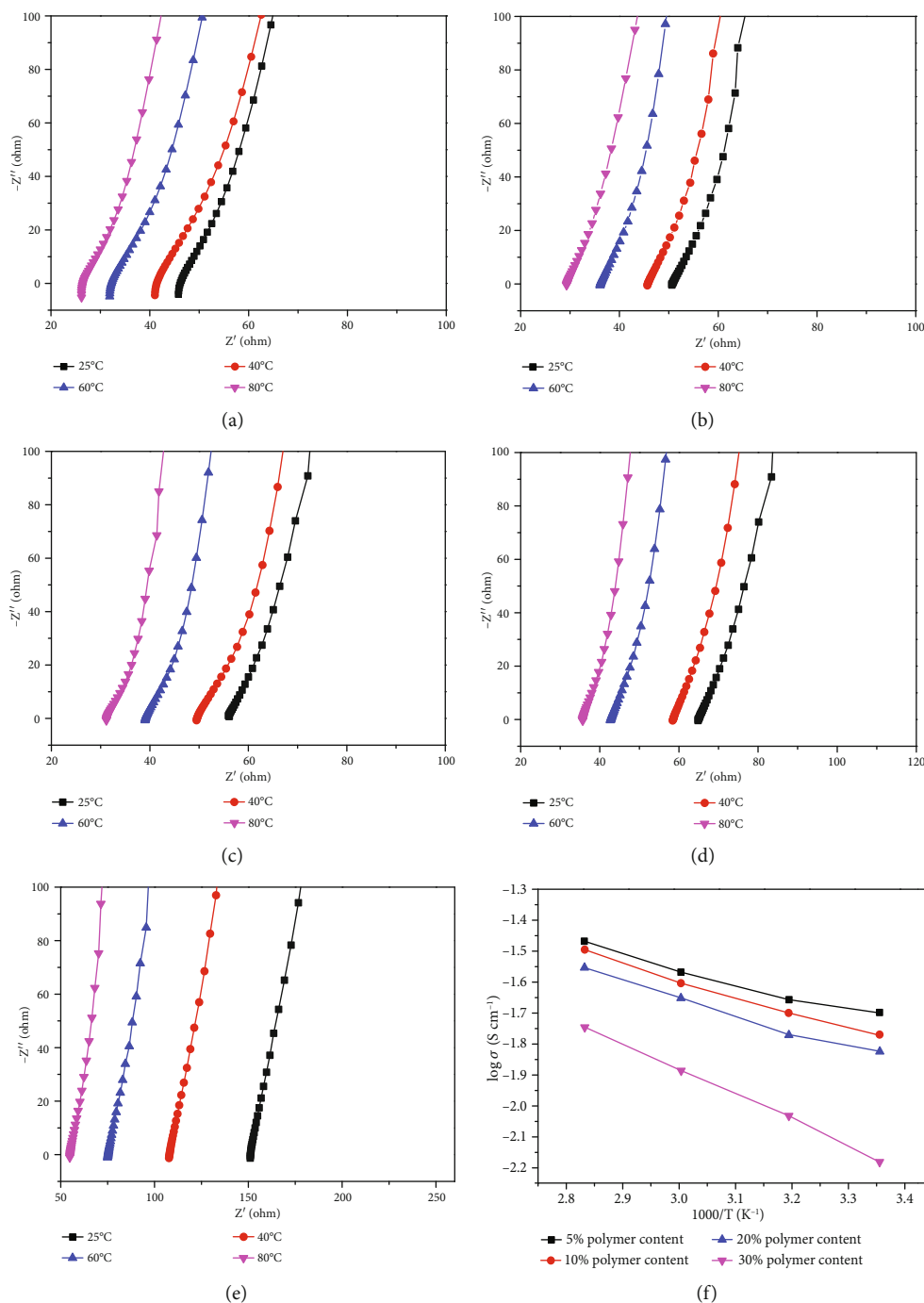


FIGURE 4: EIS plots for (a) liquid electrolyte and (b) 5% polymer content, (c) 10% polymer content, (d) 20% polymer content, (e) 30% polymer content PPCAGE-g-PEG gel at different temperatures. (f) Temperature characteristic curves of ionic conductivity of PPCAGE-g-mPEGs with different polymer content.

concentration, the surface pore can be fully covered by a PPCAGE-g-mPEG gel layer. The white porous PVDF membrane becomes transparent as shown in Figure 5(d). Sulphur (root in original thiol group) distribution (Figure 5(c)) indicates a uniform distribution of PPCAGE-g-mPEG in composite membrane.

3.6. Electrochemical Stability of the GPE@PVDF Membrane. For commercial lithium ion battery, the potential can hit

as high as 4.0 V vs. Li/Li $^{+}$. Therefore, the gel polymer electrolyte (GPE) needs be electrochemically stable at least over 4.0 V. Figure 6 shows the linear sweep voltammetry curves of the cells employing GPE (10% polymer content) @ PVDF membrane as a separator. No rapid rise in current is detected till 4.5 V vs. Li/Li $^{+}$ for the GPE@PVDF membrane, indicating that the gel polymer electrolyte may be compatible with commercial lithium-ion battery. The conductivity of the GPE@PVDF membrane is

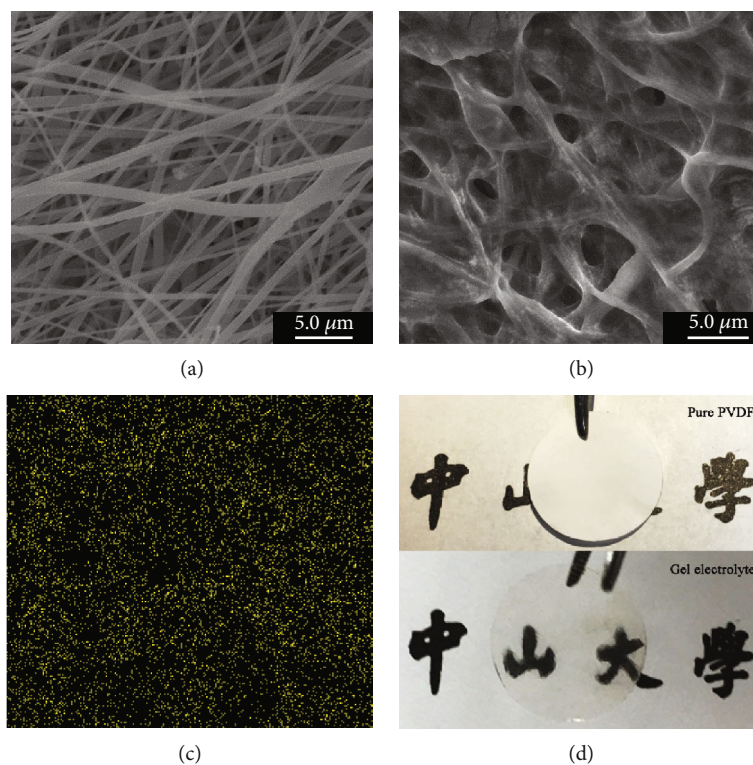


FIGURE 5: (a) SEM image of original PVDF separator, (b) SEM image of GPE@PVDF membrane, (c) Sulphur distribution in GPE@PVDF membrane, and (d) Photos of PVDF separator and GPE @ PVDF membrane.

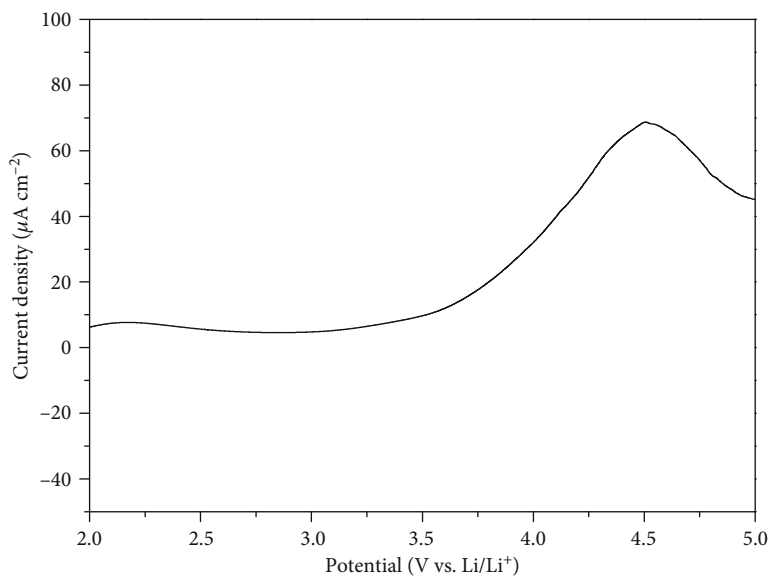


FIGURE 6: Linear sweep voltammogram of GPE@PVDF membrane.

calculated to $1.4 \times 10^{-3} \text{ S cm}^{-1}$ from Figure S6. Values of initial and steady-state currents (I_0 , I_S), and interfacial resistances (R_0 , R_S) of symmetric Li/Li⁺ cells with the GPE@PVDF membrane were evaluated by polarization curves and impedance spectra as shown in Table S3 and Figure S7. It is believed that GPE@PVDF possesses better

T_{Li^+} (lithium transference numbers) compared to the pure PVDF membrane.

3.7. *Battery Performances.* The applicability of the GPE@PVDF membrane was further estimated by cell assembly with metallic lithium foil anode and LFP cathode.

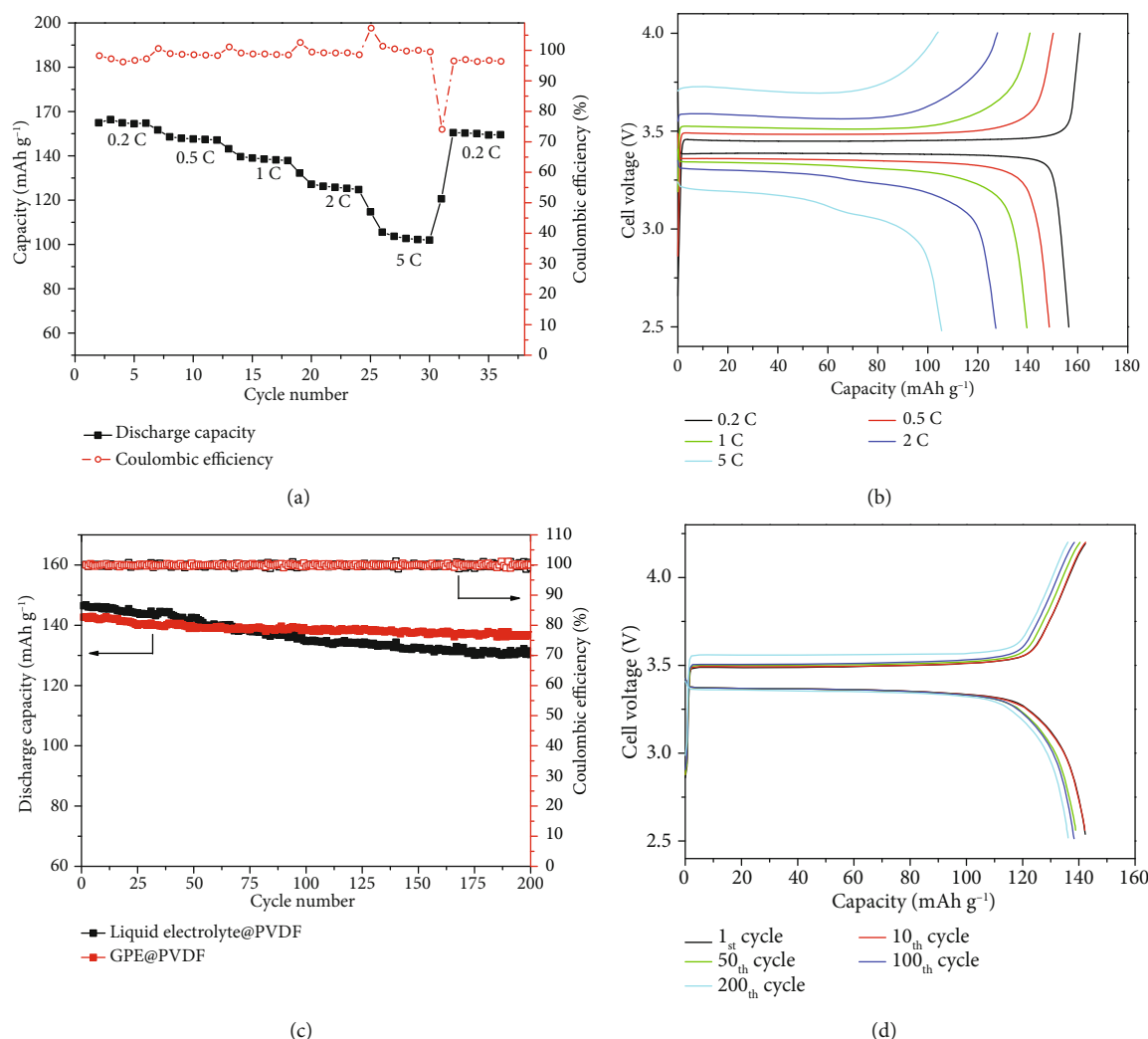


FIGURE 7: (a) Rate performance and (b) typical charge–discharge curves at various rates of GPE (10% polymer content) @ PVDF membrane cells; (c) cycling performance of liquid electrolyte @ PVDF cells and GPE (10% polymer content) @ PVDF membrane cells at 1 C; (d) typical charge–discharge curves of GPE (10% polymer content) @ PVDF membrane cells at 1 C.

Figure 7(a) shows the rate performances of the cells using GPE (10% polymer content) @ PVDF membrane at 25°C. Relatively stable capacities around average 163.4, 150.3, 141.6, 129.4, and 107.2 mAh g⁻¹ are obtained at current rates of 0.2 C, 0.5 C, 1 C, 2 C, and 5 C, in their turns. The capacity at 5 C current rate retains 66% of original capacity at 0.2 C. As the current rate reverses back to 0.2 C, the initial capacity retains at 161.2 mAh g⁻¹, very close to initial capacity. Figure 7(b) shows the charge-discharge profiles of rate performance GPE@PVDF membrane cell. Flat voltage plateaus at around 3.5 V for battery charging and 3.4 V for battery discharging correspond to Fe³⁺/Fe²⁺ reversible redox couple reaction on the cathode [33]. At the initial charge or discharge stage, the terminal voltage of the battery rises or drops rapidly. The higher charge-discharge rate is, the faster battery voltage rises or drops. When the battery voltage enters a slowly changing platform area, the lower the charge or discharge rate is, the longer the platform area lasts and the slower the voltage rises or drops. These features are quite similar to liquid electrolyte batteries.

Figure 7(c) shows the cycling performances of liquid electrolyte @ PVDF cell and GPE (10% polymer content) @ PVDF membrane cell at 1 C at room temperature. Both of the two cells displayed good cycling performance with trifling capacity loss over 200 cycles at 1 C rate. The specific capacity of LFP cathode in GPE@PVDF membrane cell remained as high as 136.4 mAh g⁻¹ after 200 cycles with a decay rate of only 0.022% per cycle. On the contrast, LFP cathode in liquid electrolyte @ PVDF cells is 130.4 mAh g⁻¹ after 200 cycles with a decay rate of 0.055% per cycle. This result indicates that GPE @ PVDF membrane cell is more stable. One important reason for the decrease of battery stability is the lithium dendrite formed in the cathode. Polymer gel inhibits the generation of lithium dendrite and protects the cathode thus the stability of the battery is improved. On the other hand, a stable and uniform solid electrolyte interface (SEI) layer between polymer gel and the cathode can be formed in the charge and discharge processes. This passivation layer possesses the electronic-insulating characteristic similar to the

solid electrolyte as well as excellent lithium-ion conductivity. Lithium-ion can embed and strip freely through the passivation layer without making the cathode corrosion, so as to improve the stability of the battery.

Figure 7(d) shows the cycling performance of GPE@PVDF membrane cells. According to the low voltage polarization and stable cycle capacity, as both electrolyte and separator, the GPE@PVDF membrane provides good electrochemical performances for the cell operation. The competitive results for the electrolyte systems demonstrate that the PPCAGE-g-mPEG gel electrolyte has potential applications in lithium-ion batteries applying.

4. Conclusions

Terpolymer (PPCAGE) with alkene pendent can be readily synthesized by terpolymerization of PO, AGE, and CO₂ employing ZnGA as catalyst. This alkene pendent can be subsequently functionalized via rapid and efficient thiol-ene click reaction with mPEG-SH in liquid electrolyte, to afford a new kind of gel polymer electrolyte. The novel gel polymer electrolyte manifests the highest ionic conductivity as high as $2.0 \times 10^{-2} \text{ S cm}^{-1}$ at 25°C. Meanwhile, LFP batteries with GPE@PVDF membrane as both separator and electrolyte show good rate performances and cycling performances. In conclusion, this work provides an alternative and efficient way to prepare a brand-new gel polymer electrolyte for lithium battery application utilizing environmentally friendly PEG grafted CO₂-based polycarbonate.

Data Availability

The authors confirm that the data supporting the findings of this study are available within the article and its supplementary materials.

Conflicts of Interest

The authors declare that they have no conflicts of interest.

Acknowledgments

The work was supported by the National Natural Science Foundation of China (U1601211, 51573215, 21506260, and 21706294), the Guangdong Province Sci & Tech Bureau (2017B090901003, 2016B010114004, and 2016A050503001), the Natural Science Foundation of Guangdong Province (2016A030313354), the Special Project on the Integration of Industry, Education and Research of Guangdong Province (2015B09090100), the Guangzhou Scientific and Technological Planning Project (201607010042, 201707010424, and 201804020025), the Fundamental Research Funds for the Central Universities (171gjc37), the University Research Project of Guangzhou 1201630241, and the Science and Technology Research Project of Guangzhou (Grant No. 201707010289).

Supplementary Materials

Figure S1: GPC curve of terpolymer PPCAGE with feed ratio of 80:20 (PO:AGE). Figure S2: DSC curve of terpolymer PPCAGE with feed ratio of 80:20 (PO:AGE). Figure S3: TGA curve of terpolymer PPCAGE with feed ratio of 80:20 (PO:AGE). Figure S4: IR spectrum of PPCAGE-g-mPEG showing a successful couple between PPCAGE and mPEG-SH. Figure S5: TGA curve of grafted polymer PPCAGE-g-mPEG. Figure S6: EIS plots for GPE @ PVDF membrane at room temperatures. The conductivity of the membrane is calculated to $1.4 \times 10^{-3} \text{ S cm}^{-1}$. Figure S7: polarization curves and impedance spectra of (a) liquid electrolyte @ PVDF and (b) GPE@PVDF membrane with 10% polymer gel content. Table S1: results of the terpolymerization of CO₂, PO, and AGE catalyzed by ZnGA. Table S2: conductivity of PPCAGE-g-PEG gel electrolyte at different temperature. Table S3: values of initial and steady-state currents (I₀, I_S), and interfacial resistances (R₀, R_S) of symmetric Li/Li⁺ cells with the GPE @ PVDF membrane. (*Supplementary Materials*)

References

- [1] L. Liu and C. Sun, "Flexible quasi-solid-state composite electrolyte membrane derived from a metal-organic framework for lithium-metal batteries," *ChemElectroChem*, vol. 7, no. 3, pp. 707–715, 2020.
- [2] S. Li, X. Meng, Q. Yi et al., "Structural and electrochemical properties of LiMn_{0.6}Fe_{0.4}PO₄ as a cathode material for flexible lithium-ion batteries and self-charging power pack," *Nano Energy*, vol. 52, pp. 510–516, 2018.
- [3] S. Huang, R. Guan, S. Wang et al., "Polymers for high performance Li-S batteries: material selection and structure design," *Progress in Polymer Science*, vol. 89, pp. 19–60, 2019.
- [4] K. Xu, "Nonaqueous liquid electrolytes for lithium-based rechargeable batteries," *Chemical Reviews*, vol. 104, no. 10, pp. 4303–4418, 2004.
- [5] A. Lewandowski and A. Świdarska-Mocek, "Ionic liquids as electrolytes for Li-ion batteries—an overview of electrochemical studies," *Journal of Power Sources*, vol. 194, no. 2, pp. 601–609, 2009.
- [6] D. Aurbach, Y. Ein-Ely, and A. Zaban, "The surface chemistry of lithium electrodes in alkyl carbonate solutions," *Journal of the Electrochemical Society*, vol. 141, no. 1, pp. L1–L3, 1994.
- [7] M. Ishikawa, T. Sugimoto, M. Kikuta, E. Ishiko, and M. Kono, "Pure ionic liquid electrolytes compatible with a graphitized carbon negative electrode in rechargeable lithium-ion batteries," *Journal of Power Sources*, vol. 162, no. 1, pp. 658–662, 2006.
- [8] P. G. Balakrishnan, R. Ramesh, and T. Prem Kumar, "Safety mechanisms in lithium-ion batteries," *Journal of Power Sources*, vol. 155, no. 2, pp. 401–414, 2006.
- [9] J. W. Fergus, "Ceramic and polymeric solid electrolytes for lithium-ion batteries," *Journal of Power Sources*, vol. 195, no. 15, pp. 4554–4569, 2010.
- [10] X. Li, J. Liu, M. N. Banis et al., "Atomic layer deposition of solid-state electrolyte coated cathode materials with superior high-voltage cycling behavior for lithium ion battery application," *Energy & Environmental Science*, vol. 7, no. 2, pp. 768–778, 2014.

- [11] K. Yamamoto, Y. Iriyama, T. Asaka et al., "Direct observation of lithium-ion movement around an in-situ-formed-negative-electrode/solid-state-electrolyte interface during initial charge-discharge reaction," *Electrochemistry Communications*, vol. 20, pp. 113–116, 2012.
- [12] Y. Li, W. Zhou, S. Xin et al., "Fluorine-doped antiperovskite electrolyte for all-solid-state lithium-ion batteries," *Angewandte Chemie International Edition*, vol. 55, no. 34, pp. 9965–9968, 2016.
- [13] J. Li, C. Ma, M. Chi, C. Liang, and N. J. Dudney, "Solid electrolyte: the key for high-voltage lithium batteries," *Advanced Energy Materials*, vol. 5, no. 4, p. 1401408, 2015.
- [14] Y. Kang, K. Cheong, K. A. Noh, C. Lee, and D. Y. Seung, "A study of cross-linked PEO gel polymer electrolytes using bisphenol A ethoxylate diacrylate: ionic conductivity and mechanical properties," *Journal of Power Sources*, vol. 119–121, pp. 432–437, 2003.
- [15] H. Li, X. T. Ma, J. L. Shi, Z. K. Yao, B. K. Zhu, and L. P. Zhu, "Preparation and properties of poly (ethylene oxide) gel filled polypropylene separators and their corresponding gel polymer electrolytes for Li-ion batteries," *Electrochimica Acta*, vol. 56, no. 6, pp. 2641–2647, 2011.
- [16] J. H. Shin, W. A. Henderson, and S. Passerini, "PEO-based polymer electrolytes with ionic liquids and their use in lithium metal-polymer electrolyte batteries," *Journal of the Electrochemical Society*, vol. 152, no. 5, pp. A978–A983, 2005.
- [17] S. Rajendran, R. Babu, and P. Sivakumar, "Optimization of PVC- PAN-based polymer electrolytes," *Journal of Applied Polymer Science*, vol. 113, no. 3, pp. 1651–1656, 2009.
- [18] P. Vickraman and S. Ramamurthy, "A study on the blending effect of PVDF in the ionic transport mechanism of plasticized PVC-LiBF₄ polymer electrolyte," *Materials Letters*, vol. 60, no. 28, pp. 3431–3436, 2006.
- [19] S. W. Choi, J. R. Kim, S. M. Jo, W. S. Lee, and Y. R. Kim, "Electrochemical and spectroscopic properties of electrospun PAN-based fibrous polymer electrolytes," *Journal of the Electrochemical Society*, vol. 152, no. 5, pp. A989–A995, 2005.
- [20] P. Carol, P. Ramakrishnan, B. John, and G. Cheruvally, "Preparation and characterization of electrospun poly (acrylonitrile) fibrous membrane based gel polymer electrolytes for lithium-ion batteries," *Journal of Power Sources*, vol. 196, no. 23, pp. 10156–10162, 2011.
- [21] P. Meneghetti, S. Qutubuddin, and A. Webber, "Synthesis of polymer gel electrolyte with high molecular weight poly (methyl methacrylate)-clay nanocomposite," *Electrochimica Acta*, vol. 49, no. 27, pp. 4923–4931, 2004.
- [22] S. Ramesh and G. P. Ang, "Impedance and FTIR studies on plasticized PMMA-LiN(CF₃SO₂)₂ nanocomposite polymer electrolytes," *Ionics*, vol. 16, no. 5, pp. 465–473, 2010.
- [23] X. Wang, C. Gong, D. He et al., "Gelled microporous polymer electrolyte with low liquid leakage for lithium-ion batteries," *Journal of Membrane Science*, vol. 454, pp. 298–304, 2014.
- [24] S. W. Choi, S. M. Jo, W. S. Lee, and Y. R. Kim, "An electrospun poly (vinylidene fluoride) nanofibrous membrane and its battery applications," *Advanced Materials*, vol. 15, no. 23, pp. 2027–2032, 2003.
- [25] J. R. Kim, S. W. Choi, S. M. Jo, W. S. Lee, and B. C. Kim, "Electrospun PVDF-based fibrous polymer electrolytes for lithium ion polymer batteries," *Electrochimica Acta*, vol. 50, no. 1, pp. 69–75, 2004.
- [26] Z. H. Li, C. Cheng, X. Y. Zhan, Y. P. Wu, and X. D. Zhou, "A foaming process to prepare porous polymer membrane for lithium ion batteries," *Electrochimica Acta*, vol. 54, no. 18, pp. 4403–4407, 2009.
- [27] P. Yan, Z. Huang, Y. Lin et al., "Composite-porous polymer membrane with reduced crystalline for lithium-ion battery via non-solvent evaporate method," *Ionics*, vol. 21, no. 2, pp. 593–599, 2015.
- [28] P. L. Kuo, C. A. Wu, C. Y. Lu, C. H. Tsao, C. H. Hsu, and S. S. Hou, "High performance of transferring lithium ion for polyacrylonitrile-interpenetrating crosslinked polyoxyethylene network as gel polymer electrolyte," *ACS Applied Materials & Interfaces*, vol. 6, no. 5, pp. 3156–3162, 2014.
- [29] S. Li, D. Zhang, X. Meng, Q. A. Huang, C. Sun, and Z. L. Wang, "A flexible lithium-ion battery with quasi-solid gel electrolyte for storing pulsed energy generated by triboelectric nanogenerator," *Energy Storage Materials*, vol. 12, pp. 17–22, 2018.
- [30] L. Long, S. Wang, M. Xiao, and Y. Meng, "Polymer electrolytes for lithium polymer batteries," *Journal of Materials Chemistry A*, vol. 4, no. 26, pp. 10038–10069, 2016.
- [31] T. F. Miller III, Z. G. Wang, G. W. Coates, and N. P. Balsara, "Designing polymer electrolytes for safe and high capacity rechargeable lithium batteries," *Accounts of Chemical Research*, vol. 50, no. 3, pp. 590–593, 2017.
- [32] G. Qiu and C. Sun, "A quasi-solid composite electrolyte with dual salts for dendrite-free lithium metal batteries," *New Journal of Chemistry*, vol. 44, no. 5, pp. 1817–1824, 2020.
- [33] Q. Lu, J. Yang, W. Lu, J. Wang, and Y. Nuli, "Advanced semi-interpenetrating polymer network gel electrolyte for rechargeable lithium batteries," *Electrochimica Acta*, vol. 152, pp. 489–495, 2015.
- [34] Y. Huang, B. Liu, H. Cao et al., "Novel gel polymer electrolyte based on matrix of PMMA modified with polyhedral oligomeric silsesquioxane," *Journal of Solid State Electrochemistry*, vol. 21, no. 8, pp. 2291–2299, 2017.
- [35] D. J. Darensbourg, "Making plastics from carbon dioxide: salen metal complexes as catalysts for the production of polycarbonates from epoxides and CO₂," *Chemical Reviews*, vol. 107, no. 6, pp. 2388–2410, 2007.
- [36] Q. Liu, L. Wu, R. Jackstell, and M. Beller, "Using carbon dioxide as a building block in organic synthesis," *Nature Communications*, vol. 6, no. 1, 2015.
- [37] W. Luo, M. Xiao, S. Wang, D. Han, and Y. Meng, "Gradient terpolymers with long ϵ -caprolactone rich sequence derived from propylene oxide, CO₂, and ϵ -caprolactone catalyzed by zinc glutarate," *European Polymer Journal*, vol. 84, pp. 245–255, 2016.
- [38] S. Inoue, H. Koinuma, and T. Tsuruta, "Copolymerization of carbon dioxide and epoxide with organometallic compounds," *Macromolecular Chemistry and Physics*, vol. 130, no. 1, pp. 210–220, 1969.
- [39] X. Yu, M. Xiao, S. Wang, D. Han, and Y. Meng, "Fabrication and properties of crosslinked poly (propylene carbonate maleate) gel polymer electrolyte for lithium-ion battery," *Journal of Applied Polymer Science*, vol. 118, pp. 2078–2083, 2010.
- [40] J. Zhao, J. Zhang, P. Hu et al., "A sustainable and rigid-flexible coupling cellulose-supported poly (propylene carbonate)

- polymer electrolyte towards 5 V high voltage lithium batteries,” *Electrochimica Acta*, vol. 188, pp. 23–30, 2016.
- [41] D. Zhou, R. Zhou, C. Chen et al., “Non-volatile polymer electrolyte based on poly (propylene carbonate), ionic liquid, and lithium perchlorate for electrochromic devices,” *The Journal of Physical Chemistry B*, vol. 117, no. 25, pp. 7783–7789, 2013.
- [42] X. Huang, D. Xu, W. Chen et al., “Preparation, characterization and properties of poly (propylene carbonate)/poly (methyl methacrylate)-coated polyethylene gel polymer electrolyte for lithium-ion batteries,” *Journal of Electroanalytical Chemistry*, vol. 804, pp. 133–139, 2017.
- [43] X. Huang, S. Zeng, J. Liu et al., “High-performance electrospun poly (vinylidene fluoride)/poly (propylene carbonate) gel polymer electrolyte for lithium-ion batteries,” *The Journal of Physical Chemistry C*, vol. 119, no. 50, pp. 27882–27891, 2015.
- [44] X. Huang, J. Huang, J. Wu et al., “Fabrication and properties of polybutadiene rubber-interpenetrating cross-linking poly (propylene carbonate) network as gel polymer electrolytes for lithium-ion battery,” *RSC Advances*, vol. 5, no. 65, pp. 52978–52984, 2015.
- [45] K. Deng, S. Wang, S. Ren, D. Han, M. Xiao, and Y. Meng, “Network type sp³ boron-based single-ion conducting polymer electrolytes for lithium ion batteries,” *Journal of Power Sources*, vol. 360, pp. 98–105, 2017.
- [46] Y. Zhong, L. Zhong, S. Wang et al., “Ultra-high Li-ion conductive single-ion polymer electrolyte containing fluorinated polysulfonamide for quasi-solid-state Li-ion batteries,” *Journal of Materials Chemistry*, vol. 7, no. 42, pp. 24251–24261, 2019.
- [47] Q. Zhu, Y.?. Z. Meng, S.?. C. Tjong, X.?. S. Zhao, and Y.?. L. Chen, “Thermally stable and high molecular weight poly (propylene carbonate)s from carbon dioxide and propylene oxide,” *Polymer International*, vol. 51, no. 10, pp. 1079–1085, 2002.
- [48] Y. Tominaga, K. Yamazaki, and V. Nanthana, “Effect of anions on lithium ion conduction in poly (ethylene carbonate)-based polymer electrolytes,” *Journal of the Electrochemical Society*, vol. 162, no. 2, pp. A3133–A3136, 2015.
- [49] Y. H. Li, X. L. Wu, J. H. Kim et al., “A novel polymer electrolyte with improved high-temperature-tolerance up to 170 °C for high-temperature lithium-ion batteries,” *Journal of Power Sources*, vol. 244, pp. 234–239, 2013.

Research Article

A Nitrogen-Rich Covalent Triazine Framework as a Photocatalyst for Hydrogen Production

Ruizhi Gong,¹ Liulu Yang,¹ Shuo Qiu,¹ Wan-Ting Chen,² Qing Wang,² Jiazhao Xie,³ Geoffrey I. N. Waterhouse^{1,2,4}  and Jing Xu¹ 

¹College of Chemistry and Material Science, Shandong Agricultural University, Tai'an, Shandong 271018, China

²School of Chemical Sciences, The University of Auckland, Auckland, New Zealand

³College of Resources and Environment, Shandong Agricultural University, Tai'an, Shandong 271018, China

⁴The MacDiarmid Institute for Advanced Materials and Nanotechnology, New Zealand

Correspondence should be addressed to Geoffrey I. N. Waterhouse; g.waterhouse@auckland.ac.nz and Jing Xu; jiaxu@sdau.edu.cn

Received 18 February 2020; Accepted 15 April 2020; Published 7 May 2020

Academic Editor: Yuezhong Meng

Copyright © 2020 Ruizhi Gong et al. This is an open access article distributed under the Creative Commons Attribution License, which permits unrestricted use, distribution, and reproduction in any medium, provided the original work is properly cited.

Covalent triazine frameworks (CTFs) have emerged as new candidate materials in various research areas such as catalysis, gas separation storage, and energy-related organic devices due to their easy functionalization, high thermal and chemical stability, and permanent porosity. Herein, we report the successful synthesis of a CTF rich in cyano groups (CTF-CN) by the solvothermal condensation of 2,3,6,7-tetrabromonaphthalene (TBNDA), Na₂(1,1-dicyanoethene-2,2-dithiolate), and 1,3,5-tris-(4-aminophenyl)-triazine (TAPT) at 120°C. XRD, SEM, and TEM characterization studies revealed CTF-CN to be amorphous and composed of ultrathin 2D sheets. CTF-CN possessed strong absorption at visible wavelengths, with UV-vis measurements suggesting a band gap energy in the range 2.7–2.9 eV. A 5 wt.% Pt/CTF-CN was found to be a promising photocatalyst for hydrogen production, affording a rate of 487.6 μmol g⁻¹ h⁻¹ in a H₂O/TEOA/CH₃OH solution under visible light. The photocatalytic activity of CTF-CN was benchmarked against g-C₃N₄ for meaningful assessment of performance. Importantly, the 5 wt.% Pt/CTF-CN photocatalyst exhibited excellent thermal and photocatalytic stability. Further, as a nitrogen-rich porous 2D material, CTF-CN represents a potential platform for the development of novel electrode material for fuel cells and metal ion batteries.

1. Introduction

Energy production and storage are two of the biggest challenges for the 21st century. There is increasing global demand for environmentally friendly energy sources, with the solar-driven splitting of water into H₂ and O₂ receiving a lot of attention as a potentially sustainable source of H₂ fuel. Over the past decade, interest in the development of visible light-driven photocatalysts for hydrogen production has grown enormously [1–3]. Graphitic carbon nitride (g-C₃N₄), a 2D polymeric material based on heptazine units, has emerged as the front runner in this field owing to its ease of synthesis from a variety of nitrogen-rich organic molecules, its tuneable band gap ($E_g = 2.2\text{--}2.8\text{ eV}$) which can be adjusted by varying the nitrogen level or heteroatom doping, and the favourable locations of its valence and conduction

band levels (+1.57 eV and -1.12 eV, respectively) [4–6]. The position of the valence band maximum allows water oxidation (O₂/H₂O = 0.82 V at pH 7), whilst the position of the conduction band minimum allows proton reduction to H₂ (H₂O/H₂ = -0.41 V at pH 7) [7, 8]. H₂ production rates can be greatly enhanced by the addition of a metal cocatalyst (typically Pt) and a sacrificial hole scavenger (typically methanol or triethanolamine) [9, 10]. A further feature of g-C₃N₄, which distinguishes it from many other visible light-driven photocatalysts, is its excellent stability [11, 12]. Appreciation of the many favourable attributes of g-C₃N₄ has prompted researchers to synthesize molecular analogues, in particular covalent triazine frameworks (CTFs) which are a special subcategory of covalent organic frameworks (COFs) [13]. CTFs exhibit many of the same physical and optical properties as g-C₃N₄, making them particularly attractive synthetic

targets as “molecular” heterogeneous photocatalysts for H₂ production.

Cote and coworkers first demonstrated the utility of topological design principles in connecting molecular building blocks via covalent bonds, thereby creating COFs with large specific surface areas and low density [14]. COFs are now widely applied in gas adsorption, gas storage, fuel cell technology, sensing, heterogeneous catalysis, and photocatalytic applications [15]. Kuhn et al. subsequently pioneered the development of CTFs [13], COFs based primarily on C, H, and N with high thermal stabilities and permanent porosity. CTFs are superior to many traditional porous materials (such as zeolites) in hydrogen storage, gas adsorption, gas separation, and heterogeneous catalysis [16–18]. Triazine rings have similar aromaticity as benzene rings and high electron affinities, along with excellent thermal and chemical stabilities making them especially suitable for catalyst and photocatalyst construction, whilst the presence of nitrogen in triazine results in a modest HOMO-LUMO separation allowing for visible light excitation. Kamiya and coworkers reported that a platinum-modified CTF hybridized with conductive carbon nanoparticles showed excellent activity and selectivity for oxygen reduction reactions in the presence of methanol [19]. Ding et al. reported that a palladium-modified imine-linked COF showed good catalytic activity, stability, and recyclability for Suzuki-Miyaura coupling reactions [20]. Bi et al. examined the photocatalytic performance of a CTF with a graphene-like layered morphology for H₂ production. In the presence of a platinum cocatalyst, a H₂ production rate of $\sim 250 \mu\text{mol g}^{-1} \text{h}^{-1}$ was realized in 12.5 vol% TEOA under $\lambda > 420 \text{ nm}$ excitation. Huang et al. successfully synthesized covalent triazine frameworks with benzothiadiazoles and thiophene moieties as electron-withdrawing and electron-donating units, respectively. A remarkable H₂ evolution rate of $6.6 \text{ mmol g}^{-1} \text{h}^{-1}$ was achieved under visible light irradiation ($\lambda > 420 \text{ nm}$) for one of the CTF hybrids synthesized, with the high activity being rationalized in terms of the improved charge separation that was possible in such hybrid CTF systems. These studies highlight the enormous untapped potential of CTFs as visible light-driven photocatalysts for H₂ production [21]. However, most of the studies reported in the literature relating to CTF development for photocatalytic H₂ production do not include data for an appropriate reference photocatalyst under the same testing conditions [22–24]. This makes it is very difficult to meaningfully compare the activity of CTFs prepared by different research groups in terms of their H₂ production performance [25–27]. More comparative studies are needed, where new CTFs are tested alongside a reliable catalyst standard, such as g-C₃N₄.

A number of studies have shown that the introduction of cyano groups (-C≡N) into g-C₃N₄ photocatalysts can be beneficial for improving the visible light response and photocatalytic activity [28–30]. Cyano groups have strong electron-withdrawing properties and thus promote the efficient separation of photogenerated electrons and holes. Cyano groups also offer a functional group that can easily be modified chemically to impart additional functionality into a molecule or a polymer. To date, the synthesis of CTFs

containing an abundance of cyano groups has received little attention, thus motivating a detailed investigation.

In this work, we aimed to synthesize a novel cyano-containing CTF (denoted herein as CTF-CN) via a facile solvothermal synthesis method. Our approach involved the reaction of 2,3,6,7-tetrabromonaphthalene dianhydride (TBNDA) with Na₂(1,1-dicyanoethene-2,2-dithiolate), followed by the condensation reaction of the organic product of this reaction with 2,4,6-tris(4-aminophenyl)-1,3,5-triazine (TAPT) [31–33]. The reaction scheme and structure of the CTF-CN product is shown in Figure 1. The introduction of the conjugated naphthalene dianhydride units was expected to assist visible light absorption; the TAPT component would impart stability, whilst the dicyano groups would offer sites for postsynthetic modification of the covalent framework. By synergistically combining these attributes, it was anticipated that a CTF material with good photocatalytic activity for visible light-driven hydrogen production could be synthesized [34, 35].

2. Experimental Section

2.1. Materials. 4-Aminobenzonitrile, trifluoromethanesulfonic acid, 2,3,6,7-tetrabromonaphthalene, 1,3,5-tris-(4-aminophenyl)-triazine, carbon disulfide, N,N-dimethylformamide, n-butanol, mesitylene, triethanolamine, and all other chemicals were purchased from Aladdin and used without further purification. For the photocatalytic tests, Milli-Q water (18.2 M Ω -cm) was used.

2.2. Synthesis of 1,3,5-Tris-(4-aminophenyl) Triazine (TAPT). TAPT was synthesized via superacid catalyzed trimerization of 4-aminobenzonitrile. Briefly, 4-aminobenzonitrile (0.386 g) was added to a 25 mL three-neck round bottom flask equipped with a magnetic stirrer and N₂ inlet. Next, the flask was cooled to 0°C in an ice bath, after which 1 mL of trifluoromethanesulfonic acid (11.1 mmol) was added dropwise into the flask over a period of 1 h under magnetic stirring. The solution was then stirred for further 24 h at room temperature resulting in the formation of an orange precipitate. After completion of the reaction, distilled water (10 mL) was added to the mixture under constant stirring, and the mixture neutralized to pH 7 by the addition of 2 mol L⁻¹ NaOH solution. As the pH increased, the orange precipitate dissolved to give a bright orange solution, with a pale yellow precipitate forming as the pH approached 7. The resultant pale yellow product was collected by filtration and then washed repeatedly with distilled water. The crude product was dried at 80°C under vacuum for 12 h, then purified by recrystallization in N-methylpyrrolidone (NMP). The recrystallized yellow TAPT product was dried overnight at 100°C. The purity of the TAPT product (yield 78.6%) was confirmed by elemental analysis and ¹H NMR spectroscopy.

2.3. Synthesis of Na₂(1,1-dicyanoethene-2,2-dithiolate) (Na₂(i-mnt)). Malononitrile (66 g, 1 mol) was slowly added to a stirred solution of sodium hydroxide (80 g) in ethanol (900 mL), with the temperature of the solution being maintained at 10°C. Next, carbon disulfide (76 g, 1 mol) was added dropwise over a period of 30 min, with the resulting pale

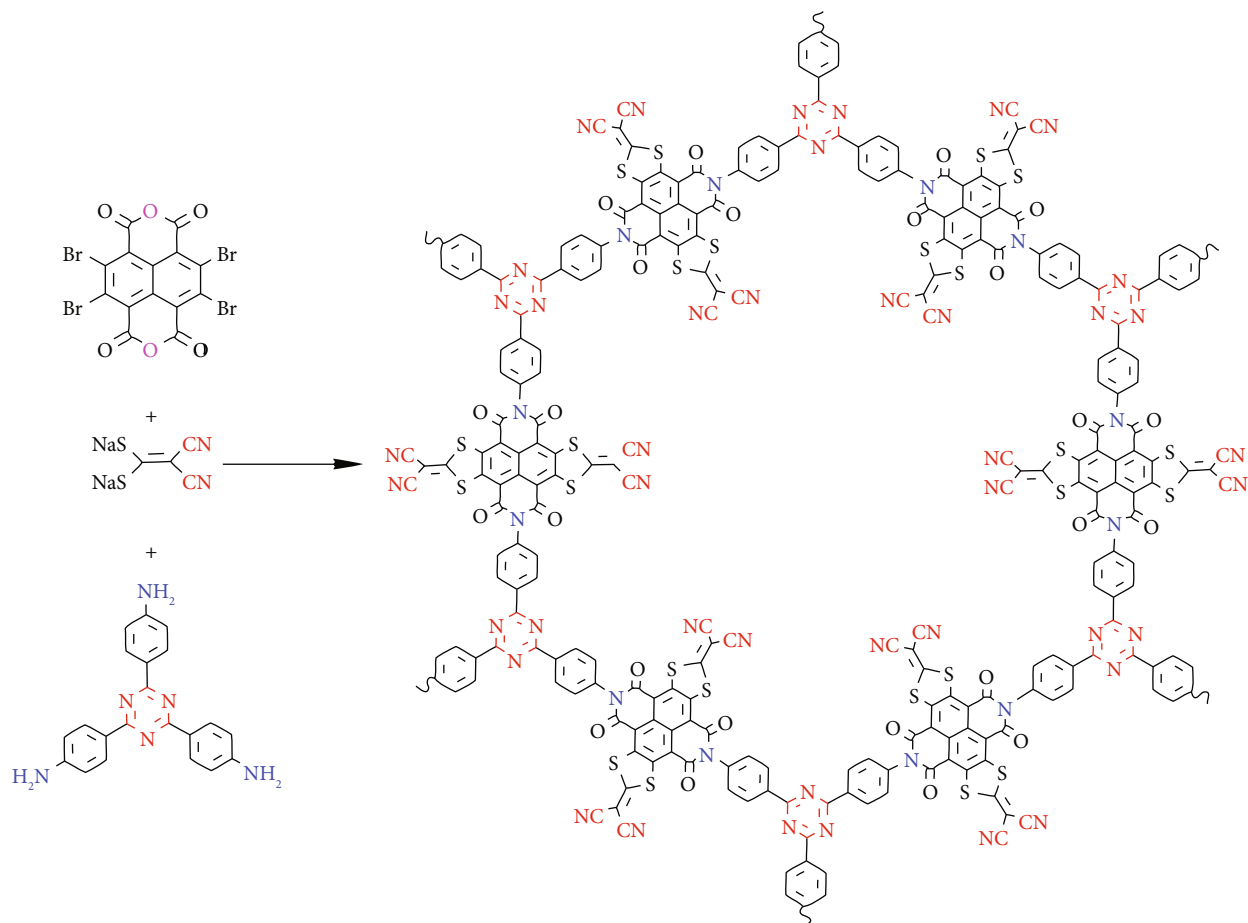


FIGURE 1: Scheme outlining the synthesis of CTF-CN.

yellow slurry then stirred for 1 h at room temperature. The product was collected by filtration, washed repeatedly with ethanol, and then dried at 80°C in a vacuum oven for 24 h. After drying, the product has a light brown colour and was mildly hygroscopic.

2.4. Synthesis of the Covalent Triazine Framework with Cyano Groups (CTF-CN). A 10 mL pyrex tube with a screw cap was charged with 2,3,6,7-tetrabromonaphthalene (70 mg, 0.12 mmol) and $\text{Na}_2(\text{i-mnt})$ (44.8 mg, 0.241 mmol). To that mixture, n-butanol (3.91 mL) and mesitylene (1.31 mL) were added. The resulting mixture was then sonicated for 10 min to homogeneously disperse all the reactants. Next, the mixture was heated in an oil bath at 50°C for 1 h, after which 1,3,5-tris-(4-aminophenyl)-triazine (28 mg, 0.079 mmol) was added. The pyrex tube was then capped, and the reaction mixture was heated at 120°C for five days. The molar ratios of TBNDAs, $\text{Na}_2(\text{i-mnt})$, and TAPT used in the synthesis were 1.5:3:1. The obtained black product was collected by filtration and washed with THF and acetone three times. The product (CTF-CN) was purified in a Soxhlet apparatus with MeOH and then dried under vacuum at 120°C for 12 h. The yield was ~90%.

2.5. Synthesis of the Graphitic Carbon Nitride ($g\text{-C}_3\text{N}_4$) Reference Photocatalyst. A $g\text{-C}_3\text{N}_4$ reference photocatalyst

was prepared by the thermal polymerization of urea. Briefly, urea (30 g) was loaded into a 100 mL alumina crucible, covered with a lid, and then heated in a muffle furnace from room temperature to 550°C in air at a heating rate of 2°C min⁻¹. The crucible was held at 550°C for 4 h, then kept in the furnace and allowed to cool naturally to room temperature overnight. A yellow product was obtained.

2.6. Characterization. Elemental analyses on TAPT, TBNDAs, $\text{Na}_2(\text{i-mnt})$, CTF-CN, and $g\text{-C}_3\text{N}_4$ were performed at the Campbell Microanalytical Lab (University of Otago, New Zealand). Attenuated total reflectance infrared (ATR-IR) spectra were recorded on an ALPHA FT-IR spectrometer over the 400-4000 cm⁻¹ range. 32 scans at 4 cm⁻¹ resolution were coadded to produce a spectrum. Powder X-ray diffraction (PXRD) patterns were collected on a Bruker AXS D-8 Advanced SWAX diffractometer equipped with a Cu-K α source (0.15406 nm, 40 kV, 300 mA). The scan rate was of 0.02° s⁻¹. ¹H nuclear magnetic resonance (NMR) spectra were recorded on a 400 MHz spectrometer (Bruker Ascend 400 MHz NMR spectrometer). Samples were dissolved in deuterated DMSO for the analyses. Thermogravimetric analyses (TGA) were performed on a Linser T6/DTA thermoanalyzer instrument. Samples were heated at 10°C min⁻¹ under a nitrogen gas flow. Scanning electron microscopy (SEM) images were recorded on a high-resolution scanning electron

microscope (Philips XL-30S Field Emission Gun scanning electron microscope). High-resolution transmission electron microscopy (HR-TEM) images were collected on a JEOL JEM 2010 transmission electron microscope operated at an electron accelerating voltage 200 kV. Samples were dispersed in absolute ethanol; then, 1 μ L of the resulting dispersion transferred onto a holey carbon-coated copper TEM grid for analysis. UV-visible diffuse reflectance spectra were recorded on a UV 2410PC spectrometer equipped with an integrating sphere attachment. Fluorescence spectra were recorded on a RF-5301 PC spectrofluorophotometer (Shimadzu) with 1.0 cm path length cell. X-ray photoelectron spectroscopy (XPS) data were collected on a Thermo ESCALAB 250 equipped with an Al K α X-ray source ($h\nu = 1486.7$ eV). N₂ physisorption data was collected at 77 K on a Tristar 2020 instrument. Specific surface areas were calculated from N₂ adsorption data in the p/p_0 range 0.01-0.1 by the Brunauer-Emmett-Teller (BET) method.

2.7. Photocatalytic Hydrogen Production Tests. Photocatalytic H₂ production tests used a GEL-SPH2N photocatalytic activity evaluation system. Briefly, CTF-CN or g-C₃N₄ (25 mg) was dispersed in a H₂O:TEOA:CH₃OH solution (50 mL) with a volume ratio 85:10:5. To this dispersion, a certain amount of K₂PtCl₆·6H₂O was added (sufficient to achieve a Pt loading of 5 wt.%); then, the headspace of the reactor system purged with N₂ for 1 h under constant stirring. Next, the system was irradiated using a 300 W xenon lamp with a cut-off filter ($\lambda > 420$ nm), which resulted in the photocatalytic reduction of cationic Pt species to Pt⁰. H₂ evolved during the Xe lamp irradiation was quantified by gas chromatography. An autosampler removed a small portion of the headspace gas every 30 min, which was then directly injected into a Shimadzu GC 2014 equipped with a TCD detector and Carboxen-1010 plot capillary column ($L \times I.D. = 30$ m \times 0.53 mm, average thickness 30 μ m). H₂ evolution was quantified against an external calibration curve of peak area versus moles of H₂. Photocatalytic tests for each sample were carried out in triplicate.

3. Results and Discussion

3.1. Characterization of CTF-CN and the g-C₃N₄ Reference Photocatalyst. The chemical composition of the covalent triazine framework with cyano groups (CTF-CN) was first examined by bulk elemental analysis. From Figure 1, it can be shown that the repeat unit for the polymeric compound has the chemical formula C₅₄H₁₂O₆N₁₂S₆. The theoretical weight percentage for each element in the CTF-CN product is therefore C, 58.06 wt.%; H, 1.08 wt.%; O, 8.59 wt.%; N, 15.05 wt.%; and S, 17.22 wt.%. Elemental analysis revealed the following composition: C, 54.21 wt.%; H, 1.18 wt.%; O, 10.70 wt.%; N, 14.05 wt.%; S, 16.06 wt.%; Br, 3.01 wt.%; and Na, 0.78 wt.%. The results confirmed that CTF-CN was relatively pure with the correct chemical formula C₅₄H₁₂O₆N₁₂S₆, along with ~0.4 equivalents of NaBr and 1 equivalent of H₂O. Given that the CTF-CN synthesis was effectively a one pot reaction, this is a very acceptable product purity. ¹H NMR spectroscopy confirmed that the triazine units

derived from TAPT had been successfully incorporated into the CTF-CN product (Figure S1) with the expected loss of the amino (-NH₂) group protons of TAPT through condensation reactions with the central anhydride oxygen of TBNDA. The g-C₃N₄ reference photocatalyst had the elemental composition C, 34.98 wt.%; H, 1.52 wt.%; N, 59.0 wt.%; and O, 4.5 wt.%, corresponding to a carbon normalized molecular formula of C_{3.00}N_{4.34}H_{1.55}O_{0.29}, which is typical for g-C₃N₄ compounds prepared from urea [3–6]. The data suggests that a g-C₃N₄ product is nitrogen-rich, with a significant fraction of the nitrogen having been protonated (as =NH-, -NH₂, or -NH₃⁺) and a small amount of surface oxygen present as H₂O, -OH, or -CO₂H species. Energy-dispersive X-ray spectroscopy, FT-IR, and XPS analyses discussed below provided further chemical composition information about the CTF-CN and g-C₃N₄ products.

FT-IR spectra for CTF-CN, the building blocks of CTF-CN, and the g-C₃N₄ reference photocatalyst are shown in Figure 2(a). TBNDA was characterized by two intense C=O stretching modes at 1784 and 1730 cm⁻¹, associated with the dianhydride groups in the molecule. Bands below 650 cm⁻¹ are associated with C-Br stretching and bending vibrations in the molecule. Na₂(i-mnt) showed a C \equiv N stretching mode at 2173 cm⁻¹ and an intense Na-S stretching mode ~497 cm⁻¹. The peaks seen in the 3200-3450 cm⁻¹ region are O-H stretching modes of water of crystallization. The FT-IR spectrum of TAPT was characterized by peaks at 3318 and 3205 cm⁻¹, which could readily be assigned to the two N-H stretching modes of the -NH₂ groups in the molecule [36]. An in-plane bending vibration for the primary amine groups is also seen at 1617 cm⁻¹. Other bands at 1604 and 1364 cm⁻¹ seen in the FT-IR spectrum of TAPT are associated with molecular vibrations of the triazine ring. The triazine ring vibrations were also present in the FT-IR spectrum of CTF-CN. However, conspicuously absent in the spectrum of CTF-CN were the primary amine vibrations characteristic of TAPT, implying that these groups were removed by reaction on forming CTF-CN. The absence of the intense dianhydride C=O vibrations of TBNDA in the spectrum of the CTF-CN is consistent with the mechanism proposed in Figure 1, where the -NH₂ groups of TAPT react with the dianhydride groups of TBNDA in forming the CTF-CN molecular polymer. New C=O stretching modes appear in the region 1640-1680 cm⁻¹ for CTF-CN, consistent with the formation of imide moieties. The presence of the band at 2215 cm⁻¹ indicates that cyano groups were successfully incorporated into the CTF-CN polymer through reaction between the Na₂(i-mnt) and TBNDA units. The FT-IR spectrum of CTF-CN is thus in good accord with the structure depicted in Figure 1 for the polymer. The FT-IR spectrum of the g-C₃N₄ reference photocatalyst was in good accord with prior literature reports, showing molecular vibrations associated with the heptazine units in the polymeric compound.

Powder X-ray diffraction data for CTF-CN, the chemical building blocks used in the synthesis of CTF-CN, and the g-C₃N₄ reference photocatalyst are shown in Figure 2(b). The TBNDA, Na₂(i-mnt), and TAPT building blocks were all crystalline solids, whereas the CTF-CN product was

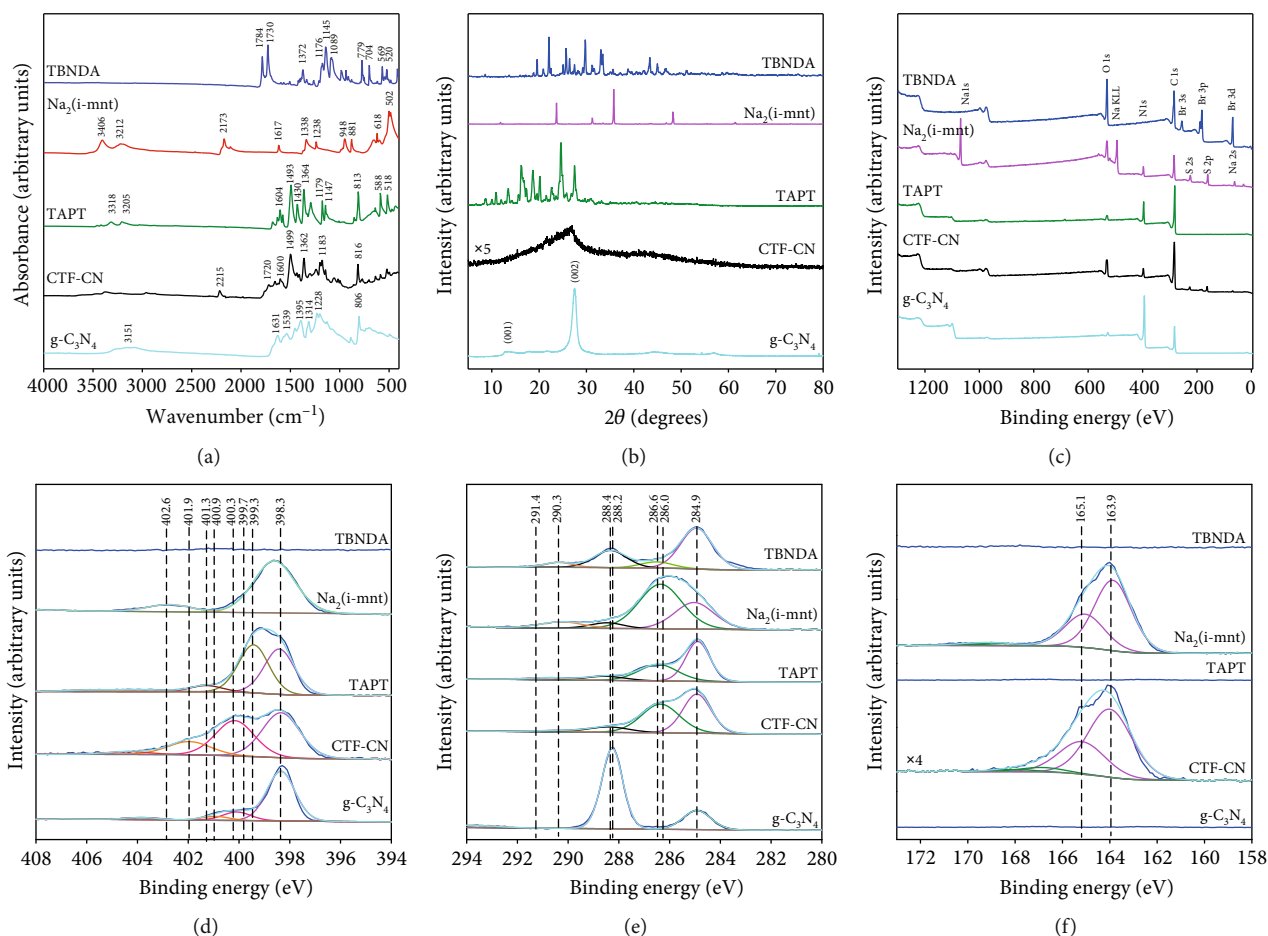


FIGURE 2: (a) FT-IR absorbance spectra for CTF-CN, the starting materials used in the synthesis of CTF-CN, and the g-C₃N₄ reference photocatalyst; (b) powder X-ray diffraction patterns for CTF-CN, the starting materials used in the synthesis of CTF-CN, and the g-C₃N₄ reference photocatalyst; (c–f) XPS data for CTF-CN, the g-C₃N₄ photocatalyst, and various reference compounds: (c) survey spectra; (d) N 1s region; (e) C 1s region; (f) S 2p region.

amorphous, characterized by a broad XRD feature with a maximum around $2\theta = 26^\circ$, which is tentatively attributed to π - π interactions between two dimensional polymeric chains. The lack of crystallinity in CTF-CN was supported by the absence of lattice fringes in the TEM images of Figures 3(c) and 3(d). The fact that CTF-CN was not crystalline is not surprising, since the structure of the framework (Figure 1) allows considerable rotation around the C-C bonds in the TAPT-derived component (i.e., the bonds between the triazine rings and aromatic rings). The g-C₃N₄ reference photocatalyst showed characteristic XRD peaks at $2\theta = 12.8^\circ$ and 27.3° which could readily be assigned to the (001) and (002) reflections, respectively, of crystalline multi-layered g-C₃N₄.

X-ray photoelectron spectroscopy was applied to probe the near-surface region chemical composition of CTF-CN, the building blocks of CTF-CN, and the g-C₃N₄ reference photocatalyst, as well as to examine the nitrogen speciation in these materials. XPS survey spectra for the different samples are shown in Figures 2(c)–2(f). Near-surface region chemical compositions for each sample are summarized in Table S1. The near-surface region chemical compositions for most of

the materials differed from their bulk composition due to the adsorption of adventitious hydrocarbons (C_xH_yO_z), which resulted in an overestimation of the carbon and oxygen contents in the samples (XPS does not detect H). For TBNDA, the O:Br ratio was 3:2, in good agreement with theory. For Na₂(i-mnt), the Na:S:N ratio was ~1:1:1, again in good agreement with expectations. For CTF-CN, the N:S ratio was 2:1, in good accord with the bulk elemental analysis results. The presence of some surface Br was also found by XPS for CTF-CN, which was also in accord with the bulk elemental analysis results (likely present as a minor NaBr impurity or simply adsorbed bromide ions). High-resolution narrow scans were also collected over the N 1s, C 1s, and S 2p regions of the samples (Figures 2(d)–2(f), respectively). The N 1s spectrum of CTF-CN was deconvoluted into 3 components with binding energies of 398.3, 400.3, and 401.9 eV. By comparison with previous XPS literature for covalent triazine frameworks and related N-heterocyclic compounds (Table S2) [37, 38], these peaks can readily be assigned to pyridinic (C=N=C), imidic (C-N-C=O), and cyano (-C≡N) groups, respectively. Based on the structure shown in Figure 1 for CTF-CN, the area ratio of the 398.3:

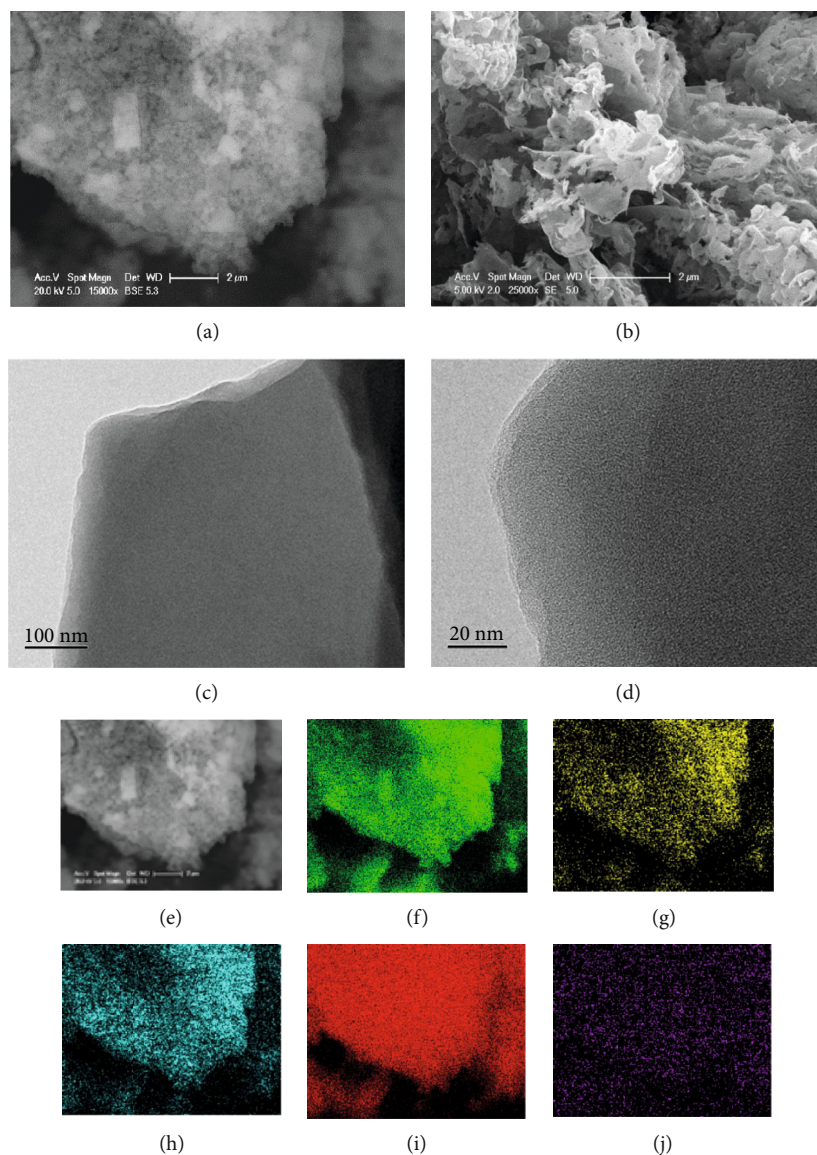


FIGURE 3: (a) SEM image of CTF-CN, (b) SEM image of g-C₃N₄ and (c, d) TEM images of CTF-CN and (e) secondary electron image and (f-j) energy-dispersive spectroscopy element maps for CTF-CN. Elements mapped were (f) C, (g) N, (h) O, (i) S, and (j) Br.

400.4 : 401.9 eV peaks should be 1 : 1 : 2. The experimental area ratio determined from Figure 2(d) was 1 : 1 : 0.5, implying that the near-surface region concentration of cyano groups was ~25% of the theoretical value. This can easily be rationalized by taking into account the susceptibility of cyano groups to hydrolysis, resulting in the production of surface amide or even carboxyl moieties (i.e., $\text{-C}\equiv\text{N} + \text{H}_2\text{O} \longrightarrow \text{C}[\text{O}]\text{-NH}_2$, then $\text{C}[\text{O}]\text{-NH}_2 + \text{H}_2\text{O} \longrightarrow \text{C}[\text{O}]\text{-OH} + \text{NH}_3$). The C 1s spectrum of CTF-CN contained components at 284.9, 286.0, and 288.4 eV, which can be assigned to carbon in aromatic rings/adventitious hydrocarbons (i.e., aromatic sp^2 and sp^3 carbons), C-N/-C \equiv N/C-S species (all of which have similar binding energies), and N-C=N or N-C=O species, respectively (Table S3) [38]. The S 2p spectrum of CTF-CN showed two peaks at 163.9 and 165.1 eV in a 2 : 1 area ratio (S 2p_{3/2} and S 2p_{1/2}, respectively), with identical peaks being observed in the S 2p spectrum of the Na₂(i-mnt) starting

material. The observation of these peaks in the S 2p spectrum of CTF-CN provides further experimental evidence for the successful attachment of the i-mnt groups onto the TBNDA units in the framework. Taking into account the surface reactivity of the cyano groups and the adsorption of adventitious hydrocarbons, it can be concluded that the XPS data collected for CTF-CN was in reasonable accord with expectations. The N 1s spectrum of the g-C₃N₄ reference photocatalyst showed peaks at 398.3 eV and 400.0 eV, which can easily be assigned to C-N=C and C-NH-C species [39]. Further weaker peaks at 400.9 and 403.6 eV are assigned to graphitic N and $\pi \longrightarrow \pi^*$ transitions, respectively. The C 1s spectrum of g-C₃N₄ was dominated by an intense peak at 288.2 eV which can readily be assigned to N-C=N species in the heptazine units of g-C₃N₄. The peak at 284.9 eV is due to adventitious hydrocarbons, whilst $\pi \longrightarrow \pi^*$ transitions give rise to weak features around 293-294 eV.

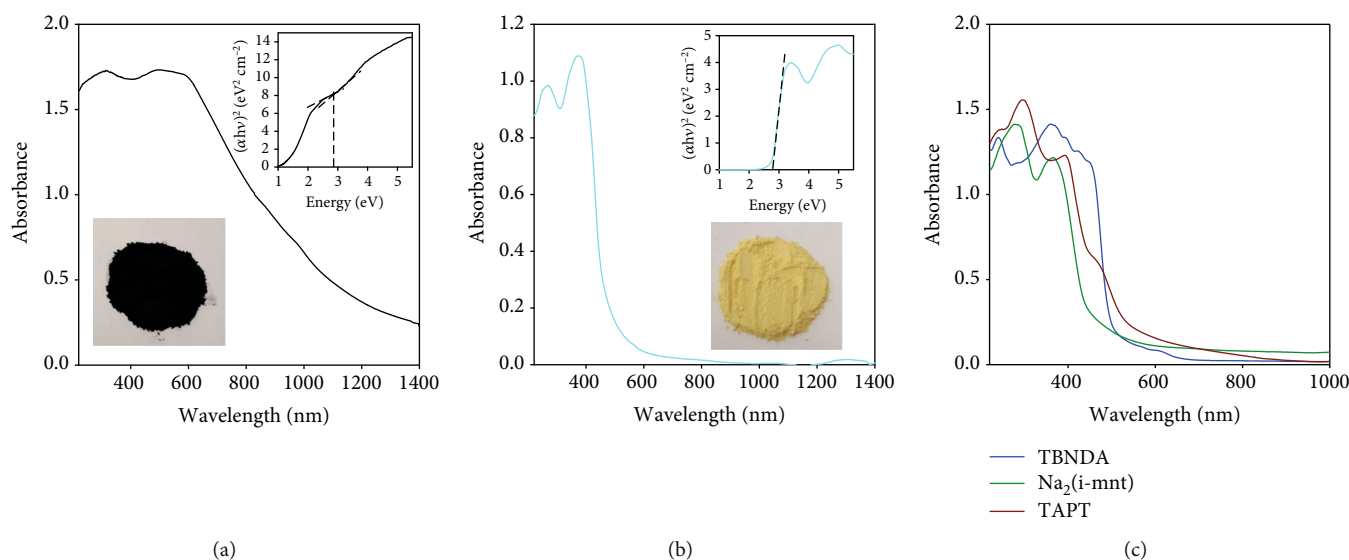


FIGURE 4: UV-vis absorbance spectra, Tauc plots, and digital photographs for (a) CTF-CN and (b) the g-C₃N₄ reference photocatalyst. For the Tauc analyses, it was assumed that both CTF-CN and g-C₃N₄ are direct band gap semiconductors. (c) Comparison of the UV-vis absorbance spectra for TBNDA, Na₂(i-mnt), and TAPT.

Scanning electron microscopy (SEM) and transmission electron microscopy (TEM) were applied to examine the morphologies of the CTF-CN and g-C₃N₄ products (Figures 3(a) and 3(b)). The as-prepared CTF-CN sample was found to consist of thin 2D sheets, with the sheets having a small lateral size and haphazardly assembled into 3D bundles (Figure 3(a)). These bundles could quite easily be broken up by ultrasonication, with TEM analysis revealing the CTF-CN sheets to be very thin, suggesting that they possessed some form of loosely layered structure to achieve thicknesses of a few nanometers. The g-C₃N₄ reference photocatalyst similarly had a characteristic 2D sheet-like structure, with the lateral size of the g-C₃N₄ sheets being at least one order of magnitude larger than the CTF-CN nanosheets.

Energy-dispersive spectroscopy (EDS) was subsequently applied to examine the element dispersion in CTF-CN. As shown in Figures 3(e)–3(j), the sample showed a uniform distribution of C, N, O, and S, with trace amounts of Br also found. Quantitative EDS analysis revealed that the ratios of these elements were consistent with the molecular formula determined from the bulk elemental analysis (i.e., C₅₄H₁₂O₆N₁₂S₆ with a small amount of Na, Br, and O).

Surface area and porosity are important considerations when developing photocatalytic materials. N₂ physisorption data was collected at 77 K for both CTF-CN and g-C₃N₄. Nitrogen adsorption-desorption isotherms collected for CTF-CN are shown in Figure S2. The CTF-CN sample showed a type II adsorption isotherm under the IUPAC classification system. The BET specific surface area was determined to be 96 m² g⁻¹, which was low compared to areas reported for other crystalline CTF materials. It can therefore be concluded that CTF-CN does not possess an ordered microporous or ordered mesoporous structure, consistent with the XRD analysis which showed the material to be amorphous. A further possible reason for the

modest specific surface may be blocking of pores by the abundant cyano groups in the CTF-CN structure. The BET specific surface area for the g-C₃N₄ reference photocatalyst was 108.3 m² g⁻¹. The similarity in surface area between CTF-CN and g-C₃N₄ was desirable here, as it meant that both samples would offer almost the same amount of surface for light absorption and surface redox reactions during the photocatalytic tests.

UV-vis transmittance spectra and Tauc plots for CTF-CN and g-C₃N₄ are shown in Figures 4(a) and 4(b). CTF-CN was black, absorbing very strongly across the whole visible spectrum. Such a wide absorption range was not surprising, given the fact the polymer contained multiple chromophores with accessible $\pi \rightarrow \pi^*$ and $n \rightarrow \pi^*$ transitions (the absorption spectra for the TBNDA, Na₂(i-mnt), and TAPT are shown in Figure 4(c) for comparison). The g-C₃N₄ reference photocatalyst had a characteristic absorption edge ~450 nm and an absorption tail extending to longer wavelengths associated with nitrogen defects. Band gap energies extrapolated from the Tauc plots for CTF-CN and g-C₃N₄ were ~2.8 eV (due to the many different chromophores in the CTF-CN polymer, exact determination of E_g was challenging) and 2.7 eV, respectively. It is likely that the E_g value needed to drive the H₂ production reactions using CTF-CN is probably similar to that of g-C₃N₄ (i.e., ~2.7–2.8 eV). This implies that the separation between the CB and the VB (or alternatively the separation between S₁ and S₀ states) was very similar in the two materials.

For many applications involving covalent triazine frameworks, thermal stability is important. Figure S3 shows thermogravimetric (TGA) data for TBNDA, Na₂(i-mnt), TAPT, and CTF-CN collected with heating under a N₂ atmosphere. Except for Na₂(i-mnt), which showed a large mass loss below 100°C due to the loss of water of crystallization (3 equivalents of H₂O per Na₂(i-mnt)), all

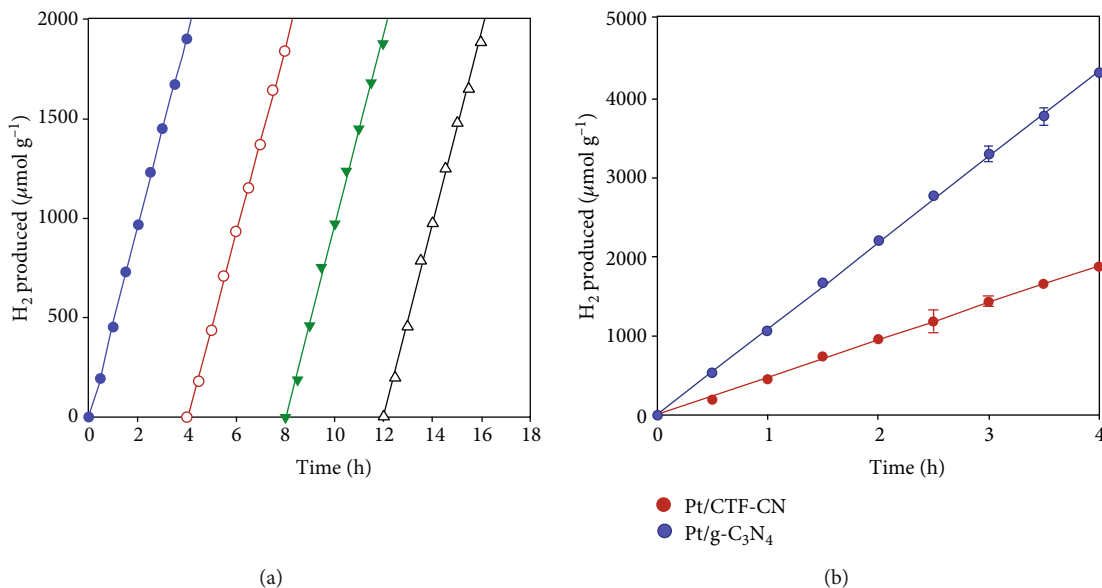


FIGURE 5: (a) H₂ production data for Pt/CTF-CN over four successive testing cycles in a H₂O/TEOA/CH₃OH (85 : 10 : 5 by volume) mixture under irradiation from a 300 W Xenon lamp and (b) plots of H₂ production versus time for Pt/CTF-CN and the Pt/g-C₃N₄ reference photocatalyst.

samples were stable to temperatures above 300°C. It can be concluded that CTF-CN is thermally very stable.

3.2. Photocatalytic Hydrogen Production Tests. Following the detailed physicochemical characterization studies of CTF-CN and g-C₃N₄ described above, we then focussed on evaluating the photocatalytic hydrogen production performance of these two materials in aqueous media. In a typical experiment, CTF-CN or g-C₃N₄ (25 mg) was dispersed in 50 mL of a H₂O:TEOA:CH₃OH mixture (containing 10 vol% TEOA and 5 vol% CH₃OH). The H₂O:TEOA:CH₃OH solution contained sufficient K₂PtCl₆·6H₂O to achieve a Pt metal loading of 5 wt.% once all the dissolved platinum salt had been reduced. The catalyst dispersions were stirred in the dark under a N₂ flow for 1 h to remove any dissolved oxygen, then irradiated by a 300 W Newport Xe light source with a 420 nm cutoff filter. This resulted in the simultaneous formation of Pt metal nanoparticles on the surface of the catalysts (see characterization data below) and concurrent H₂ evolution.

Figure 5(a) shows plots of H₂ production over time for the Pt/CTF-CN photocatalyst. The photocatalytic H₂ production test was carried out over a 4 h period, affording a H₂ production rate of 484.7 μmol g⁻¹ h⁻¹ for run #1 (see Table S4). The reactor was then shielded from the Xe lamp and purged with N₂ for 15 min, then again irradiated with the Xe lamp for 4 h. The H₂ production rate for run #2 was 468.4 μmol g⁻¹ h⁻¹ and 481.3 and 479.9 μmol g⁻¹ h⁻¹ for the two subsequent runs (i.e., runs #3 and #4). It can therefore be concluded that the Pt/CTF-CN photocatalyst was extremely stable under the applied testing conditions, with no loss in activity observed over a 16 h testing period. Figure 5(b) compares the performance of the Pt/CTF-CN and Pt/g-C₃N₄ photocatalysts over the 4 repeat test cycles (the Pt/g-C₃N₄ photocatalyst also showed no change in

activity over the 4 cycles). The hydrogen production rate over the Pt/g-C₃N₄ photocatalyst was 1088 μmol g⁻¹ h⁻¹ or approximately twice that of Pt/CTF-CN when the rates were normalized by the specific surface area (10.054 μmol m⁻² h⁻¹ for Pt/g-C₃N₄ versus 4.985 μmol m⁻² h⁻¹ for Pt/CTF-CN). Benchmarking using the g-C₃N₄ reference photocatalyst, which is relatively easy to synthesize, provides a useful indicator of the merits of the Pt/CTF-CN photocatalyst for H₂ production. With optimization of parameters such as metal cocatalyst loading and Pt/CTF-CN dispersion, it is likely that the performance of the Pt/CTF-CN could be improved to the level of the 5 wt.% Pt/g-C₃N₄ photocatalyst. Table S5 compares the performance of the Pt/CTF-CN photocatalyst for H₂ production with various other covalent triazine framework photocatalysts and CTF hybrid photocatalysts. The data shows that the H₂ production activity of Pt/CTF-CN photocatalyst sits in the middle of the range of reported values for CTF-based photocatalysts. Again, we urge caution in comparing the activity of Pt/CTF-CN with the other systems, due to differences in cocatalyst loading content, sacrificial agent, presence/absence of cyano groups, and various other parameters which can all influence H₂ production rates as shown in Figure S4. However, it should be noted that under the same experimental conditions, the hydrogen production rate of Pt/CTF-CN was nearly four times that of Pt/CTF (without cyano groups), indicating that the presence of cyano groups can promote the efficient separation of photogenerated electrons and holes in covalent triazine frameworks.

Here, we strongly advocate that researchers in the field test a Pt/g-C₃N₄ photocatalyst alongside their Pt/CTF or Pt/CTF-CN photocatalysts to allow meaningful comparison of the work of different groups (measurement of apparent quantum yields is an alternative approach that allows the work of different groups to be compared, though in our

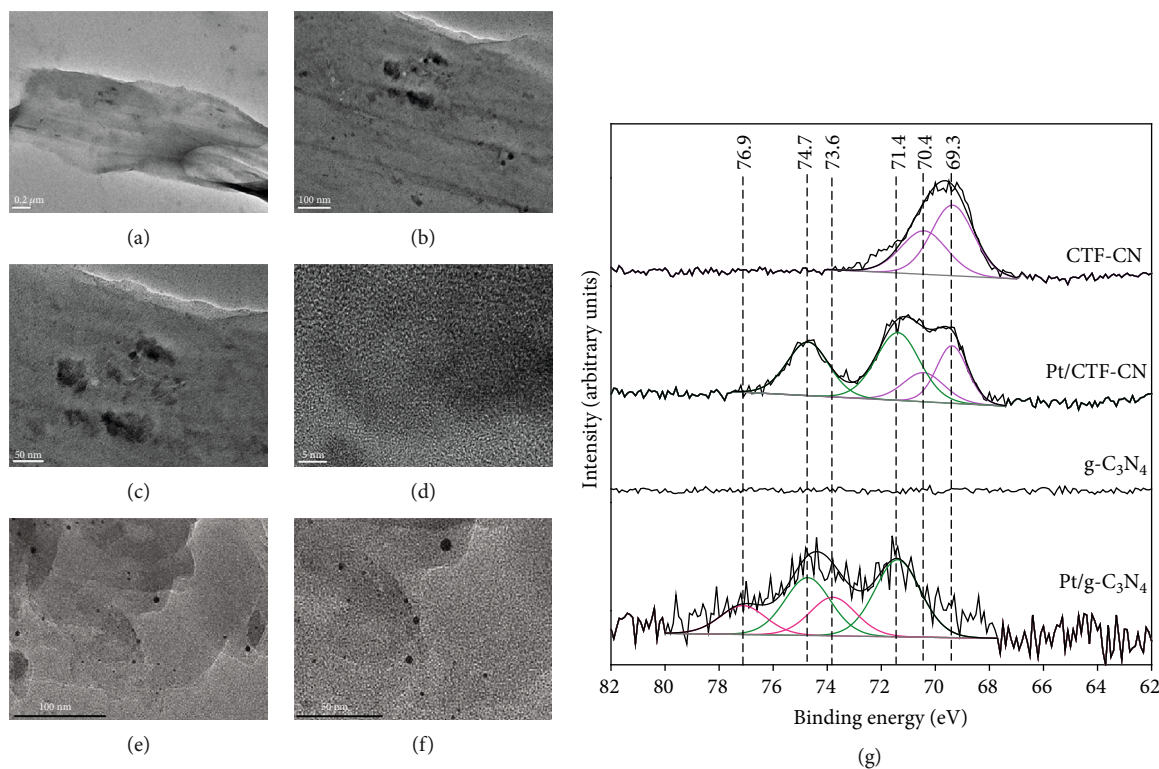


FIGURE 6: TEM images for (a–d) Pt/CTF-CN following the H_2 production tests and (e, f) Pt/g- C_3N_4 . The Pt nanoparticles were formed by the photoreduction of hexachloroplatinate ions in a $\text{H}_2\text{O}/\text{TEOA}/\text{CH}_3\text{OH}$ (85 : 10 : 5 by volume) mixture with photocatalyst exposure to a 300 W Xe lamp. (g) Pt 4f XPS spectra for CTF-CN, Pt/CTF-CN, g- C_3N_4 , and Pt/g- C_3N_4 . For the CTF-CN and Pt/CTF-CN, the Br 3d peaks also appear in this spectral region (for the curve fits, pink = Br 3d, green = Pt^0 , and red = Pt^{2+}).

experience is less straightforward than just measuring a simple reference catalyst under the same testing conditions). For the interest of readers, Table S6 compares the activity of our Pt/g- C_3N_4 photocatalyst for H_2 production with prior literature reports for Pt/g- C_3N_4 systems.

Regarding the role of the Pt cocatalyst, negligible H_2 production was observed from CTF-CN or g- C_3N_4 in the absence of $\text{K}_2\text{PtCl}_6 \cdot 6\text{H}_2\text{O}$ addition. Clearly, the surfaces of these materials have high overpotentials for H_2 evolution. $\text{K}_2\text{PtCl}_6 \cdot 6\text{H}_2\text{O}$ was therefore added to the system to produce the Pt^0 nanoparticles by photoreduction. When the Xe lamp irradiates the photocatalyst dispersion containing Pt(II) ions, photogenerated electrons are easily transferred from the photocatalyst to surface-adsorbed Pt(II) ions, resulting in the reduction of Pt(II) to Pt^0 . Pt nanoparticles created on the photocatalyst surface then act as efficient hydrogen evolution sites since platinum has a high work function ($\Phi = 5.65$ eV) and a low Fermi level (i.e., a Schottky junction is formed between the photocatalyst and Pt). As a result, electrons photogenerated in the photocatalyst migrate onto the Pt nanoparticles, providing cathodic sites for H_2 generation and suppressing electron-hole pair recombination. Electron-hole pair recombination was further suppressed here by using triethanolamine (TEOA) and methanol as sacrificial hole scavengers (electron donors). Figures 6(a)–6(d) show TEM images for the Pt/CTF-CN photocatalyst after the four successive cycles of H_2 production tests depicted in

Figure 5(a). Following, the tests, Pt nanoparticles can be seen on the surface of the CTF-CN photocatalyst, ranging in size from 1 to 10 nm. In addition, some lattice fringes can be seen in high-resolution images (Figure 6(d)), which may be due to Pt nanoparticles or possibly due to partial crystallization of the CTF-CN during the photoreaction. For the Pt/g- C_3N_4 photocatalyst, which offered a larger atomic number contrast between Pt and the support, the Pt nanoparticles were easier to discern, having sizes ranging from 1 to 8 nm (Figures 6(e)–6(f)). ICP-MS confirmed that the Pt/CTF-CN and Pt/g- C_3N_4 photocatalysts had Pt loadings in the range 4.6–4.8 wt.%, in good accord with the nominal target loading of 5 wt.%. Pt 4f XPS spectra for the Pt/CTF-CN and Pt/g- C_3N_4 photocatalysts are shown in Figure 6(g). For the Pt/CTF-CN photocatalyst, the Pt 4f spectrum showed peaks at 71.4 and 76.9 eV in a 4 : 3 area ratio, which can readily be assigned to the Pt 4f_{7/2} and 4f_{5/2} signals of platinum metal (peaks at 69.3 and 70.4 eV in a 3 : 2 area ratio are Br 3d_{5/2} and Br 3d_{3/2} peaks, respectively, of a surface bromide impurity). For Pt/g- C_3N_4 , two sets of Pt peaks are seen; the peaks at 71.2 and 76.7 eV are due to Pt^0 , whereas the peaks at 73.6 and 76.9 eV are due to Pt(II). The TEM and XPS data for Pt/CTF-CN and Pt/g- C_3N_4 thus confirm the in situ reduction of Pt(II) ions to Pt^0 on the surface of the photocatalysts under the conditions of the H_2 production tests. FT-IR spectra for CTF-CN and Pt/CTF-CN (after 16 h of H_2 production testing) are shown in Figure S5. Following the tests, new peaks appear at 3270

and 1036 cm^{-1} , consistent with the introduction of surface C-O-H groups. The introduction of these groups does not appear to adversely impact the photocatalytic activity of Pt/CTF-CN, since the H_2 production rate did not change over the 16 h of testing (Table S4). Currently, we are performing apparent quantum yield experiments using narrow band pass filters on Pt/CTF-CN to explore the relationship between the CTF-CN electronic structure and photocatalytic H_2 performance.

3.3. Alternative Microwave-Assisted Synthesis of CTF-CN. Finally, we explored an alternative microwave-based synthesis of CTF-CN. It was hypothesized that by using microwave heating, the kinetics of CTF-CN synthesis could be enhanced, as has been observed by other groups [40, 41]. Under a nitrogen atmosphere, TBND and $\text{Na}_2(\text{i-mnt})$ were added to a round bottomed three-necked flask, with DMF added as the solvent. The flask was then heated at 50°C for 1 h in an oil bath, after which TAPT was added to suspension. Next, the mixture was transferred to a microwave reactor, then subjected to 300 W microwave irradiation for 30 min. The reaction temperature achieved was $\sim 70^\circ\text{C}$. Following the treatment, the contents of the microwave reactor were poured into ice-cold ethanol, then centrifuged to obtain the CTF-CN product. The microwave-synthesis method had a low yield ($\sim 10\%$ due to the relatively short reaction time, compare 90% for the solvothermal synthesis over 5 d), though giving a CTF-CN polymer with a much more uniform sheet-like structure than the solvothermal method (i.e., a structure more comparable to $\text{g-C}_3\text{N}_4$), as shown in Figure S6. Currently, we are evaluating the performance of the microwave-assisted synthesized CTF-CN for photocatalytic hydrogen production. We are also exploring microwave-assisted synthetic approaches for postsynthetic modification of CTF-CN by taking advantage of the reactivity of the cyano groups in the polymer.

4. Conclusion

A novel covalent triazine framework functionalized with numerous cyano groups was successfully synthesized using both solvothermal and microwave-assisted methods. The CTF-CN polymer absorbed strongly across the visible region and after decoration with Pt nanoparticles demonstrated very good activity for photocatalytic hydrogen production in a H_2O -TEOA- CH_3OH mixture under UV-vis excitation. A hydrogen production rate of $\sim 487.6\ \mu\text{mol g}^{-1}\text{ h}^{-1}$ was realized at a Pt loading of 5 wt.%, comparable to that of a Pt/ $\text{g-C}_3\text{N}_4$ photocatalyst under the same testing conditions ($1088.8\ \mu\text{mol g}^{-1}\text{ h}^{-1}$). The CTF-CN demonstrated excellent thermal and photocatalytic stability, with no deactivation observed even after 16 h testing. In addition, the presence of the rich cyano groups on the skeleton of CTF-CN provides an abundance of active sites for further chemical modifications, thus potentially allowing the synthesis of families of CTFs using CTF-CN as an intermediate for further applications such as electrocatalyst development for fuel cells and batteries [42, 43].

Data Availability

The original data used to support the findings of this study are available from the corresponding author upon request.

Conflicts of Interest

The authors declare that they have no conflicts of interest.

Acknowledgments

This work was supported by the National Key R&D Plan (No. 2016YFB0302400) and Agricultural Key Applied Technology Innovation Project of Shandong Province (2017, No. 6). GINW acknowledges funding support from the Shandong Provincial “Double-Hundred Talent Plan” on 100 Foreign Experts, the Energy Education Trust of New Zealand, and the MacDiarmid Institute for Advanced Materials and Nanotechnology.

Supplementary Materials

Figure S1: ^1H NMR spectra for (a) TAPT and (b) CTF-CN. The samples were dissolved in deuterated DMSO for the analyses. Figure S2: N_2 adsorption and desorption isotherms for CTF-CN collected at 77 K. Table S1: summarized XPS chemical composition data for CTF-CN, its precursors, and $\text{g-C}_3\text{N}_4$ reference photocatalyst. Data for Pt/CTF-CN and Pt/ $\text{g-C}_3\text{N}_4$ is also included. Table S2: N 1s peak position for different N environments. Table S3: C 1s peak position for different C environments. Figure S3: TGA data for CTF-CN and the starting materials used in the synthesis of CTF-CN. All data was collected at a heating rate of $10^\circ\text{C min}^{-1}$ under a N_2 atmosphere. Table S4: summarized H_2 production data for Pt/CTF-CN and Pt/ $\text{g-C}_3\text{N}_4$ photocatalysts. Table S5: performance comparison of different covalent triazine framework- (CTF-) based photocatalysts for H_2 production under visible ($\lambda > 420\text{ nm}$) or UV-visible irradiation. Figure S4: (a) H_2 production data for CTF-CN with different cocatalyst Pt contents, (b) H_2 production data for CTF-CN with different sacrifices, and (c) H_2 production data for CTF-CN and CTF (without cyano groups). Figure S5: FT-IR absorbance spectra for CTF-CN and $\text{g-C}_3\text{N}_4$ before and after the H_2 production tests. During the H_2 production tests, aqueous Pt(II) was photoreduced to Pt^0 on the surface of the photocatalyst. Table S6: summarized H_2 production data for various Pt/ $\text{g-C}_3\text{N}_4$ photocatalysts. Figure S6: TEM images of CTF-CN synthesized using the microwave method. (*Supplementary Materials*)

References

- [1] X. Wang, K. Maeda, A. Thomas et al., “A metal-free polymeric photocatalyst for hydrogen production from water under visible light,” *Nature Materials*, vol. 8, no. 1, pp. 76–80, 2009.
- [2] G. Liao, Y. Gong, L. Zhang, H. Gao, G. J. Yang, and B. Fang, “Semiconductor polymeric graphitic carbon nitride photocatalysts: the “holy grail” for the photocatalytic hydrogen evolution reaction under visible light,” *Energy & Environmental Science*, vol. 12, no. 7, pp. 2080–2147, 2019.

- [3] S. Cao and J. Yu, "g-C₃N₄-based photocatalysts for hydrogen generation," *The Journal of Physical Chemistry Letters*, vol. 5, no. 12, pp. 2101–2107, 2014.
- [4] J. Liu, Y. Zhang, L. Lu, G. Wu, and W. Chen, "Self-regenerated solar-driven photocatalytic water-splitting by urea derived graphitic carbon nitride with platinum nanoparticles," *Chemical Communications*, vol. 48, no. 70, pp. 8826–8828, 2012.
- [5] P. Niu, M. Qiao, Y. Li, L. Huang, and T. Zhai, "Distinctive defects engineering in graphitic carbon nitride for greatly extended visible light photocatalytic hydrogen evolution," *Nano Energy*, vol. 44, pp. 73–81, 2018.
- [6] C.-Q. Xu, K. Li, and W.-D. Zhang, "Enhancing visible light photocatalytic activity of nitrogen-deficient g-C₃N₄ via thermal polymerization of acetic acid-treated melamine," *Journal of Colloid and Interface Science*, vol. 495, pp. 27–36, 2017.
- [7] J. Liu, Y. Liu, N. Liu et al., "Water splitting. Metal-free efficient photocatalyst for stable visible water splitting via a two-electron pathway," *Science*, vol. 347, no. 6225, pp. 970–974, 2015.
- [8] Y. Yu, W. Yan, X. Wang et al., "Surface engineering for extremely enhanced charge separation and photocatalytic hydrogen evolution on g-C₃N₄," *Advanced Materials*, vol. 30, no. 9, article 1705060, 2018.
- [9] Y.-J. Yuan, Z. Shen, S. Wu et al., "Liquid exfoliation of g-C₃N₄ nanosheets to construct 2D-2D MoS₂/g-C₃N₄ photocatalyst for enhanced photocatalytic H₂ production activity," *Applied Catalysis B: Environmental*, vol. 246, pp. 120–128, 2019.
- [10] S. Anandan, J.-J. Wu, D. Bahnemann, A. Emeline, and M. Ashokkumar, "Crumpled Cu₂O-g-C₃N₄ nanosheets for hydrogen evolution catalysis," *Colloids and Surfaces A: Physicochemical and Engineering Aspects*, vol. 527, pp. 34–41, 2017.
- [11] W.-J. Ong, L.-L. Tan, Y.-H. Ng, S.-T. Yong, and S.-P. Chai, "Graphitic carbon nitride (g-C₃N₄)-based photocatalysts for artificial photosynthesis and environmental remediation: are we a step closer to achieving sustainability?," *Chemical Reviews*, vol. 116, no. 12, pp. 7159–7329, 2016.
- [12] Z. Jiang, X. Zhang, H.-S. Chen, X. Hu, and P. Yang, "Formation of g-C₃N₄ Nanotubes towards superior photocatalysis performance," *ChemCatChem*, vol. 11, no. 18, pp. 4558–4567, 2019.
- [13] P. Kuhn, M. Antonietti, and A. Thomas, "Ionothermal synthesis von porösen kovalenten Triazin-Polymernetzwerken," *Angewandte Chemie*, vol. 120, no. 18, pp. 3499–3502, 2008.
- [14] A.-P. Cote, A.-I. Benin, N.-W. Ockwig, M.-O. Keeffe, A.-J. Matzger, and O.-M. Yaghi, "Porous, crystalline, covalent organic frameworks," *Science*, vol. 310, no. 5751, pp. 1166–1170, 2005.
- [15] D. Chen, S. Huang, L. Zhong et al., "In situ preparation of thin and rigid COF film on Li anode as artificial solid electrolyte interphase layer resisting Li dendrite puncture," *Advanced Functional Materials*, vol. 30, no. 7, article 1907717, 2020.
- [16] G. Wang, N. Tahir, I. Onyshchenko et al., "Novel hexaazatrinaphthalene-based covalent triazine frameworks as high-performance platforms for efficient carbon capture and storage," *Microporous and Mesoporous Materials*, vol. 290, article 109650, 2019.
- [17] Z. Yang, S. Wang, Z. Zhang et al., "Influence of fluorination on CO₂ adsorption in materials derived from fluorinated covalent triazine framework precursors," *Journal of Materials Chemistry A*, vol. 7, no. 29, pp. 17277–17282, 2019.
- [18] P. van der Voort, H.-S. Jena, C. Krishnaraj, J. Schmidt, K. Leus, and K. Van Hecke, "Triggering white-light emission in a 2D imine covalent organic framework through lanthanide augmentation," *ACS Applied Materials & Interfaces*, vol. 11, no. 30, pp. 27343–27352, 2019.
- [19] K. Kamiya, R. Kamai, K. Hashimoto, and S. Nakanishi, "Platinum-modified covalent triazine frameworks hybridized with carbon nanoparticles as methanol-tolerant oxygen reduction electrocatalysts," *Nature Communications*, vol. 5, no. 1, pp. 1–6, 2014.
- [20] S.-y. Ding, J. Gao, Q. Wang et al., "Construction of covalent organic framework for catalysis: Pd/COF-LZU1 in Suzuki-Miyaura coupling reaction," *Journal of the American Chemical Society*, vol. 133, no. 49, pp. 19816–19822, 2011.
- [21] G. Zhang, Z.-a. Lan, and X. Wang, "Conjugated polymers: catalysts for photocatalytic hydrogen evolution," *Angewandte Chemie International Edition*, vol. 55, no. 51, pp. 15712–15727, 2016.
- [22] J. Xie, S.-A. Shevlin, Q. Ruan et al., "Efficient visible light-driven water oxidation and proton reduction by an ordered covalent triazine-based framework," *Energy & Environmental Science*, vol. 11, no. 6, pp. 1617–1624, 2018.
- [23] T. Banerjee, K. Gottschling, G. Savasci, C. Ochsenfeld, and B.-V. Lotsch, "H₂ evolution with covalent organic framework photocatalysts," *ACS Energy Letters*, vol. 3, no. 2, pp. 400–409, 2018.
- [24] C. B. Meier, R. S. Sprick, A. Monti et al., "Structure-property relationships for covalent triazine-based frameworks: the effect of spacer length on photocatalytic hydrogen evolution from water," *Polymer*, vol. 126, pp. 283–290, 2017.
- [25] J. Bi, W. Fang, L. Li et al., "Covalent triazine-based frameworks as visible light photocatalysts for the splitting of water," *Macromolecular Rapid Communications*, vol. 36, no. 20, pp. 1799–1805, 2015.
- [26] J. H. Ko, N. Kang, N. Park et al., "Hollow microporous organic networks bearing triphenylamines and anthraquinones: diffusion pathway effect in visible light-driven oxidative coupling of benzylamines," *ACS Macro Letters*, vol. 4, no. 7, pp. 669–672, 2015.
- [27] L. Li, W. Fang, P. Zhang, Y. He, J. Wang, and W. Su, "Sulfur-doped covalent triazine-based frameworks for enhanced photocatalytic hydrogen evolution from water under visible light," *Journal of Materials Chemistry A*, vol. 4, no. 32, pp. 12402–12406, 2016.
- [28] L. Wang, Y. Hong, E. Liu, X. Duan, X. Lin, and J. Shi, "A bottom-up acidification strategy engineered ultrathin g-C₃N₄ nanosheets towards boosting photocatalytic hydrogen evolution," *Carbon*, vol. 163, pp. 234–243, 2020.
- [29] M. Sun, H. X. Guan, W. D. Zhang, and Y. X. Yu, "Strong organic acid-assisted synthesis of holey graphitic carbon nitride for efficient visible light photocatalytic H₂ generation," *International Journal of Hydrogen Energy*, vol. 44, no. 41, pp. 23091–23100, 2019.
- [30] J. Wen, J. Xie, X. Chen, and X. Li, "A review on g-C₃N₄-based photocatalysts," *Applied Surface Science*, vol. 391, pp. 72–123, 2017.
- [31] Y. Hu, Y. Qin, X. Gao et al., "One-pot synthesis of core-expanded naphthalene diimides: enabling N-substituent modulation for diverse n-type organic materials," *Organic Letters*, vol. 14, no. 1, pp. 292–295, 2012.
- [32] Y. Hu, X. Gao, C.-A. Di et al., "Core-expanded naphthalene diimides fused with sulfur heterocycles and end-capped with electron-withdrawing groups for air-stable solution-

- processed n-channel organic thin film transistors,” *Chemistry of Materials*, vol. 23, no. 5, pp. 1204–1215, 2011.
- [33] X. Gao, C.-a. Di, Y. Hu et al., “Core-expanded naphthalene diimides fused with 2-(1, 3-dithiol-2-ylidene) malonitrile groups for high-performance, ambient-stable, solution-processed n-channel organic thin film transistors,” *Journal of the American Chemical Society*, vol. 132, no. 11, pp. 3697–3699, 2010.
- [34] F. Jing, R. Liang, J. Xiong et al., “MIL-68(Fe) as an efficient visible-light-driven photocatalyst for the treatment of a simulated waste-water contain Cr(VI) and malachite green,” *Applied Catalysis B: Environmental*, vol. 205, no. 5, pp. 9–15, 2017.
- [35] Z. Cheng, W. Fang, T. Zhao et al., “Efficient visible-light-driven photocatalytic hydrogen evolution on phosphorus-doped covalent triazine-based frameworks,” *ACS Applied Materials Interfaces*, vol. 10, no. 48, pp. 41415–41421, 2018.
- [36] K. Wang, L.-m. Yang, X. Wang et al., “Covalent triazine frameworks via a low-temperature polycondensation approach,” *Angewandte Chemie International Edition*, vol. 56, no. 45, pp. 14149–14153, 2017.
- [37] D. Y. Osadchii, A. I. Olivos-Suarez, A. V. Bavykina, and J. Gascon, “Revisiting nitrogen species in covalent triazine frameworks,” *Langmuir*, vol. 33, no. 50, pp. 14278–14285, 2017.
- [38] J.-F. Moulder, W.-F. Stickle, P.-E. Sobol, and K.-D. Bomben, *Handbook of X-ray Photoelectron Spectroscopy*, J. Chastain, Ed., Perkin-Elmer Corporation, 1992.
- [39] J. Zhang, J. Chen, Y. Wan et al., “Defect engineering in atomic-layered graphitic carbon nitride for greatly extended visible-light photocatalytic hydrogen evolution,” *ACS Applied Materials & Interfaces*, vol. 12, no. 12, pp. 13805–13812, 2020.
- [40] M. Liu, L. Guo, S. Jin, and B. Tan, “Covalent triazine frameworks: synthesis and applications,” *Journal of Materials Chemistry A*, vol. 7, no. 10, pp. 5153–5172, 2019.
- [41] Y. Zhang and S. Jin, “Recent advancements in the synthesis of covalent triazine frameworks for energy and environmental applications,” *Polymers*, vol. 11, no. 1, p. 31, 2019.
- [42] T. Feng, J.-M. Wang, S.-T. Gao et al., “Covalent triazine frameworks supported CoPd nanoparticles for boosting hydrogen generation from formic acid,” *Applied Surface Science*, vol. 469, pp. 431–436, 2019.
- [43] R. Kamai, K. Kamiya, K. Hashimoto, and S. Nakanishi, “Oxygen-tolerant electrodes with platinum-loaded covalent triazine frameworks for the hydrogen oxidation reaction,” *Angewandte Chemie International Edition*, vol. 55, no. 42, pp. 13184–13188, 2016.